PAUL SCHERRER INSTITUT

PSI

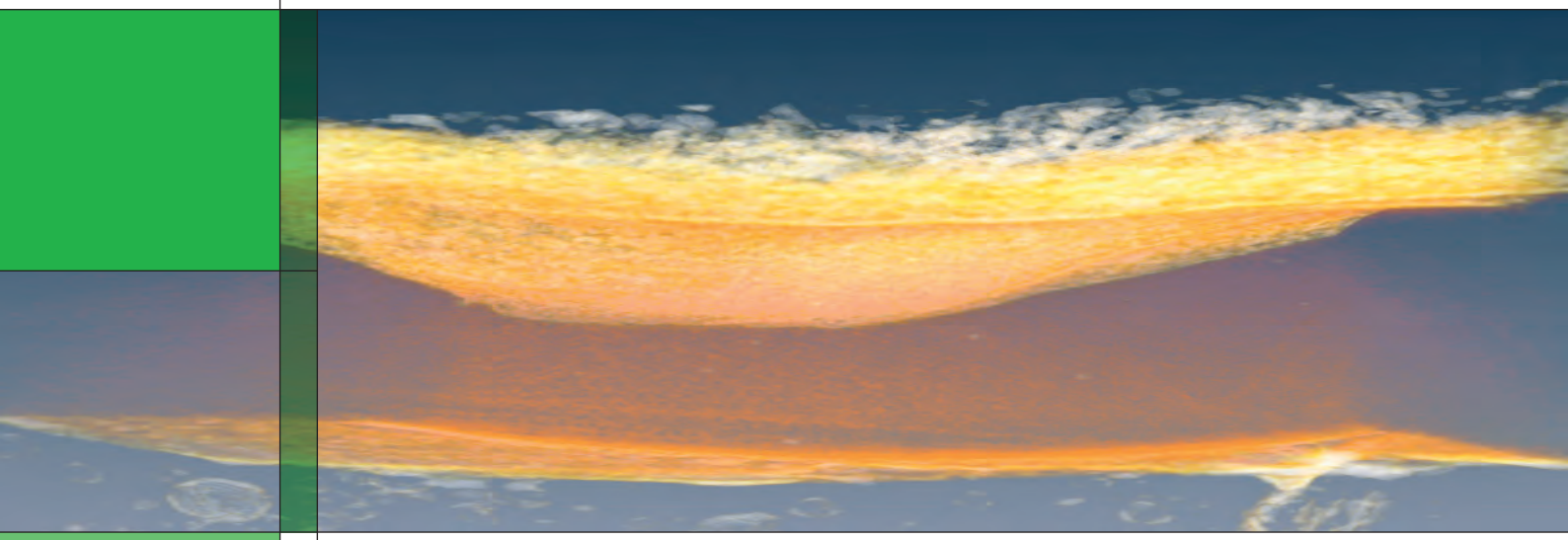

Annual Report 2008

Electrochemistry Laboratory

http://ecl.web.psi.ch

COVER PHOTO:

3-D image of a membrane electrode assembly (MEA) recorded by X-ray tomography at the TOMCAT-Beamline of the SLS. Pt on the cathode is reflected by the golden layer on top. The anode at the bottom has no Pt.

PAUL SCHERRER INSTITUT

PSI

Electrochemistry Laboratory

Annual Report 2008

Hardcopies of this report are available from:
Isabella Kalt (isabella.kalt@psi.ch)
Paul Scherrer Institut
5232 Villigen PSI
Switzerland

A full version of this report is also available on the web:
http://ecl.web.psi.ch

Paul Scherrer Institut
Electrochemistry Laboratory
5232 Villigen PSI
Switzerland

Secretary
Phone +41 (0)56 310 29 19
Fax +41 (0)56 310 44 15

Publisher
Electrochemistry Laboratory
Paul Scherrer Institut
5232 Villigen PSI

Editorial Team
Isabella Kalt
Rüdiger Kötz
Günther G. Scherer

Printing
Paul Scherrer Institut

ISSN 1661-5379
PSI Electrochemistry Laboratory – Annual Report 2008

CONTENTS

EDITORIAL

On May 30th the contract was signed between Paul Scherrer Institut and Belenos Clean Power Holding, Biel, to develop a “Swiss Fuel Cell” for automotive applications. Based on the recent successful collaborations together with other industrial partners in the HY.POWER and HY-LIGHT projects, the concept of an all electric power train with a hybrid configuration of a H_2/O_2-fuel cell and an electrochemical storage unit (battery or supercapacitor) will be further developed. This will be part of a larger program demonstrating a sustainable energy system in a region of Switzerland. With this program we come closer to bringing electrochemical conversion and storage devices “Made in Switzerland” to the market place.

All this is made possible due to our long standing comprehensive approach, namely to carry out research and development of electrochemical energy conversion and storage systems at the materials, cell, and systems level for fuel cells, batteries, and supercapacitors. Our achievements are well recognized by our industrial as well as by our academic partners. It also provides a challenging interdisciplinary environment to our PhD-students, co-workers, and guests, opening job opportunities for them in various fields.

Again, within this present Annual Report 2008, all our four research groups, namely Fuel Cells, Fuel Cell Systems, Batteries, and Interfaces and Capacitors communicate the progress made during the past year in numerous contributions. As in recent years, topics range from materials development for the different electrochemical systems to the development of novel characterization methods adapted to the respective electrochemical system, i.e. fuel cell, battery, or capacitor. Success of our continuous efforts is well documented in our list of peer reviewed publications, patent applications, invited contributions to conferences, and talks and poster presentations at various conferences and workshops worldwide

Our 24th One-Day-Symposium took place on May 7, 2008, addressing the subject of “Electrochemical Materials Processing”, with excellent contributions by F. Di Quarto (Univ. Palermo), M.M. Lohrengel (Univ. Düsseldorf), R. Schuster (Univ. Karlsruhe), W. Kautek (Univ. Wien), J.-C. Puippe (Innosurf, Châtel St. Denis, CH), and A.W. Hassel (MPI Düsseldorf).

On May 7, 2009, we will celebrate the 25th One-Day-Symposium entitled “Electrochemistry: Learning from the past to master the future”. Together with D.M. Kolb (Univ. Ulm), N.M. Markovic (Argonne National Laboratory), J. Maier (MPI Stuttgart), J.M. Tarascon (CNRS Amiens), A. Züttel (EMPA Dübendorf), and M. Waidhas (Siemens Research & Development, Erlangen), we review recent key developments in various fields of Electrochemistry and dare to take a look into the future of electrochemical energy research, both, from an academic and industrial point of view.

This Annual Report 2008 gives proof that we successfully continued our effort to contribute to the field of Electrochemistry and in particular to Electrochemical Energy R&D. Successful transfer of our know-how to industrial partners as well as the education of students and young scientists will continue to be prime targets for the year 2009. As in past years, our work is carried out in the context of R&D for a sustainable energy development, within Paul Scherrer Institut and the Domain of the Swiss Federal Institutes of Technology.

Günther G. Scherer

SCIENTIFIC CONTRIBUTIONS 2008

FUEL CELLS

MATERIALS

Reaction of •OH with some model compounds for PEFC membranes based on poly(styrene sulfonic acid)

S.M. Dockheer, A. Domazou[1], L. Gubler, G.G. Scherer, W.H. Koppenol[1]. A. Wokaun

phone: +41 56 310 4003, e-mail: sindy.dockheer@psi.ch

Reactions of •OH with sulfonated aromatics are of interest because of their presumed involvement in the degradation mechanism of fuel cell membranes. In view of the recent development of membranes based on α-methyl-styrene [1], without an abstractable H atom in α-position to the aromatic ring, also subsequent reactions after the •OH addition to the ring are of interest.

Experimental

Aqueous sample solutions at neutral pH and room temperature were irradiated with doses of 1 - 20 Gy / pulse, delivered from a 2 MeV 705 Febetron electron accelerator, equipped with an optical detection system. •OH were generated according to

$$N_2O + e^-_{aq} + H_2O \rightarrow N_2 + {}^{\bullet}OH + {}^{-}OH \quad k = 9.8\cdot10^9\ M^{-1}s^{-1}$$

and aqueous sample solutions were saturated with N_2O or the appropriate partial pressure ratio of N_2O/O_2.

Results

The •OH reacts with sulfonated aromatics with rate constants near the diffusion controlled limit, as shown in table 1. We note that in case of the oligomer and tosylate *k* is the rate constant for the sum of abstraction and addition reactions. The specific rate for the addition reaction can be derived by mass balance from the hydroxycyclohexadienyl radical yield, and results in a constant value of $9.8\cdot10^9\ M^{-1}s^{-1}$ for the •OH addition to the oligomer.

***Table 1**. Absolute rate constants for the reaction of •OH with some substrates and second order rate constants for the decay of the OH-adduct in N_2O_{sat} solutions.*

Substrate	*k* [$M^{-1}s^{-1}$] •OH + substrate	Decay of OH-adduct $2k/\varepsilon$ [cm/s]
PSSS MW1360	$(1.3 \pm 0.3)\cdot10^{10}$	$(6.4 \pm 0.4)\cdot10^5$
tosylate	$(1.0\pm0.1)\cdot10^{10}$	$(5.4\pm1.3)\cdot10^5$
benzenesulfonate	$(6.5 \pm1.9)\cdot10^9$	$(2.5 \pm 0.4)\cdot10^5$

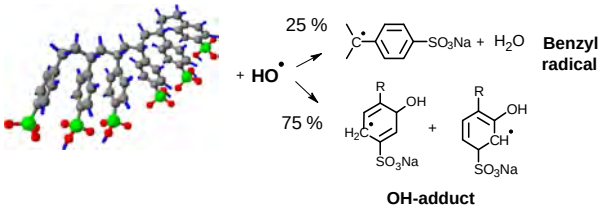

***Figure 1.** Oligomer of poly(sodium styrene sulfonate), PSSS, with average molecular weight 1360, reacts with 75 % of initially produced •OH to an OH-adduct.*

The reaction of the OH-adduct with O_2 was studied with benzenesulfonate. C-centered radicals generally react with O_2 with rate constants in the order of $10^9\ M^{-1}s^{-1}$. Pentadienyl type radicals are an exception, as their reaction with O_2 is slower and especially the presence of electron-withdrawing substituents retards the reaction. In some cases, due to the low binding energy of the C-O bond in the corresponding peroxyl radical, being around a value of 25 kJ/mol [2], the hydroxycyclohexadienyl radical reacts reversibly with oxygen.

Irradiated oxygenated benzenesulfonate solutions, with 80 - 400 µM O_2, resulted in a fast initial decay of the OH-adduct. We did not find any indication of reversibility and determined a rate constant of $7\cdot10^6$ - $2\cdot10^7\ M^{-1}s^{-1}$ for the reaction with O_2, similar to the published rate constant for benzoic acid [2].

The formed peroxyl radicals release $HO_2^{\bullet}$ (pK_a = 4.8), which was detected with tetranitromethane, TNM, at pH 7, according to:

$$O_2^{\bullet-} + C(NO_2)_4 \rightarrow O_2 + C(NO_2)^{3-}_3 + NO_2^{\bullet}$$

$k = 1.9\cdot10^9\ M^{-1}s^{-1}$, with $\varepsilon_{350}[C(NO_2)^{3-}_3] = 15'000\ M^{-1}cm^{-1}$,

to yield the hydroxylated product. As displayed in Fig. 2, the radiation chemical yield of $HO_2^{\bullet}$ increases with lower dose as second order reactions slow down.

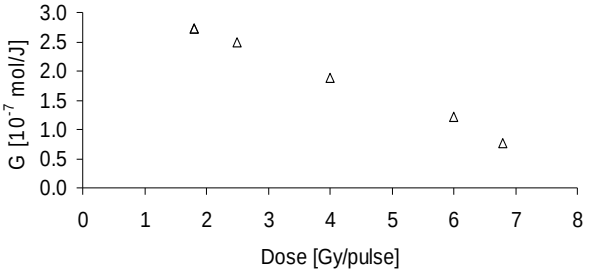

***Figure 2**. Radiation chemical yield of $O_2^{\bullet-}$ as a function of dose, from an irradiated 260 µM O_2, 410 µM benzenesulfonate, 100 µM tetranitromethane containing solution.*

Conclusions

In the absence of benzylic H atoms, the •OH reacts in an addition reaction with the aromatic substrate. At low doses, a condition that might be more relevant for a fuel cell, the $HO_2^{\bullet}$ yield, released form the corresponding peroxyl radicals, increases. In case of benzenesulfonate, at a dose of 1.8 Gy, the $HO_2^{\bullet}$ is formed with 47 % yield. The $HO_2^{\bullet}$ might then undergo further H-abstraction reactions from the aliphatic C-backbone of the membrane, resulting in formation of C-centered radicals.

References

[1] L. Gubler, M. Slaski, A. Wokaun G. G. Scherer, Electrochem. Commun. **8**, 1215-1219 (2006).

[2] S. Naumov, C. von Sonntag, J. Phys. Org. Chem. **18**, 586-594 (2005).

[3] X.F. Fang, X. Pan, A. Rahmann, H. P. Schuchmann, C. von Sonntag, Chem. Eur. J. **7**, 423 (1995).

[1] ETH Zürich

An enhanced radiation grafting model comprising monomer transport

L. Gubler, F. Wallasch, A. Wokaun, G.G. Scherer

phone: +41 56 310 2673, e-mail: lorenz.gubler@psi.ch

Fuel cells are electrochemical energy conversion reactors, producing electrical power by virtue of spatially separated oxidation and reduction half-cell reactions, respectively, with exchange of ionic charges via the electrolyte. In the polymer electrolyte fuel cell (PEFC) a cation exchange membrane is used as solid electrolyte to transport protons from anode to cathode [1].

We have identified radiation grafting as a promising method for fuel cell membrane preparation. Radiation grafting is a versatile and potentially cost-effective technology. The process involves the pre-irradiation of a thin (25 µm) base polymer film, e.g., FEP or ETFE, with electrons to introduce radicals, followed by graft polymerization of styrene or other monomers to form a graft copolymer (Figure 1). Sulfonation of the grafted film introduces sulfonic acid groups, converting the film into a proton conducting polymer.

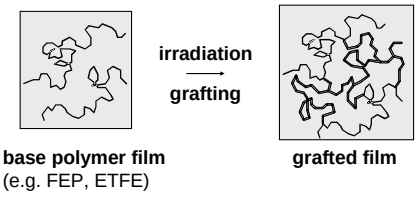

Figure 1. *Preparation of a graft copolymer via activation by pre-irradiation, followed by growing of grafted chains onto the base polymer through copolymerization. Proton conductivity is introduced in a last stage via sulfonation.*

Grafting Model

The amount of introduced graft component is expressed by the degree of grafting (or graft level) X_G according to

$$X_G = \frac{\Delta m}{m_0} = \frac{m_g - m_0}{m_0} \quad (1)$$

where m_0 and m_g are the mass of the film before and after grafting, respectively. The understanding of the grafting process is pivotal to the understanding of the resulting membrane structure and properties. The grafting reaction has been described previously using a homogeneous model, taking into account the chain growth reaction by polymerization and loss of radicals by termination [2]. The rate of polymerization r_p and termination r_t, respectively, are as follows:

$$r_p = \frac{1}{\alpha}\frac{dX_G}{dt} = k_p[P\bullet][M] \approx k_p[P\bullet][M]_0 \quad (2)$$

$$r_t = \frac{d[P\bullet]}{dt} = -k_t[P\bullet]^2 \quad (3)$$

where $\alpha = M/\rho$, with M as the molecular weight of the monomer and ρ the density of the film, k_p and k_t are the respective rate constants, [P•] is the radical concentration in the film, and [M] is the monomer concentration near the reactive sites, which is assumed to remain at a constant value of $[M]_0$ due to low conversion. The initial radical concentration, following irradiation, is $[P\bullet]_0$. The degree of grafting X_G is obtained by integration and combination of (2) and (3):

$$\frac{1}{\alpha}X_G = \frac{k_p[M]_0}{k_t}\ln(1 + k_t[P\bullet]_0 t) = \frac{r_{p0}}{\gamma}\ln(1+\gamma t) \quad (4)$$

with following replacements: r_{p0} (apparent initial polymerization rate) = $k_p[M]_0[P\bullet]_0$ and γ (radical recombination rate, termination rate) = $k_t[P\bullet]_0$. Experimental grafting data can be fitted reasonably well to the kinetic model (4), except at low temperatures and when base films thicker than 25 µm are used [3]. Under those conditions, a pronounced 'induction' period is observed, i.e., the highest grafting rate is observed not at the beginning (t=0), as would be expected from (4), but after a certain delay time t_0, which increases with increasing film thickness and decreasing temperature. This delay has been interpreted as the time required for the monomers to penetrate from the surface into the bulk of the film [2]. In the simplest approach, it can be accounted for by replacing t with (t-t_0) in (4). However, the graft level during the induction period $0 \le t \le t_0$ cannot be described in this case.

At this point, it is clear that the description of the grafting reaction by a homogeneous model is unsatisfactory. Essentially, the grafting proceeds from the surface to the interior of the film via a so-called 'grafting front mechanism' [4]. As a consequence, graft penetration throughout the film is only achieved at a sufficiently high graft level.

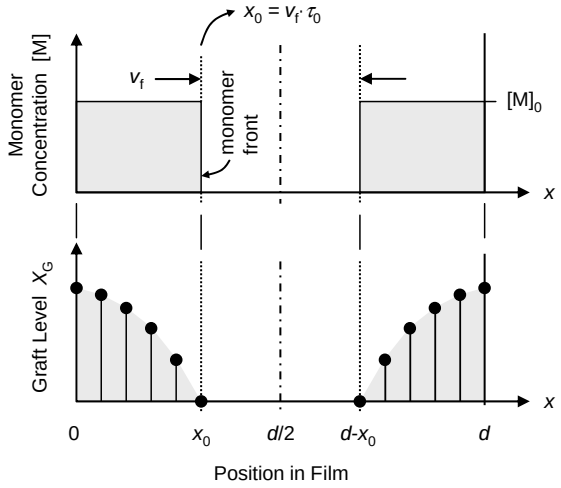

Figure 2. *The enhanced grafting model assumes propagation of the monomer into the film with constant velocity v_f. Grafting within the film starts when the monomer front reaches the respective depth. The film thickness is d.*

The enhanced grafting model presented here is a 1D model, which takes into account the transport of the monomer into the film with a constant front velocity v_f (Figure 2). The monomer concentration behind the front is assumed to be constant at $[M]_0$. While grafting starts immediately at the film surface, the reaction at a depth x_0 is delayed by the time interval $\tau_0 = x_0/v_f$ required for the monomer front to reach that depth. The local graft level X_G can therefore be expressed according to

$$\frac{1}{\alpha} X_G(t,x) = \begin{cases} t \le \tau: & 0 \\ t > \tau: & \frac{r_{p0}}{\gamma} \ln(1+\gamma(t-\tau)) \end{cases} \quad , \quad \tau = \frac{x}{v_f} \qquad (5)$$

The time T after which the fronts from both sides meet at the film center at $x = d/2$ is $T = d/(2v_f)$, where d is the film thickness. The average graft level $\overline{X_G}$ is then easily obtained by integration:

$$\overline{X_G}(t) = \frac{2}{d} \cdot \int_0^{d/2} X_G(t,x)\,dx \qquad (6)$$

Experimental

The applicability of the model to experimental data was evaluated using a series of grafting experiments carried out in a temperature range between 35 and 80 °C, which have been reported in our 2007 Annual Report [6]. For the numerical fitting procedure of the model to the experimental graft levels, the integral in (6) was replaced by a sum over 30 discrete 'film slices'.

Results

The experimental grafting data as a function of temperature and the fitted enhanced kinetic model are displayed in Figure 3. It is obvious that the grafting reaction at low temperature is substantially retarded, indicated by the extended initial convex part of the curve. At temperatures above 50°C, however, the grafting rate, i.e. the slope of the curve, decreases notably after long reaction periods, although initially the grafting proceeds very rapidly.

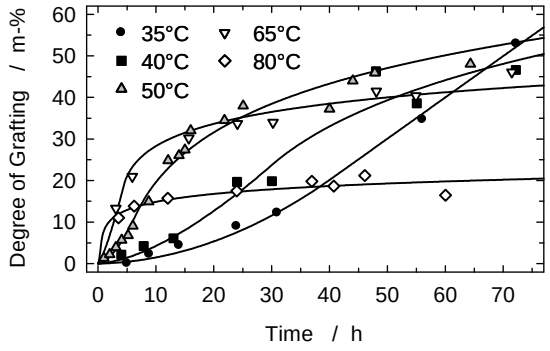

Figure 3. *Grating curves at different temperatures from [6] and fitted model (6).*

The grafting characteristics as a function of temperature can be interpreted more easily by plotting the fitting parameters as a function of (inverse) temperature (Figure 4). From the Arrhenius plot, the activation energies for the propagation rate r_{p0} and termination rate γ can be calculated. The termination rate seems to increase more strongly with temperature, which explains the decreasing degree of grafting at the higher temperature [3]. The slow grafting front velocity v_f at low temperatures causes the extended induction time. The time T for graft penetration decreases from 33 h at 35 °C to 3 h at 80 °C. Obviously, grafting will be confined to the surface initially [4], while the monomer front propagates into the film and the film center remains ungrafted. Only after reaction times exceeding the penetration time T by a factor of around 2 will the grafting profile become uniform with a variation of less than 0.1 (10 % relative).

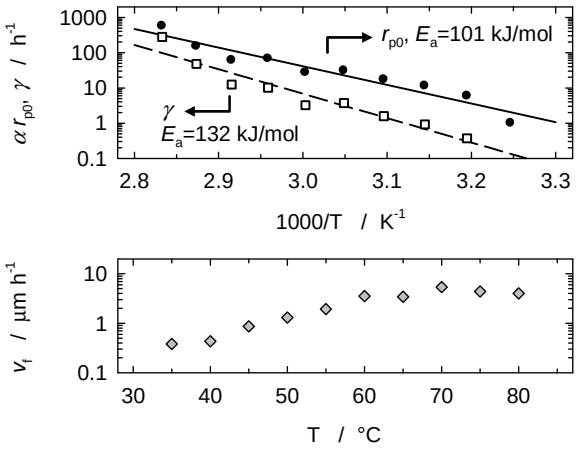

Figure 4. *Parameters $\alpha \cdot r_{p0}$ (r_{p0} = apparent initial polymerization rate), γ (radical recombination rate), and v_f (front velocity) determined by fitting to the experimental data in Figure 3.*

Discussion

The grafting curves displayed in Figure 3 are typical and highlight that practical graft levels of approximately 30 % are reached most efficiently at intermediate temperatures of 50 to 60 °C. It has to be emphasized, however, that differences in polymer structure and morphology are likely to exist in films of identical graft level but prepared at different temperature.

In contrast to the homogeneous model, the grafting curves with initial retardation can be represented well with the enhanced grafting model (Figure 3). Yet, the model is still comparatively crude. A sharp monomer propagation front is rather unlikely. In addition, other processes can be identified that might lead to a similar delay of the grafting reaction. For instance, the (hydro)peroxides created in the base polymer upon irradiation in air first need to decompose to yield radicals, which is a thermally activated process [7]. Furthermore, it is assumed that the radical concentration at a particular position x_0 is constant $[P\bullet]_0$ as long as the grafting front has not reached x_0. In reality, recombination occurs to some extent, despite the restricted chain mobility [8].

References

[1] L. Gubler, G.G. Scherer, Adv. Polym. Sci. **215**, 1-14 (2008).

[2] T. Rager, Helv. Chim. Acta **86**, 1966-1980 (2003).

[3] T. Rager, Helv. Chim. Acta **87**, 400-407 (2004).

[4] S. Alkan Gürsel, L. Gubler, B. Gupta, G.G. Scherer, Adv. Polym. Sci. **215**, 157-218 (2008).

[5] C. Schmidt, G. Schmidt-Naake, Macromol. Chem. Eng. **292**, 1067-1074 (2007).

[6] F. Wallasch, L. Gubler, G.G. Scherer, A. Wokaun, PSI Electrochemistry Annual Report 2007, 7, ISSN-1661-5379 (2008).

[7] M.M. Nasef, E.S.A. Hegazy, Prog. Polym. Sci. **29**, 499-561 (2004).

[8] S. Mitov, G. Hübner, H.-P. Brack, G. Scherer, E. Roduner, J. Polym. Sci. Part B: Polym. Phys. **44**, 3323-3336 (2006).

ETFE-graft-poly(AMSSA-co-MAN-co-DVB) membranes – *ex situ* properties

D. Henkensmeier, S. Lüscher, F. Wallasch, G.G. Scherer

phone: +41 56 310 2797, e-mail: dirk.henkensmeier@psi.ch

The stability of poly(styrenesulfonic acid) in the prevailing environment of a fuel cell can be increased by grafting it from a chemically stable and mechanically robust (per)fluorinated base film, e.g. FEP. Since the *α*-position of polystyrene is sensitive towards radical attack [1], an inherently more stable membrane can be obtained by substituting the labile *α*-proton by a methyl group. This lead to the development of FEP-*graft*-AMSSA-*co*-MAN-*co*-DVB membranes, AMSSA: α-methylstyrenesulfonic acid, MAN: methacrylonitrile [2]. A further improvement can be obtained by the utilization of ETFE base films, which are available in higher molecular weights (better mechanical properties), show faster grafting kinetics due to better interaction with the monomers, and demonstrate lower radiation induced damages during electron beam irradiation, as compared to their FEP-analogs [3].

Experimental

ETFE films (Dupont, 25 µm thick) were electron beam irradiated under air and stored at -80 °C before grafting at elevated temperature. The grafting mixture consisted of isopropanol, water and a monomer mixture (AMS, MAN and DVB). The graft level (GL) was determined as $GL = 100 \cdot (W_g - W_i) / W_i$, W_g = weight of the grafted film, W_i = weight of the pristine film. Sulfonation was achieved by reaction with 2 % chlorosulfonic acid in dichloromethane for 5 hours at rt, followed successively by hydrolysis in water at rt (over night) and 80 °C (for 8 hours). The water uptake was measured for membranes swollen in water at rt. For the determination of the area shrinkage, samples were punched out from water swollen membranes at room temperature and dried in vacuum at 80 °C for 2 hours. Ion conductivity was measured by ac impedance spectroscopy at rt.

Results

The dependence of the reaction kinetics on the irradiation dose is displayed in Fig. 1. To obtain grafted films of about 40 % GL [2], a reaction time of 4 hours and 19 hours is required for 3 kGy and 15 kGy irradiated films, respectively.

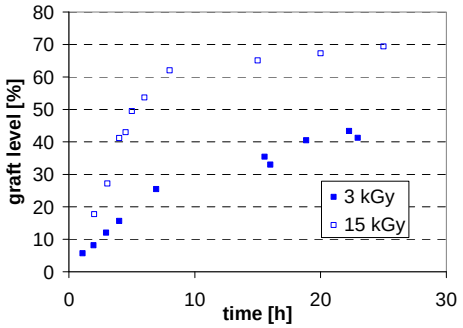

Figure 1. *Influence of the dose rate on the grafting kinetics.*

For membranes with a graft level of about 40 % and an irradiation dose of 15 kGy, the influence of the crosslinker content in the grafting solution on the *ex situ* properties was investigated. The mass based water uptake and the hydration number decrease significantly upon addition of DVB. Since the proton conductivity is closely related to the water content of the membrane, a high DVB content is not favourable.

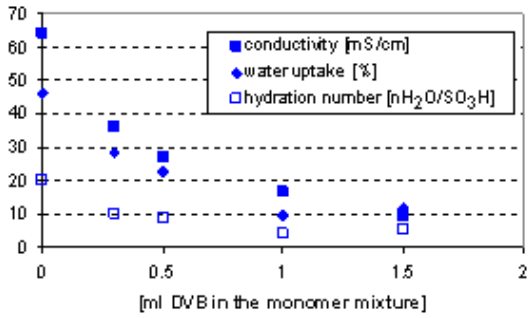

Figure 2. *Influence of the crosslinker on selected properties.*

On the other hand, the area swelling and shrinkage following hydration and dehydration is a major source for mechanical stress, leading to delamination of the MEA [4] and other mechanically induced defects. In summary, the DVB content of a membrane has to be optimised to obtain the required specifications with respect to performance (power output, lifetime), balancing the two opposing effects of crosslinking. At a GL of 40 %, all our membranes show lower or similar shrinkage than Nafion 112 (Figure 3).

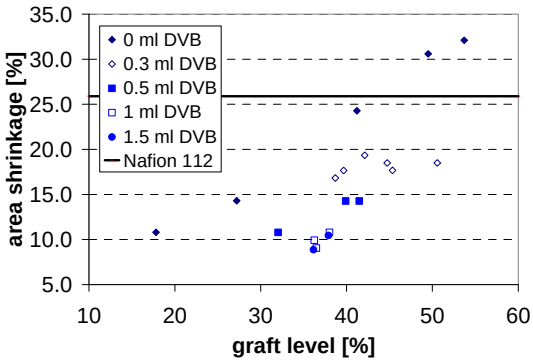

Figure 3. *Area shrinkage (wet → dry) of selected membranes.*

References

[1] G. Hübner, E. Roduner, J. Mater. Chem. **9**, 409 - 418 (1999).

[2] L. Gubler, M. Slaski, A. Wokaun, G. G. Scherer, Electrochem. Commun. **8**, 1215 - 1219 (2006); WO 2006084591.

[3] L. Gubler, H. Ben youcef, S. Alkan Gürsel, A. Wokaun, G. G. Scherer, Electrochem. Soc. Trans. **11**, 27 - 34 (2007).

[4] H.-S. Lee, A. Roy, O. Lane, S. Dunn, J. E. McGrath, Polymer **49**, 715 - 723 (2008).

Accelerated chemical aging and *post mortem* analysis of radiation grafted fuel cell membranes

M.M. Menamparambath, G.G. Scherer, A. Wokaun, L. Gubler

phone: +41 56 310 4003, e-mail: mini-mol.menamparambath@psi.ch

Durability, in the present context, is a concept that relates how fuel cell components and fuel cells are made and operated to how long they last. Typical membrane degradation in fuel cells results from mechanical, chemical, and electrochemical mechanisms occurring with time. With extensive *post mortem* characterization, degradation mechanisms can be identified, which will help to develop more durable fuel cell components and fuel cells. Open circuit voltage (OCV) hold experiments are an effective tool for understanding the chemical degradation of the membranes [1]

Experimental

Radiation grafted FEP based (25µm) PSI membranes are subjected to *in situ* accelerated chemical aging in single cells (OCV, 80 ^{0}C, 3 bar$_a$ for both fuel and oxidant (H_2/O_2), 100% relative humidity) for different time of operation. Electrodes used were from E-TEK with a Pt loading of 0.5 mg/cm^2. High frequency (1 kHz) resistance was measured online to detect the gradual increase in membrane resistance due to aging. Electrochemical hydrogen crossover measurements have been periodically carried out *in situ* to check the mechanical integrity of the membrane. Post test analyses of the aged membranes were carried out using a Perkin-Elmer FTIR spectrometer operating in 400 to 4000 cm $^{-1}$ region. The area of the peaks corresponding to the grafted component poly(styrene sulphonic acid) at 1010 cm $^{-1}$ and 1040 cm $^{-1}$ was quantified using GRAMS AI software. Degradation D of the grafted components is calculated via $D = 1- A_D/A_P$, where A_D is the peak area from the degraded membrane sample and A_P is the peak area from the pristine membrane sample.

Results and Discussion

Post test analysis of the membranes subjected to OCV over different time of operation is carried out by transmission FTIR and the extent of degradation is quantified (Figure 1). Membrane exposed to channel and land area of the flow field is differentiated using a slit mask [2].

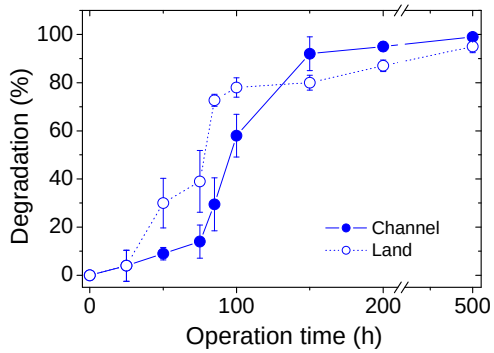

Figure 1. *Loss of grafted component of the membranes aged at open circuit voltage (OCV) over different time of operation.*

The membrane does seem to be stable up to 25 hours, yet shows notable degradation (channel 58% and land 78% for the peak 1040 cm^{-1}) at 100 hours. There is clearly an inhomogeneous degradation in channel and land area from 50 h to 150 h of operation. The decrease in intensity of these peaks is due to the chemical attack of active oxygen species on grafted poly(styrene sulphonic acid) followed by detaching from the FEP backbone. This caused a gradual increase in resistance of the membrane during fuel cell operation as indicated by high frequency resistance (1 kHz) measurements. Micro ATR-IR (attenuated total reflection IR), having a penetration depth of 1.6 µm, studies revealed that there is a strong difference in the extent of degradation in land areas of the anode and cathode side (Figure 2).

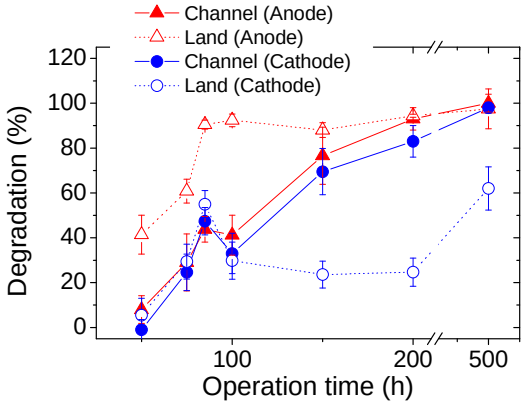

Figure 2. *Near-surface degradation analysis on anode and cathode side using Micro ATR-IR technique.*

Type of Operation	Operating Time	Degradation
OCV	500 h	99 %
High Current Density	500 h	12 %

Table 1. *Comparison of extent of degradation in OCV and high current density operations.*

The higher extent of degradation on the anode side could be due to the formation of active radicals by the diffused O_2 from the cathode side. Degradation under OCV operation (500 h) is compared with high current operation (500 h) (Table 1). These results indicate that the degradation of polymer electrolytes is highly influenced by the local operating parameters. Mechanical integrity monitored by H_2 permeation indicates that the membranes remain intact throughout the operation.

References

[1] V.O. Mittal, H.R. Kunz, J.M. Fenton, J. Electrochem. Soc. **154**, B652-B656 (2007).

[2] L. Gubler, R. Müller, G.G. Scherer PSI Electrochemistry Laboratory - Annual Report 2006, 20, ISSN 1661-5379 (2007).

Local gas analysis in PEFC during accelerated membrane degradation

G. Schuler, R. Müller, A. Wokaun, F.N. Büchi

phone: +41 56 310 53 96, e-mail: gabriel.schuler @psi.ch

Durability achievements of polymer electrolyte fuel cells (PEFC) generally do not fulfill the requirements of real world applications. Degradation under dynamic load conditions is still a challenge. Polymer electrolyte membranes are one of the susceptible components of present PEFC. Membrane degradation is measureable by loss of proton conductivity and loss of gas separation functionality. It is known that gas permeation lowers efficiency and membrane lifetime, but the mechanisms are still not fully understood. Existing accelerated test procedures allow membrane degradation investigations, but do not correlate the findings to real world operating conditions to predict cell lifetime. To set the base of this correlation we investigated accelerated chemical membrane degradation under various conditions. We measured local gas permeation characteristics of a cell of technical size during open circuit voltage tests (OCV-tests) under different humidity conditions.

Experimental

Various gas permeation measurement methods are described in literature [1]. Electrochemical and time-lag techniques are the most frequently used permeation investigation methods. Beside the easy implementation, these techniques show inherent lack of flexibility.

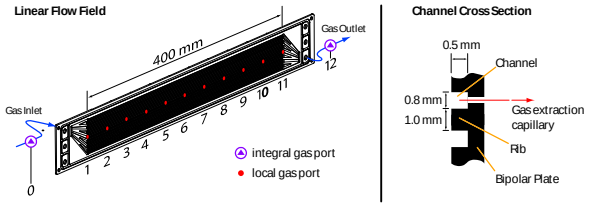

Figure 1. *Left: Linear flow field and gas port locations. Right: cross section of the bipolar plate with gas extraction.*

Online permeation investigations with these methods under real fuel cell conditions are not possible. Therefore we use gas analysis by mass spectrometry to investigate local membrane permeation behaviour under real operating conditions. The test rig consists of a fuel cell of technical size, local gas extraction lines and a mass spectrometer for gas analysis. The linear fuel cell has an active area of 200 cm^2 and a channel cross sectional area of 0.4 mm^2 (Fig.1). Nafion 112 with 12 µm Mylar (Dupont) subgaskets and catalyst coated Etek (Elat A6 V2.1) electrodes were used as membrane electrode assemblies (MEA). Eleven local gas extraction ports are located within the active area of the cell at each side of the membrane (Fig. 1). Gas is extracted from one representative channel in the middle of the linear flow field. Additional integral gas ports measure the gas compositions at cell in- and outlet. Locally extracted gas is conducted by fused silica capillaries to a rotor selector valve (RSV, Fig. 2) and guided to the quadrupole mass spectrometer (Pfeiffer Prisma 200M1). All extraction lines are fully heated to 120°C to ensure constant measurement conditions in the vacuum chamber of the mass spectrometer. During OCV-tests an undefined fraction of permeated oxygen or hydrogen will directly react on the catalyst of the permeation side and is therefore not representative for gas permeation measurements. Therefore we use helium as inert permeation tracer, which is added to the anode feed gas. Two humidification levels of 0.07 and 30% relative humidity at 80°C cell temperature were chosen. During the OCV-tests, anode and cathode operated in counter flow and the rates of reactant supply was adjusted to the load equivalent point of stoichiometry 2 and 0.2 A/cm^2. The cathode was fed with air while the anode feed gas consisted of 90% hydrogen and 10% helium. Anode and cathode pressure was set to 1.5 bar.

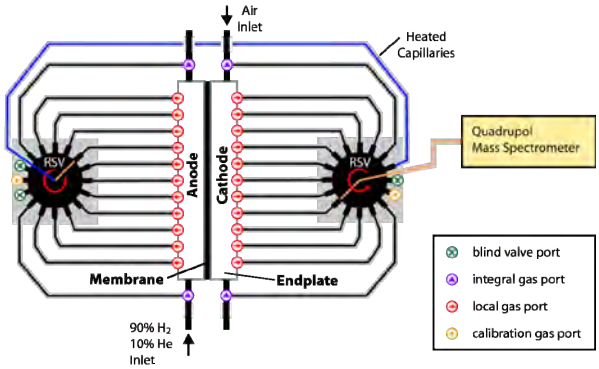

Figure 2. *Layout local gas analysis test rig. Anode gas extraction on the left, cathode gas extraction on the right side. Rotor selector valves (RSV) for capillary selection.*

Local permeation along the channel was measured at certain time intervals. Diffusive and combined diffusive and convective permeation was measured separately by applying an overpressure of 0.1 bar on the anode or cathode side, respectively (Fig. 3). Convective permeation rate was calculated under assumption of constant helium solubility in the membrane, while any influence of air back convection during the diffusive measurement was neglected. Polarization curves under standard conditions of 60°C cell temperature, relative humidity of 64% and stoichiometry of 2 with pure oxygen were conducted before and after the OCV-test.

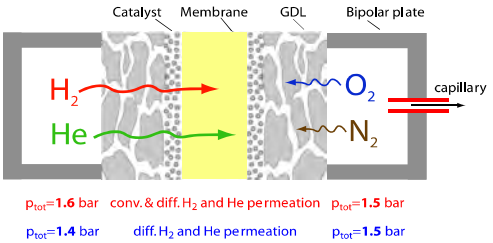

Figure 3. *Schematic diffusive and combined diffusive-convective helium permeation measurement.*

Results

Cell degradation due to different humidity is illustrated by polarization curves at begin and end of life (Fig. 4). Degradation under dry condition shows in comparison to humid condition only minor degradation. Integral helium concentration measurements at cathode outlet show the general permeation trend under different humidities (Fig. 5). Integral helium permeation increased in the 30% rH case by a factor of 19, while it remained

constant over more than 200 h under dry conditions of 0.07% rH.

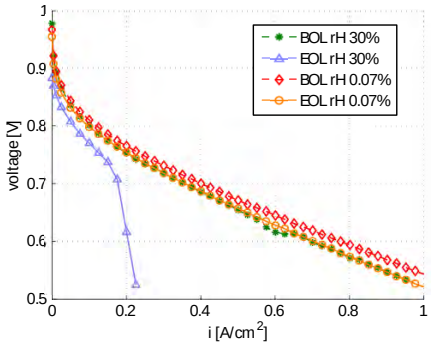

Figure 4. *Polarization curve at begin (BOL) and end of the OCV degradation test (EOL). Cell temperatur 70°C, rH 64%, hydrogen/oxygen stoichiometry 1.5/1.5; pressure 1.5/ 1.5 bar.*

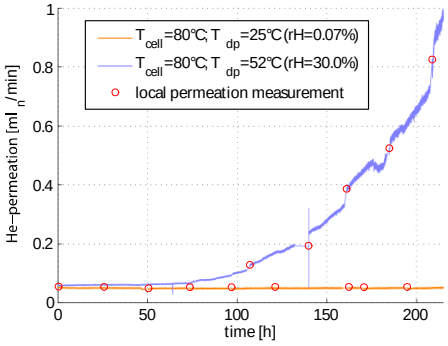

Figure 5. *Integral helium concentration at cathode outlet under counterflow and equal anode and cathode pressure of 1.5 bar.*

More detailed insight into the permeation characteristics of the membrane is available by local gas analysis under diffusive or convective conditions. The OCV-test under 0.07% rH showed constant diffusive helium permeation during the entire test (Fig. 6/7). Convective permeation was not present. Under humid condition, the MEA showed a combination of diffusive and convective helium transport. Diffusive transport was the dominating permeation mechanism at the begin of the test under humid conditions. This diffusive permeation rate was 1.5 times higher than under dry condition (Fig. 6). Evolution of local membrane defects after 100 h of OCV-test between gas ports 9 and 10 forced the local permeation. Both diffusive and convective helium transport increased due to these defects. The dominating transport mechanism switched from diffusive to convective permeation between 100 and 140 h of OCV degradation. Convective helium permeation was more than twice the amount of the diffusive permeation rate at the end of the OCV-test under humid conditions. Permeation does not only vary along the investigated channel in the middle of the flow field. It varies as well perpendicular to the flow field channel. This is clearly visible by comparison of the exit gas port of the middle channel (gas port 1) and the integral gas port at cell exit (gas port 0). Two possible sources lead to non equal permeation measurements at these ports: non uniform feed gas supply of the channels and different permeation characteristics of the middle and border of the active cell area. Further measurements have to clarify what dominates the different permeation behaviour of local and integral gas port.

Local permeation measurements illustrate, that integral gas permeation investigations can lead to misinterpretation of the membrane degradation. Membrane gas permeation is highly dependent on local defects. Humid conditions are considered more detrimental due to lower mechanical stability and swelling. Detailed measurements of local convective and diffusive gas transport under various operating conditions are necessary to fully understand membrane degradation mechanisms. Additional measurements under load are needed to correlate OCV-tests to real world applications.

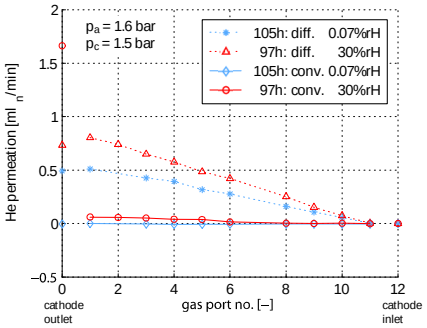

Figure 6. *Total permeation split in purely diffusive and purely convective helium permeation after the first 100h. Gas port 12 and 0 show the integral helium permeation at inlet and outlet of the cell.*

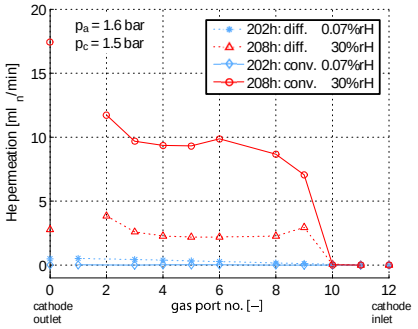

Figure 7. *Total permeation split in purely diffusive and purely convective helium permeation at end of the OCV-tests. Gas port 12 and 0 show the integral helium permeation at inlet and outlet of the cell.*

Conclusions

Local gas permeation during OCV degradation tests was measured by in-situ online mass spectrometry. Local permeation results showed that the combination of local defects, humidity conditions and local pressure gradients over the membrane govern the permeation characteristics. Humid conditions are considered more detrimental due to lowering of the mechanical stability of the membrane and higher local membrane defect probability.

Acknowledgement

We thank Thomas Gloor and Marcel Hottiger for their test rig support. Thanks as well to the Swiss Federal Office of Energy SFOE for financial support.

References

[1] S. S. Kocha, J.D. Yang, J.S. Yi, AIChE Journal **52**, 1916-1925 (2006).

Micro-patterning for PEFC: Single pulse laser ablation of aluminum films from glassy carbon

B.C. Seyfang, R. Fardel[1], T. Lippert, G.G. Scherer, A. Wokaun

phone: +41 56 310 2092, e-mail: bernhard.seyfang@psi.ch

Micro-fuel cells are a possible replacement for batteries as energy sources in portable devices. At PSI, a micro-polymer electrolyte fuel cell was developed, whose flow fields consist of micro-structured glassy carbon plates [1]. Micro-structuring of glassy carbon is carried out in a multi-step process. Single pulse laser ablation removes a sputtered aluminum mask selectively from glassy carbon, thereby defining micro-channels that are subsequently etched by reactive ion etching (RIE).

A pulsed XeCl excimer laser (308 nm) is used for the single pulse patterning of a metal mask on the glassy carbon. The influence of the excimer laser typical pulse to pulse energy fluctuations on the micro-structuring process must be known to minimize defects during RIE etching of the micro-channels.

Experimental

To obtain a better understanding of the processes occurring during ablation, ns-shadowgraphy was performed on glassy carbon samples with a sputtered, 570 nm thick aluminum film (Figure 1). The formation of a shockwave was observed, followed by a similar but much slower perturbation, and the subsequent release of fragments. The calculated velocities can be correlated with the energy release during ablation.

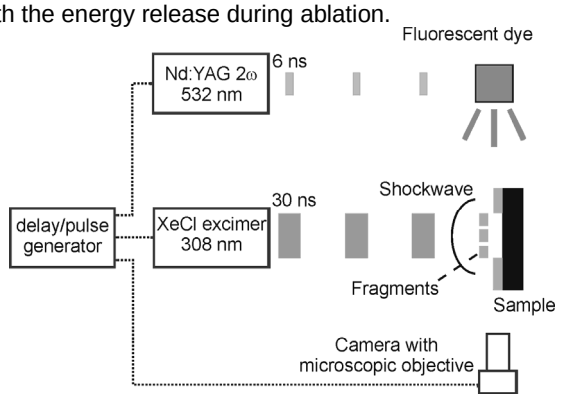

Figure 1. *Scheme of the ns-shadowgraphy arrangement. The delay generator controls the time difference between pump and probe laser to visualize the processes happening close to the surface of the sample at different time delays.*

The post-ablation examination of the samples by profilometry, optical microscopy, SEM, and EDX is used to measure the amount of removed material, the quality of the aluminum mask edges and aluminum residues on the glassy carbon surface.

Results

According to the post-ablation photographs, four different types of photon-material interaction can be classified as a function of laser fluence: no ablation, partial ablation, complete ablation, and over-ablation.

For fluences below 1.3 J/cm^2, no significant amount of aluminum is removed. Above this threshold, aluminum removal in significant amounts is observed, but only parts of the aluminum film are removed from the irradiated area. In areas where the Al is removed, the complete layer is ablated, as EDX measurements reveal. The remaining Al in the irradiated area forms bubbles.

At higher fluences (~3.0 J/cm^2), the aluminum is removed completely from the irradiated area and a minor ablation of glassy carbon is observed. A steep increase in the shockwave velocity is visible, compared to the values given for lower fluences.

When the fluence is increased above 3.0 J/cm^2, so-called over-ablation takes place. Next to the damaged edge of the aluminum mask, a several microns wide region is visible, that was not irradiated and where no aluminum is deposited. Inside the irradiated area, large droplets of molten and re-solidified aluminum are observed on the surface as can be quantified by EDX. This means for the following RIE process that remaining aluminum creates a shadowing effect and hinders defined etching.

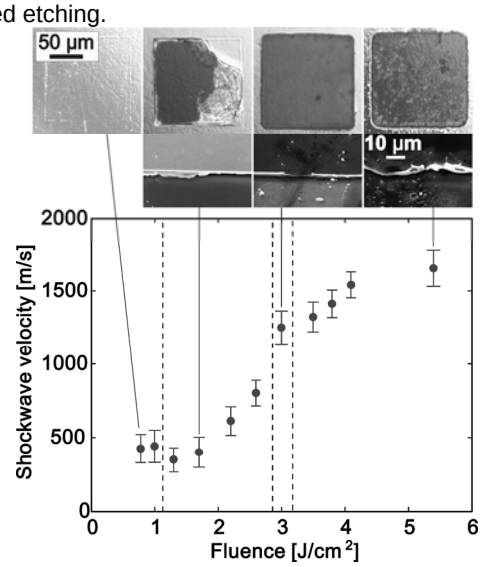

Figure 2. *Shockwave velocity as a function of laser energy density. Micrographs show the samples after ablation for selected fluences*

Because of pronounced differences in heat transfer coefficients, heat accumulates at the Al-GC interface that results in aluminum vaporization. The aluminum film is removed hereby. Observations like the formation of bubbles in the layer at lower fluence, aluminum deposition on the glassy carbon surface at higher fluence and the transition to a different ablation regime when full ablation takes place, support this hypothesis [2].

References

[1] B.C. Seyfang, M. Kuhnke, T. Lippert, G.G. Scherer, A. Wokaun, Electrochem. Commun. **9**, 1958-1962 (2007).

[2] B.C. Seyfang, R. Fardel, T. Lippert, G.G. Scherer, A. Wokaun, Appl. Surf. Sci., in press (2009).

[1] EMPA Dübendorf

Membrane swelling – an aspect of mechanical stability in the fuel cell

F. Wallasch, S. Rudin, L. Gubler, G.G. Scherer, A. Wokaun

phone: +41 56 310 2132, e-mail: frank.wallasch@psi.ch

The operation of a PEFC under realistic conditions, as expected for automotive applications [1], includes dynamic load changes, start/stop events, and freeze cycles. The start/stop cycles, for instance, include the fuel cell shut down and the start-up after a certain time without gas supply, heating, humidifying, and power output. For a polymer membrane, which is water swollen during the power generation due to a) the supply of humidified gas and b) the production of water in the fuel cell reaction ($2\ H_2 + O_2 \rightarrow H_2O$), the shut- down stops the water supply and production. During the lifetime of a FC, dynamic load changes are expected to occur more often than start/stop events (10^6 load changes vs. 10^5 start/stop cycles [1]) and the shift between high and low power also effect the membrane water content. The removal of the water, which acts as plasticizer, out of the polymeric network leads to shrinkage of the membrane. The spatial confinement of the membrane in the cell will lead to the formation of internal stress, and the accumulation of thousands of dry-wet cycles may eventually cause crack or pinhole formation and membrane failure.
The dimensional stability of a membrane measured as length variation, both in machining (MD) and transverse direction (TD), and thickness in wet and dry state allows the calculation of the area and volume change upon shrinking.

Preparation of fuel cell membranes

The membranes, based on poly(tetrafluoroethylene-*co*-hexafluoropropylene) FEP (DuPont Teflon® 100A) or poly(ethylene-*alt*-tetrafluoroethylene) ETFE (DuPont Tefzel® 100 LZ), were prepared by the pre-irradiation/graft polymerization/sulfonation sequence [1]. The graft polymerization without crosslinker was done in an isopropanol (50 vol%) and water (20 vol%) solution, using 30 vol% of an α-methylstyrene (AMS) / methacrylonitrile (MAN) mixture with a molar ratio $R_{m,sol.} = n_{AMS}/n_{MAN} = 1.5$. When diisopropenylbenzene (DIPB) was used as crosslinker, the volume of isopropanol was reduced by the volume of the added DIPB. The pre-irradiated film (3 kGy) was immersed into the grafting solution, and the polymerization was carried out under nitrogen at 50 °C for the different reaction times, needed to yield the given degree of grafting (*DoG)*. The grafted films were washed with acetone and dried under vacuum at 60 °C. The *DoG* was calculated as mass ratio of the grafted polymer and the initial mass of the base film. The grafted films were sulfonated at room temperature for 6 hours in a dichloromethane solution of chlorosulfonic acid and hydrolysed afterwards. The membranes were stored in water swollen state until further used.

FEP or ETFE – comparison of mechanical properties

The mechanical properties of grafted films were tested with a tensile machine (Zwick Roell). To obtain the Young's Modulus, a film strip (10 cm long / 10 mm wide) was stretched with constant speed (10 mm/min) in the elastic region (< 1 % strain), and to get the elongation at break, the experimental speed was set to 100 mm/min until the stripe ruptured. For each sample 10 stripes were tested. The influence of irradiation and grafting on the mechanical behaviour of grafted films was tested (Figure 1; film orientation in MD).

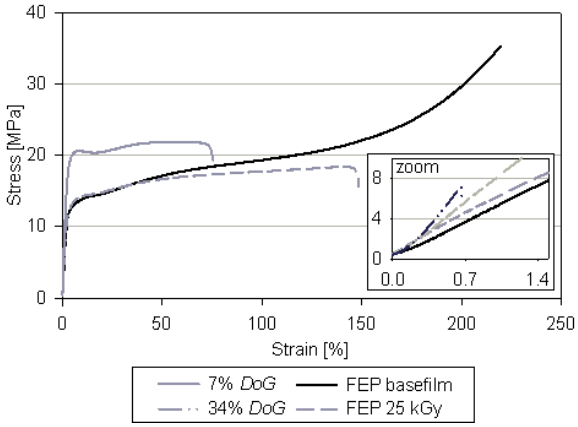

Figure 1. *Stress-strain curves of FEP-g-[AMS-co-MAN] films with four different DoG compared to the curves of the pristine and 25 kGy pre-irradiated FEP base film.*

The elongation at break decreases from 220 % for the pristine base film to 150 % for the irradiated film and finally to less than 2 % for a film with a fuel cell relevant *DoG* of around 30 %. The tensile tests of FEP based films suggested the change to ETFE as base film material. The comparison of some of the mechanical properties for both base films (Figure 2) clearly indicates the advantages of ETFE.

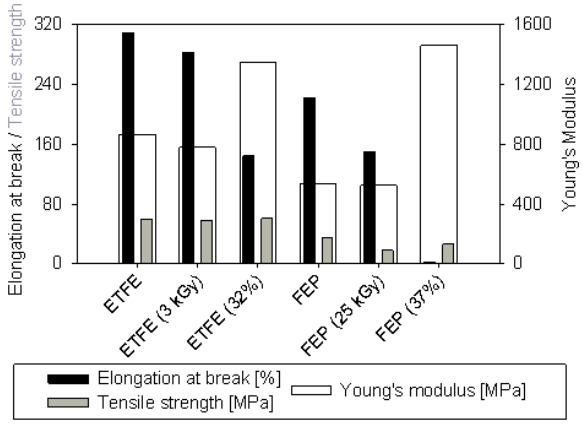

Figure 2. *Comparison of the elongation at break, tensile strength, and Young's modulus for ETFE and FEP and the influence of irradiation and grafting to PEFC relevant DoG.*

Intrinsically, the tensile strength for ETFE is higher as compared to FEP, and the elongation at break is less influenced by irradiation and grafting. After the grafting, the Young's modulus is higher for FEP. The mechanical properties of the membranes yield the same trend.

Dimensional stability

The dimensional stability of a fuel cell membrane is assumed to be important for its long term stability during swelling and shrinking. To determine the shrinkage, a rectangular piece of the wet membrane was punched out with the length $l_{0,MD}$ in MD, $l_{0,TD}$ in TD, and the thickness t_0, averaged over 5 measurements. The

membrane was dried for 2 hours under reduced pressure at 80 °C and the dry length in MD (l_{MD}), TD (l_{TD}), and the thickness t were measured five times and the linear shrinkages

$S_{MD} = 1 - l_{MD}/l_{0,MD}$,

$S_{TD} = 1 - l_{TD}/l_{0,TD}$, and

$S_t = 1 - t/t_0$, the area

$S_{area} = 1 - \frac{(l_{MD} \cdot l_{TD})}{(l_{0,MD} \cdot l_{0,TD})}$ and volumetric shrinkage

$S_{vol} = 1 - \frac{(l_{MD} \cdot l_{TD} \cdot t)}{(l_{0,MD} \cdot l_{0,TD} \cdot t_0)}$ were calculated.

The errors were calculated based on the variance of the length in MD, TD, and thickness. The relative errors are below 10 % and the error bars for clarity reasons not shown in the following graphs.

Uncrosslinked membranes based on ETFE

Uncrosslinked membranes with four different *DoG* (Figure 1) were prepared and subsequently tested to determine their shrinking properties. The contribution of the different directions (1-dimensional shrinkage; MD, TD, thickness) and the calculated 2-dimensional (area) and 3-dimensional (volumetric) shrinkage were determined and compared to those of Nafion® 212 (DuPont, Fig. 3).

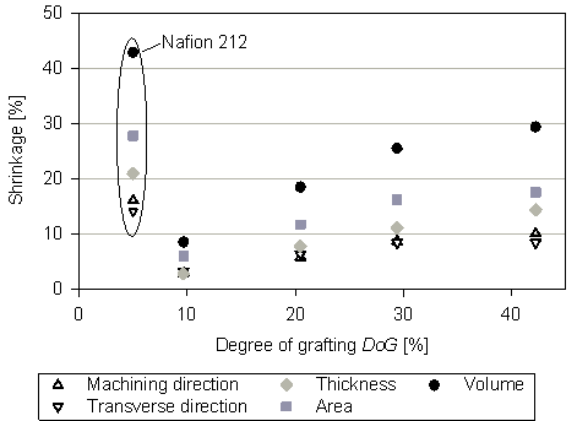

Figure 3. *Linear, 2-dimensional (area), and volumetric shrinkage of ETFE-g-[AMSSA-co-MAN] membranes compared to Nafion® 212 (DuPont).*

The ratio of the contribution in MD and TD (anisotropy) is approximately the same for all *DoG*s, increasing linearly until a *DoG* of 29 % and remaining constant until a value of 42 %. The shrinkage in thickness direction increases more strongly with the *DoG*, even above a *DoG of* 29 %.

DIPB-crosslinked membranes based on ETFE

The influence of crosslinking on the volumetric shrinkage was determined by the comparison of uncrosslinked and DIPB crosslinked membranes, prepared with different DIPB concentrations (c_{DIPB}) in the grafting solution (Figure 4). The membranes were synthesized to series with (10±1), (20±1), (30±2), and (40±2) % *DoG* with c_{DIPB} = 0, 0.7, 2.0, 4.0, and 6.6 mol% with respect to the total amount of AMS and MAN.

The volumetric shrinkage increases with increasing *DoG*. A higher amount of grafted and sulfonated polymer leads to a higher swellable fraction of the membrane and this yields a more pronounced shrinking upon drying. An increasing c_{DIPB} in the grafting solution is expected to give a higher DIPB concentration in the grafted film and, accordingly, in the membrane. The consequence of crosslinking is the formation of a three dimensional network, where the DIPB linkages between different polymer chains reduce the flexibility and elongation of polymer chains. As a result the swelling is limited.

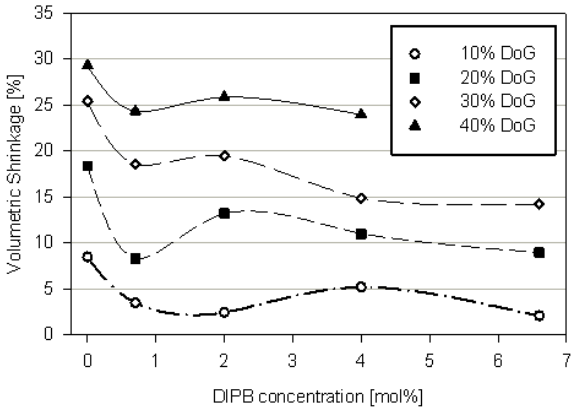

Figure 4. *Volumetric shrinkage of ETFE-g-[AMSSA-co-MAN-co-DIPB] membranes, prepared with different DoG and DIPB concentration in the grafting solution.*

The membranes prepared in a grafting solution containing 0.7 mol% DIPB show a particularly low swelling. This behaviour is not completely understood to date, but it seems that the in-plane shrinking (MD and TD) contributes more significantly to this phenomenon than the shrinkage over the membrane thickness. FT-IR spectroscopic measurements in ATR mode, which allow the differentiation between the bulk and surface concentration of DIPB, may yield insights into the behaviour of the membranes prepared in solutions containing low DIPB concentration.

Summary and Outlook

The elongation at break and the Young's modulus indicate that grafted films based on ETFE are tougher. The shrinkage of uncrosslinked ETFE based membranes up to a degree of grafting of 42 % is lower than that of Nafion 212. The resulting higher dimensional stability of the grafted membranes could explain the higher stability in a relative humidity cycling test. The crosslinking with DIPB reduces the shrinkage and enhances the dimensional stability. The influence of crosslinking on the shrinkage of membranes prepared with low DIPB concentrations seems to be more complex. The volumetric shrinkage of membranes with desired *DoG* for fuel cell applications (30 - 40 %) varies, depending on the base film and concentration of crosslinker used, from approximately 15 to 40 % *DoG*.

The interpretation of the behaviour of membranes prepared in solutions with less than 2 mol% DIPB has to be further investigated. Locally resolved measurements, such as confocal Raman- or FTIR-microscopy, may help to explain the phenomenon by understanding the crosslinker distribution.

References

[1] N.L. Garland, J.P. Kopasz J. Power Sources **172**, 94-99 (2007).

[2] L. Gubler, M. Slaski, A. Wokaun, G.G. Scherer Electrochem. Commun. **8**, 1215-1219 (2006).

[3] L. Gubler, M. Schisslbauer, PSI Electrochemistry Laboratory - Annual Report 2007, 16, ISSN 1661-5379 (2008).

The composition of grafted films measured by confocal Raman microscopy

F. Wallasch, L. Gubler, G.G. Scherer, Ch. Hierold[1], A. Wokaun

phone: +41 56 310 2132, e-mail: frank.wallasch@psi.ch

Important properties of the electrolyte membrane in a polymer electrolyte fuel cell (PEFC) are proton conduction, gas separation, and electronic insulation. Whereas the latter two are already present in the base film (FEP), proton conductivity is only introduced by the sulfonated graft copolymer [1]. The graft component should be distributed homogeneously through the thickness to ensure uniform membrane properties. For the mapping of the lateral distribution of the grafted component, FT-IR spectroscopy in transmission mode is applied [2]. The distribution over the film thickness is accessible via confocal Raman microscopy [3].

The preparation of the grafted films was done as described before [4], using pre-irradiated (25 kGy) poly(tetrafluoroethylen-*co*-hexafluoropropylene) FEP as base film. For the grafting of methacrylonitrile (MAN), 30 vol% of MAN were added to the solvent, in the case of the co-grafting of α-methylstyrene (AMS) and MAN, 30 vol% of the monomers were used at a molar ratio $R_{m,sol.} = n_{AMS}/n_{MAN}$ of 1.5. The integral degree of grafting *DoG* was calculated according $DoG = (m_{graft} - m_0) / m_0$, where m_0 is the mass before and m_{graft} after grafting.

Confocal Raman microscopy

Raman spectroscopy, based on the inelastic scattering of light (Raman effect [5]), is used to study vibrational and rotational modes of molecules.
The present study was carried out with a WITec alpha 300 R microscope[1], using a Nd-Yag-laser (λ = 532 nm, *P* = 4 mW) and an oil immersion objective (Zeiss, 100x/1.4 oil). The Raman spectrum of a FEP-*g*-[AMS-*co*-MAN] film (*DoG* = 34 %, molar ratio in the grafted polymer $R_{m,graft.}$ = 0.86), with a sampling time of 60 s is displayed in Figure 1.

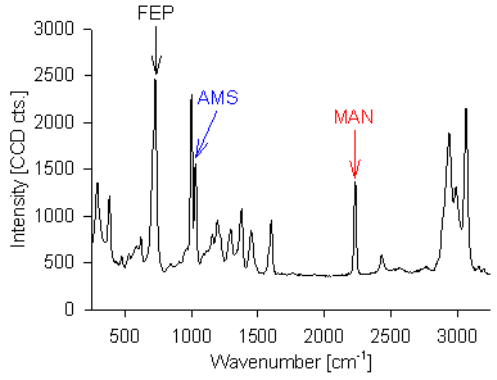

Figure 1. *Raman spectrum of FEP-g-[AMS-co-MAN] with 34 % DoG and $R_{m,graft.}$ = 0.86. The evaluated vibration bands for FEP (black), AMS (blue), and MAN (red) are labelled.*

The confocal configuration of a Raman microscope allows simultaneously the excitation and detection of a very small sample volume (ca. 1 µm^3) at different positions within the grafted film. To measure the distribution of the polymer components over the film thickness, the sample is displaced stepwise (1 µm) in the thickness direction. The number of depth steps is given by the thickness of the grafted film, which increases when the *DoG* increases. At each step 30 spectra were recorded over a lateral distance of 180 µm.

From intensity profiles to the local *DoG*

The confocal alignment of the Raman microscope allows the measurement of spectra at different positions within the grafted film. Lateral heterogeneity can be minimized by averaging the 30 spectra for each depth. By using an oil immersion objective, deviations due to different refractive indices of the film and the medium in the outside optical path are avoided. The quantification of the intensity loss based on scattering is elusive. The correction was done by assuming a constant FEP signal intensity for the vibration at 728 cm^{-1} and a linear decline over the film thickness. The measured and uncorrected intensity profile, shown as dotted blue line in Figure 2, for a FEP-g-MAN film with 2 % *DoG* was corrected (solid blue line) with the slope of the green line. The ratio of the corrected and uncorrected FEP signal was used to correct the intensity profiles of the MAN band (2235 cm^{-1}; red).

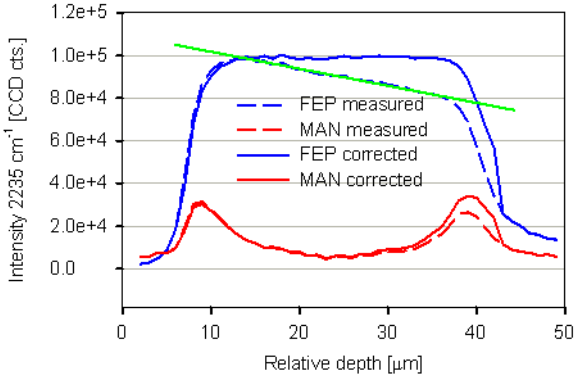

Figure 2. *Uncorrected (dotted) and corrected (solid) intensity profiles of FEP (black) and MAN (red). The slope of the straight line (green) was used for the correction.*

The *local* DoG_X for component *x* at the depth *i* was calculated from the integral DoG_x, in case of co-grafted films with regard to the $R_{m,graft.}$, by the ratio of the signal intensity at the considered depth $I_{x,i}$ to the sum of the intensities over the film thickness $\sum I_{x,i}$, according to the equation $local\ DoG_x = DoG_x \cdot \left(I_{x,i} \Big/ \sum_{bottom}^{top} I_{x,i} \right)$.

FEP-*g*-MAN as model graft polymer

As the grafting of AMS is not possible under the given reaction conditions, MAN grafting onto pre-irradiated FEP is the simplest system to be investigated. In Figure 3, the intensity profiles of the signals at 728 cm^{-1} (FEP, CF-stretching vibration; used to identify the film surfaces) and 2235 cm^{-1} (MAN, CN-stretching vibration) of films with different *DoG* are shown, using 5 s sampling time for each spectrum. The signal intensity is given by colour intensity, where black is the lowest and yellow the highest intensity.

[1] ETH Zürich

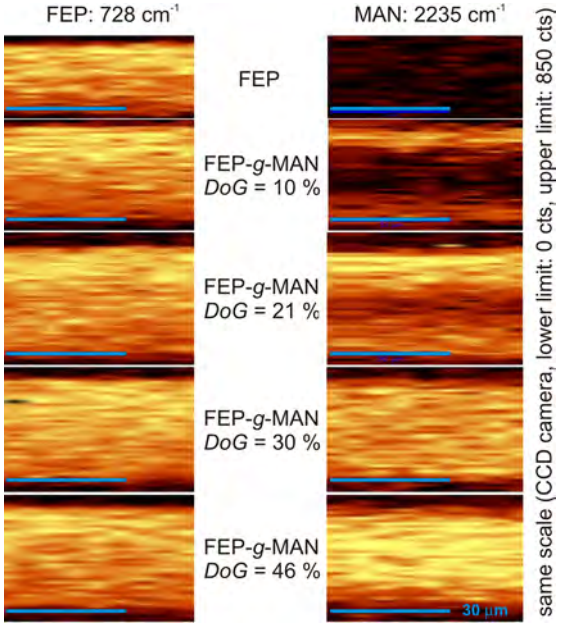

Figure 3. *Intensity profiles of FEP and MAN based vibrations for different DoG. A lateral section of 50 µm and the film thickness is shown for each sample.*

For the films with *DoG*s < 30 %, the grafting fronts are visible at both surfaces. For five different FEP-*g*-MAN films, the local *DoG*, based on the CN-vibration at 2235 cm^{-1}, is plotted against the depth in Figure 4.

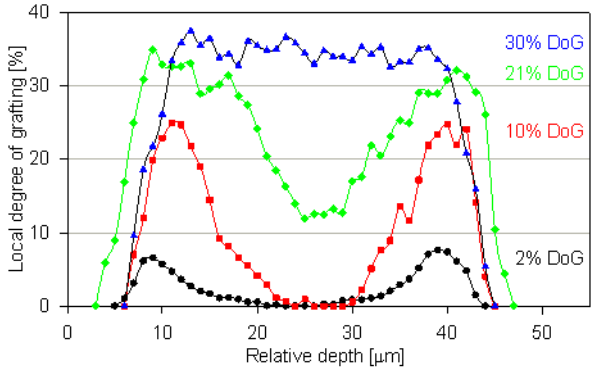

Figure 4. *Laterally averaged local DoG for FEP-g-MAN films with integral DoG from 2 to 46 %. The film centres placed at 25 µm.*

The local *DoG* for films with integral *DoG*s up to 21 % is significantly higher close to the surface than at the film centre. Only the film with 30 % *DoG* shows homogenous grafting over the film thickness, with a variation at the film surface. This variation may be caused by an uneven alignment of the film and / or a rough surface, which both complicate the definition of an exact surface position.

The intensity profiles for FEP-*g*-[AMS-*co*-MAN]

The corrected intensity profiles of the AMS and MAN based vibrations for different *DoG* (15, 24, 35, 44 % and $R_{m,graft.}$ = 0.95 ± 0.10) are shown in Figure 5.

The intensity profiles show a homogenous distribution for both graft components. This may be caused by the different reaction rates for the grafting of MAN and the co-polymer (AMS-*co*-MAN). The time necessary to reach a *DoG* of 46 % takes 14 h in the case of MAN and 48 h for the grafting of the copolymer.

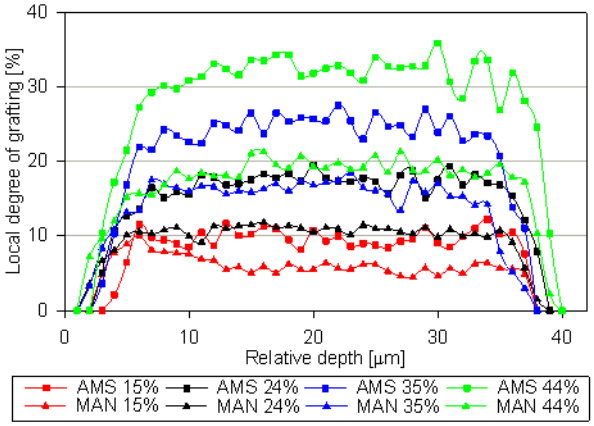

Figure 5. *Local DoG for AMS and MAN for FEP-g-[AMS-co-MAN] films with four different DoG and $R_{m,graft.}$ = 0.95 ± 0.10.*

Summary and Outlook

We assume for both cases, the grafting of MAN and the co-grafting of AMS and MAN, that the grafting occurs via the front mechanism [6] and AMS and MAN have comparable diffusion rates in the grafted film. As a consequence, the results can be explained by the different reaction times required to reach the same *DoG* for the grafting of MAN and the co-polymer, respectively. If the diffusion is slow, compared to the polymerization, then all the monomers at the grafting front will react immediately and the concentration profiles will be more expressed. This may be the case for the grafting of MAN, where it takes 4 h to reach a homogenous distribution (30 % *DoG*). If the diffusion is fast compared to the polymerization, then the monomer concentration during the grafting and also the monomer distribution in the grafted film should be more homogeneous. The grafting of 15 % [AMS-*co*-MAN] is reached after 9 h, which is, assuming comparable diffusion rates, more than a factor two of the time necessary to reach a homogeneous distribution in the case of MAN, if the grafting is controlled by diffusion.
The determination of the monomer diffusion rate into the film will allow a better understanding of the irradiation grafting. The separation of the two coupled contributions to the grafting process, i.e. diffusion and polymerization, can be realized by measuring the diffusion of the monomers in already grafted films as a function of their *DoG* and $R_{m,graft.}$. The calculation of the local *DoG* with the diffusion rates for the monomers and their comparison with the local *DoG* obtained from confocal Raman depth profiles will allow a more precise determination of the polymerization kinetics.

References

[1] M.V. Rouilly, E.R. Kötz, O. Haas, G.G. Scherer, A. Chapió, J. Membrane Sci. **81**, 89-95 (1993).

[2] H.-P. Brack, D. Fischer, G. Peter, M. Slaski, G.G. Scherer, J. Polymer Sci. Part A **42**, 59-75 (2003).

[3] H. Matic, A. Lundblad, G. Lindbergh, P. Jacobsson, Electrochem. and Solid State Let. **8**, A5-A7 (2005).

[4] F. Wallasch, M. Slaski, L. Gubler, A. Wokaun, G.G. Scherer, PSI Electrochemistry Laboratory - Annual Report 2006, 16, ISSN 1661-5379 (2007).

[5] V. Raman, Nobel Lectures, Physics 1922-1941, Elsevier Publishing Company, Amsterdam (1965).

[6] B. Gupta, F. N. Büchi, M. Staub, D. Grman, G.G. Scherer, J. Polymer Sci. Part A **34**, 1873-1880 (1996).

FUEL CELLS

DIAGNOSTICS

A 2D impedance model for low humidity polymer electrolyte fuel cells

M. H. Bayer, A. Wokaun, G.G. Scherer, I. A. Schneider

phone: +41 56 310 5304, e-mail: michael.bayer@psi.ch

Electrochemical Impedance Spectroscopy (EIS) is a widely used method for the characterization of Polymer Electrolyte Fuel Cells (PEFCs). By using EIS one can distinguish between processes, which occur on different time-scales and gain insights into factors limiting the cell performance.
AC impedance models for PEFCs published in the literature [1] take into account only processes across the membrane electrode assembly (MEA) and, therefore, they are 1-dimensional. Processes along the flow channels, namely reactant depletion and water accumulation have been neglected so far. However, these processes become limiting at finite gas flow rates and, therefore, they must undoubtedly be taken into account for the interpretation of PEFC impedance spectra [2-5]. Recently, we were able to give experimental proof that the formation of low frequency inductive loops in PEFC impedance spectra under sub-saturated conditions is associated with the slow hydration/dehydration of the polymer electrolyte with ac current and a varying ionic resistance of the polymer electrolyte [5, 6]. These results have shown that reactant and water concentration oscillations build up along the flow channels, as a consequence of ac current. As a result, the ac current in upstream parts of the cell affects the impedance response in downstream regions [2-5]. Based on these experimental findings, we present a 2-dimensional ac impedance model for a low humidity PEFC.

The Model

The model takes into account processes in two spatial dimensions: i) processes across the membrane (through plane) and, ii) processes along the flow channel (in plane). The large aspect ratio of the cell [2], which exhibits a flow field length of more than 30 cm, justifies the use of a pseudo 2-dimensional or 1+1 dimensional model approach [7]. In this approach the through- and in plane direction are treated separately.

Through plane, across the membrane, a multilayer model is used, which accounts for gas channels, gas diffusion layers (GDLs), catalyst layers, and the membrane. Diffusion and electro osmotic drag are the mass transport mechanisms considered here. The cathode is treated as an interface; the oxygen reduction reaction (ORR) is assumed to obey Tafel's law. Anode overpotential losses are neglected.

In plane, along the channel, the 1-dimensional through plane sub models are coupled solely through downstream convective transport in the flow channel.

The key points in the model, which have major influence on the results, are the following:

1. The local proton conductivity of the polymer electrolyte σ depends on its water content λ (Eq. 2) [8]:

$$\sigma(\lambda) = (0.005738\lambda - 0.007192) \quad (1)$$

   leading to a water dependent membrane resistance *R,* since (t_M = membrane thickness)

$$R = \int_0^{t_M} \frac{1}{\sigma(\lambda(y))} dy \quad (2)$$

2. The local current density depends on the electric potential but also on the species distribution. The concentration of reactants and water at the electrode defines the concentration overpotential, and the water concentration profile in the polymer electrolyte defines the membrane resistance.
3. Local water production rates at the cathode and electro osmotic drag in the polymer electrolyte depend on current density.
4. Water and reactants are not only transported through plane but also in plane by the convective flow in the flow channel

Consequently, local current density depends highly on the water concentration profile across the membrane but also on the species concentration transported in the flow channel. Hence, a change in local current density can originate from a change in potential, but also from changing species concentration in the channel due to the electric current occurring in upstream parts of the cell.

For steady state calculations the system of transport equations has to be solved self consistently, using the species concentrations in the channel of the upstream segment and the electric potential as input parameters. The result of this calculation is the through plane species concentration profile and the current density for a given position along the channel.

One can write down the through plane equation of motion as a linear system of equations in the form

$$\dot{c} = M \cdot c + b, \quad (3)$$

where *M* contains the transport coefficients, while *b* contains the source terms, including the water produced in the cathode by the ORR and the upstream species concentration. The working point of the cell is given by the electric potential, which is assumed to be homogeneous along the channel, because of the high electric conductivity. For the steady state case, the nonlinear set of equations is solved using Newton-Raphson method.

Calculation of the cell impedance

The steady state solution defines the parameters for the impedance model. The impedance is defined as the linear response function of the potential to a current perturbation (Eq. 4).

$$Z(\omega) = \frac{\eta(\omega)}{j(\omega)} \quad (4)$$

The impedance can be calculated by Fourier transformation of the whole system of equations with

respect to time. Even though equation (3) is linear, the whole set of equations is highly nonlinear, since *b* contains the current, which itself depends on the solution of (3). Hence, linearization of the whole set of equations is necessary to obtain through plane a true linear system leading to a short calculation time for any frequency.

Alternatively, the transient response of the local current densities to a perturbation in voltage can be calculated in time domain and subsequently be transformed to Fourier space. This method has the advantage of being very flexible with respect to the type of perturbation signal, yet, needs extensive computation time for low frequency calculations. The results shown here were calculated by using a potential step of 1mV.

Results

All calculations were made for partially humidified hydrogen and dry oxygen in co-flow mode. The 2-dimensional ac impedance model can qualitatively describe the experimental results [5]. As shown in Figure 1, area specific resistance decreases with current density, as well as along the flow channels, due to water formation and accumulation along the flow field and, hence, an improved hydration of the ionomer by product water. This leads to an increasing current density from inlet to outlet for all potentials, as shown in Figure 2.

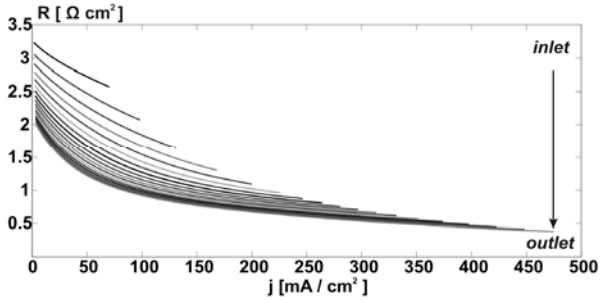

Figure 1. *Calculated local area specific resistance curves plotted over local current density along the flow channels*

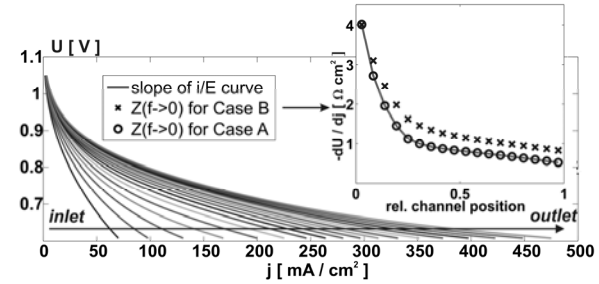

Figure 2. *Calculated local i/E curves as a function of channel position and local polarization resistance (inset).*

The contribution of channel processes to PEFC impedance response is demonstrated in Figure 3 and 4. For the calculation of the local spectra, as shown in Figure 3 (case A), the effect of ac current on the water and reactant concentration in the gas channels and the convective transport of gas concentration oscillations along the flow channels was taken into account, whereas their transport was neglected in case B (Figure 4). Therefore, case B effectively disregards the effect of water accumulation and reactant depletion along the flow channels on ac impedance response. Consequently, the local polarization resistance, as obtained from the low frequency intercept of the respective local spectra, is consistent with the slope of the local i/E curves only in case A (inset in Figure 2).

The result shows that 1-dimensional EIS models are not sufficient to describe the impedance response of a PEFC, which is operated under sub-saturated conditions at finite gas flow rates [5]. The contribution of channel processes must be taken into account and 2-dimensional PEFC impedance models are required to account for these effects [2-5].

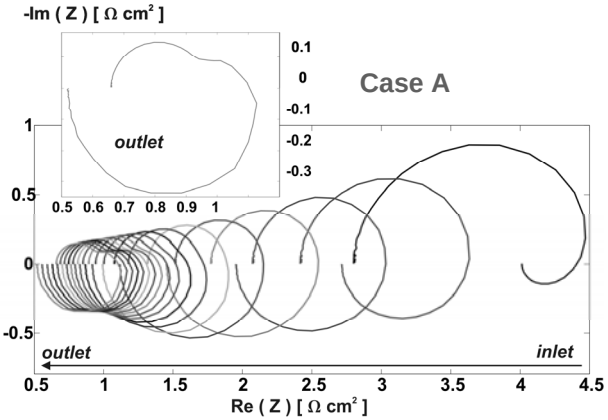

Figure 3*. Calculated local impedance spectra for the case that the build up of gas concentration oscillations along the flow channels is considered. (3.97 kHz to 50 µHz). The outlet segment is shown in the inset.*

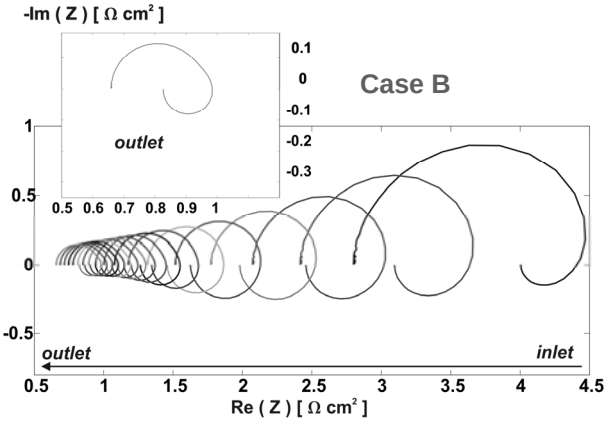

Figure 4. *Calculated local impedance spectra for the case that gas concentration oscillations in the gas channels are not carried downstream (3.97 kHz to 50 µHz). The outlet segment is shown in the inset.*

References

[1] P.M. Gomadam, J.W. Weidner, Int. J. of Energy Res. **29**, 1133 (2005).

[2] I.A. Schneider, G.G. Scherer, 'Local Transient Techniques in PEFC Diagnostics' in "Handbook of Fuel Cells" **5**, W. Vielstich, H.A. Gasteiger, H. Yokokawa, Editors, John Wiley & Sons, New York (2009).

[3] I. A. Schneider, S. A. Freunberger, D. Kramer, A. Wokaun, G.G. Scherer, J. Electrochem. Soc., **154**, B383 (2007).

[4] I.A. Schneider, D. Kramer, A. Wokaun, G.G. Scherer, J. Electrochem. Soc. **154**, B770 (2007).

[5] I.A. Schneider, M.H. Bayer, P. Boillat, G.G. Scherer, ECS Transactions **11**, 461 (2007).

[6] I.A. Schneider, M.H. Bayer, A. Wokaun, G.G. Scherer, J. Electrochem. Soc., **155**, B783-B792 (2008).

[7] P. Berg, K. Promislow, J. St. Pierre, J. Stumper, B. Wetton, J. Electrochem. Soc., **151**, A341-A353 (2004).

[8] A.A. Kulikovsky, J. Electrochem. Soc., **150**, A1432-A1439 (2003).

Passive hybrid architecture for fuel cell powertrains

J. Bernard, M. Hofer, F.N Büchi

Phone: +41 56 310 5588 e-mail: jerome.bernard@psi.ch

Fuel Cell Hybrid Vehicles use two energy sources for supplying their powertrain: a polymer electrolyte fuel cell which converts hydrogen into electrical power, and an energy buffer, typically a battery, which is power reversible. The two main roles of the energy buffer are to power assist the fuel cell system and to recover the energy during vehicle braking. In the hybrid powertrain, there are two main possibilities for connecting the FC system and the energy buffer (Figure 1):

- Active hybrid: one or two DC/DC converters are used to actively control the power sharing;
- Passive hybrid: the fuel cell system is directly connected to the battery. The power sharing cannot be controlled and is imposed by the internal impedance of each device.

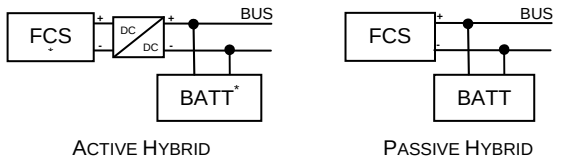

FCS: Fuel cell system; BATT: Battery.

Figure 1. *Illustration of active and passive hybrid architectures.*

Although active hybrids are almost exclusively retained in powertrain designs, passive hybrids may bring advantages that should be explored.

Advantages/drawbacks of passive hybrids

In the passive hybrid, the fuel cell system is directly connected to the battery and therefore the two components operate at the same voltage. This causes two main disadvantages: 1) the specifications are highly constrained because the voltage ranges of the two devices have to match [1], and 2) active power sharing is impossible. The state of charge (SOC) of the battery is uncontrolled, so overcharges and deep discharges can only be avoided by restricting the load power.

However, as there are no DC/DC converters, a passive hybrid is cheapest, simplest, and the power losses in the hardware are eliminated. To partially overcome the problem of passive power sharing without compromising the benefits mentioned, a plug-in / plug-out capability of the fuel cell system can be added (Figure 2).

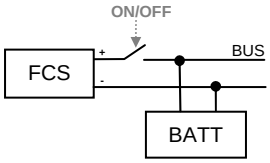

Figure 2. *Passive Hybrid with FC system plug-in capability.*

Experimental validation

Considering the plug-in/plug-out capability of the fuel cell system, the goal of the experiments was to verify that 1) the power demand can be fulfilled and 2) the battery SOC can be controlled in the same time. To do this, a Hardware in the Loop (HiL) test bench was used [2].

An example of the results is given in Figure 3. The hybrid power source is composed of a 600 W fuel cell system and a 27.3V/4Ah Li-ion battery. The profile of the power demand is derived from a light-duty vehicle driving the Zürich-Pendler cycle. The rule for plug-in/plug-out the fuel cell system is based on a thermostatic controller:

- If SOC increases above 75%, unplug the FC system;
- If SOC decreases under 65%, plug the FC system.

Figure 3 clearly shows that using this simple control strategy, SOC control can be achieved while satisfying the power demand of the load.

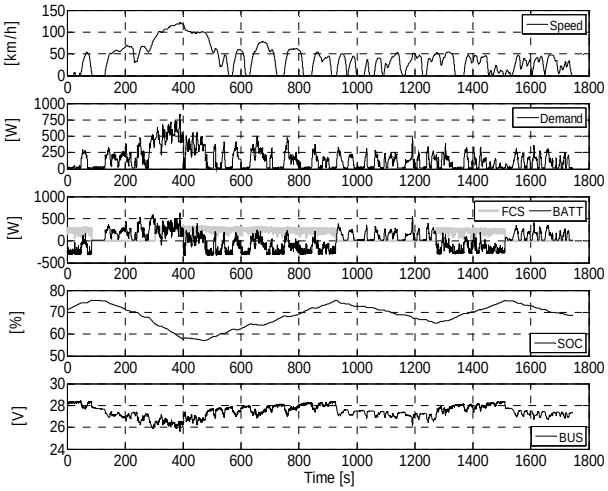

Figure 3. *HiL result of a passive hybrid powertrain.*

Conclusion

This study is a first step in evaluating passive hybrid powertrains for FC vehicle drivetrain design. Although passive hybrids offer a reduced complexity, it requires careful consideration when sizing the FC system and the battery. To keep a minimal control on the power sharing, FC plug in/plug out capabilities can be considered.

References

[1] L. Gao, Z. Jiang, R.A. Dougal, IEEE Transactions on Aerospace and Electronic Systems **41**, 346-355, (2005).

[2] J. Bernard, S. Delprat, T.M Guerra, R.Kötz., F.N. Büchi, PSI Electrochemistry Annual Report 2007, 23, ISSN No. 1661-5379 (2008).

Determination of liquid water distribution in PEFC by X-ray tomography

R. Flückiger, D. Tehlar, F. Marone, M. Stampanoni, A. Wokaun, F.N. Büchi

phone: +41 56 310 4189, e-mail: reto.flueckiger@psi.ch

Understanding the mass transport properties of the gas diffusion layer (GDL) is essential to understand local degradation and to improve the water management and the power density in the high current domain. GDL's are structured to fulfill a multitude of requirements. They have to allow access of reactants to the catalyst layer (CL) and removal of gaseous and liquid product water. Therefore they are highly porous and hydrophobized with polytetrafluorethylene (PTFE). Furthermore electrons need to be collected or distributed at the CL's. GDL's need therefore to be based on a conducting substrate, which is chemically inert (e.g. carbon fibers). Assuming no transport bottleneck in the CL, the strongest limitation comes from the flooding of GDL pores with liquid water and a subsequent shortage of oxygen in the cathode CL. Liquid water and transport thereof in the GDL has therefore been widely investigated [1-3].

Methodology

X-ray radiography with a resolution of 3 μm [4] and tomography with 10 μm resolution [5] have been used earlier to study water in GDL's. In this work x-ray micro tomography at the Tomcat beamline of the Swiss Light Source has been employed. For the first time the structure of the water has been resolved in 3D with a resolution of 1 μm. Special sample holders were developed for the small samples, which were required due to the limited field of view at this resolution. Figure 1 shows the experimental setup and a radiogram of a GDL sample. Water with defined pressure was applied from the bottom to the sample. The stamp is screwed into the cup to hold and seal the sample at the periphery.

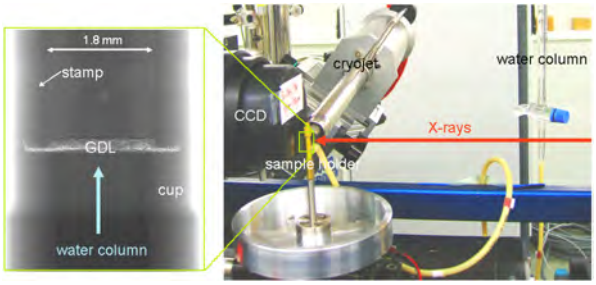

Figure 1. *(right) Experimental setup for the water filling experiment. The water column is connected with a tube to the rotating sample holder. (left) radiogram of sample holder and GDL sample at 10 keV.*

Figure 2 shows the resolution and contrast which are possible with the phase contrast method [6]. A clear contrast between the three different phases (air, fiber, water) and a low noise are required in order to separate the phases during image processing.

Results and Discussion

Figure 3 shows a reconstructed vertical (through-plane) slice of a TGP-H-060 (20% PTFE) GDL recorded with the phase absorption method. The structure of the solid, voids, and water can be clearly identified.

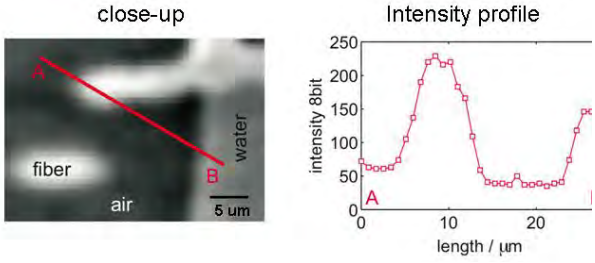

Figure 2. *(left) Close-up of 2D through-plane slice of a GDL containing water. Measured with phase contrast method at 30 keV; (right) intensity diagram along line A-B in close up showing the distinct intensity level of the three different phases and the low noise.*

The proceeding water front as function of filling pressure is clearly visible. On the bottom of the individual pictures in Figure 3 the threshold-estimated porosities and the saturations are given.

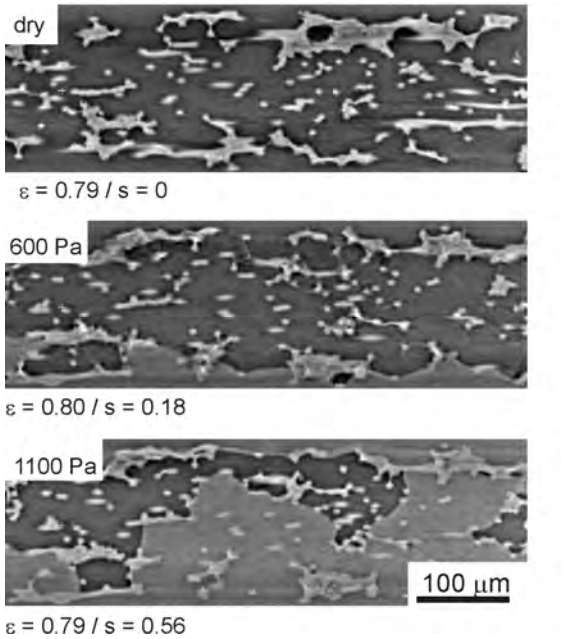

Figure 3. *Through-plane slices of a TGP-H-060 (20% PTFE) tomography measured with phase contrast method at 30 keV; (top) dry; (middle) filled with liquid water pressure of 600 Pa; (bottom) filled with liquid water pressure of 1100 Pa. labels below the pictures indicate porosity (ε) and saturation (s).*

The porosity and local liquid saturation as function of the GDL thickness may be obtained for different water pressures. The local saturation is an important parameter determining the local diffusivity and permeability of these porous materials. In Figure 5 the saturation is shown as a function of position within the GDL. The porosity, which is also shown for all measurements, is a quality criterion of the phase separation. It can be seen that upon increasing the water pressure, the water is retained at the layers of higher density before a breakthrough to the center of the GDL or out of the GDL occurs. For these Toray TGP-H-

060 (20% PTFE) materials a maximum average saturation of ca. 60% is observed. When the sample is purged with air only little water is removed. This is counter-intuitive because one would assume that a hydrophobic material has no water retention ability. This effect is possibly influenced by other parameters such as PTFE distribution, which strongly affects the local contact angle between solid and water. Another explanation could be the high porosity layer in the middle, which acts as a water trap.

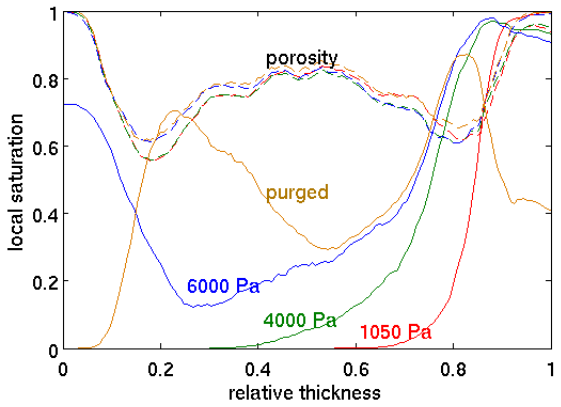

Figure 4. *Porosity and saturation of TGP-H-060 (20% PTFE) over the entire sample size. Water is filled from the right side; with water pressures indicated. at 6000 Pa break through to gas-side surface is observed. "purged" curve is after through-plane purging of the GDL with air for about 10 seconds.*

The assumption of a fully saturated catalyst layer may not always be true and gaseous water can be transported in large fractions through the GDL. The sample holder has therefore been further adapted to run an electrochemical active cell with an area of 7 mm^2. For this 0.4 mm gold wires were connected to the GDL on both sides of an MEA. The cell was connected with a saturated hydrogen and oxygen reservoir. An external load with a constant resistance was applied until the effect of flooding could be observed. Figure 6 shows a through-plane slice of an x-ray tomography of the cell after flooding occurred. The platinum in the CL's resulted in a high absorption and therefore a high grayscale value (white). In between the two CL's the membrane is visible. Adjacent to the CL's the anode and cathode GDL's with water filled pores can be seen.

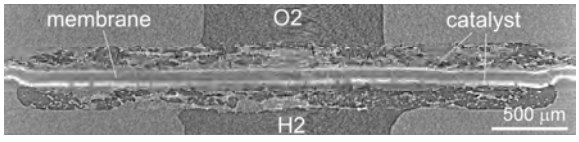

Figure 6*. Through-plane slice of a catalyst coated membrane and two GDL's in a special sample holder. Water is observed as the light gray phase in the GDL's.*

It is difficult to obtain the same resolution and contrast for complete cells as for the components only. However, qualitatively a similar water distribution as for single GDL's is observed. In Figure 7 the local saturation of different active cell experiments is shown over the thickness of the cell (slice number). Qualitatively the profiles are similar to the ex-situ measurements but the catalyst layer saturation around slice 50 is always smaller than one. Different GDL configurations were examined for different amounts of product water. The produced liquid water is measured in terms of cathode pore volume. As expected the active cells with unteflonated GDL's had the highest level of saturation. The lowest saturation profile was observed for the GDL with 20% PTFE and a micro porous layer (MPL) despite the fact that the amount of water produced was the highest (5.49x). The increase in saturation from the anode catalyst to the anode channel can be explained with the electo-osmotic drag towards the cathode.

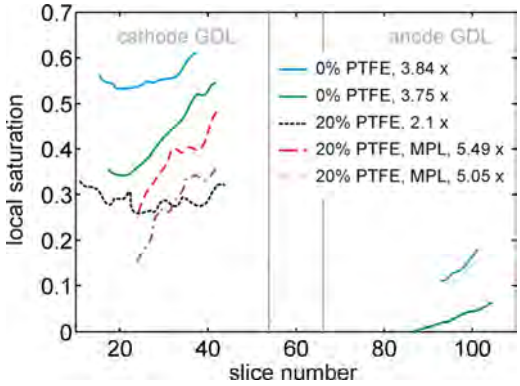

Figure 6*. Saturation profiles of different active cell x-ray tomography scans. The slice number is a measure for the thickness. The number in the legend indicates the amount of reactant water produced: 1x is the pore volume of the cathode GDL.*

Conclusions

X-ray micro-tomography can provide qualitative and quantitative insights into the structure of the water in porous gas diffusion layers of polymer electrolyte fuel cells. The saturation as a function of the GDL thickness shows that the filling of the porous layers is inhomogeneous. When filling the dry GDL, the water is retained by dense layers at both surfaces. When a wet layer is purged, the dense layers trap the water and a significant saturation remains. Preliminary experiments have shown that the same measurements are possible with complete cells. X-ray micro-tomography can be developed to be a versatile tool for investigating the behavior and state of water in porous transport layers and active cells with an unprecedented resolution.

References

[1] T. Koido, T. Furusawa, K. Moriyama, K. Takato, ECS Transactions **3**, 425 (2006).

[2] J. Zhang, D. Kramer, R. Shimoi, Y. Ono, E. Lehmann, A. Wokaun, K. Shinohara, G.G. Scherer, Electrochim. Acta **51,** 2715 (2006).

[3] A. Bazylak, D. Sinton, Z. Liu, N. Djilali, J. Power Sources **163**, 784 (2007).

[4] I. Manke, Ch. Hartnig, M. Grünerbel, W. Lehnert, N. Kardjilov, A. Haibel, A. Hilger, J. Banhart, H. Riesemeier, Appl. Phys. Lett. **90**, 174105 (2007).

[5] P.K. Sinha, P. Halleck, C.-Y. Wang, Electrochem. Solid-State Lett. **9,** A344 (2006).

[6] A. Groso, R. Abela, M. Stampanoni, Opt. Express **14**, 8103 (2006).

Influence of temperature and humidity on start/stop induced degradation in polymer electrolyte fuel cells

N. Linse, A. Wokaun, G.G. Scherer, L.Gubler

phone: +41 56 310 4668, e-mail: nicolas.linse@psi.ch

Besides the high costs, the poor durability under dynamic operating conditions is the main barrier for a commercial use of Polymer Electrolyte Fuel Cells (PEFCs). For most applications, dynamic operation includes the frequent start-up and shut-down of the fuel cell. However, uncontrolled start-up and shut-down by anode air purging leads to elevated cathode potentials due to the formation of a hydrogen/air front in the anode electrode compartment [1]. The occurring potentials can reach values up to 1.5V and cause corrosion of the carbon catalyst support material. This results in a substantial loss of active cathode catalyst surface area and a consequential decrease in fuel cell performance. In contrast to the cathode, the anode electrode is not exposed to elevated potentials during start/stop processes. Hence, the anode catalyst degradation is negligible. Investigating the influence of fuel cell operating parameters on the start/stop induced degradation is a prerequisite for the development of operation strategies which can mitigate degradation under dynamic conditions.

Experimental

To determine the influence of humidity and temperature on the degradation, start/stop cycling experiments were carried out. All experiments were performed using a 16cm^2 cell with a parallel flow field and MEAs fabricated by hot pressing of a Nafion 212 membrane and ETEK 140W electrodes (0.5mgPt/cm^2). The cells were operated with hydrogen and air in stoichiometric mode (1.5/2.0, minimum gas flow 600ml/min) at a gas pressure of 3bar$_a$. During all experiments an external load of 0.2Ω was applied. To perform start/stop cycling, the anode electrode was alternately purged with hydrogen and air (60s each). The influence of humidification was investigated by cycling three cells at different humidifications and a constant temperature of 80°C. To determine the influence of temperature, the cells were operated at 40°C, 80°C, and 95°C with fully humidified gases. Degradation behaviour was characterized by determining the active Pt catalyst surface area by CO stripping voltammetry.

Results

The reactant gas humidity has a notable influence on the degradation rate (cf. Figure 1). The strong increase of start/stop durability with decreasing humidification has two main reasons. On the one hand, a decreased humidification leads to lower water content in the membrane. The resulting increase of the membrane resistance reduces the detrimental cathode potentials and consequently leads to a lower degradation rate. Moreover, two water molecules are needed for the corrosion of one carbon atom (cf. Equation 1). Therefore the carbon corrosion reaction rate strongly depends on the water content in the cell.

$$C + 2H_2O \rightarrow CO_2 + 4H^+ + 4e^- \quad (1)$$

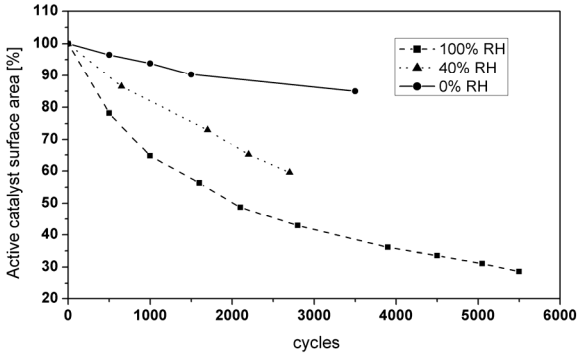

Figure 1. *Decrease of active cathode Pt surface area for cells operated at different reactant gas humidities.*

Surprisingly, the experiments show no influence of the temperature on the degradation rate (cf. Figure 2). This result is contradictory to similar results obtained by potential cycling for catalyst durability tests [2, 3]. The reason for this discrepancy is not clear yet. Possible explanations are (i) the different electrode materials used or (ii) differing degradation mechanisms for potential cycling tests and start/stop cycling experiments using anode gas purging as described here.

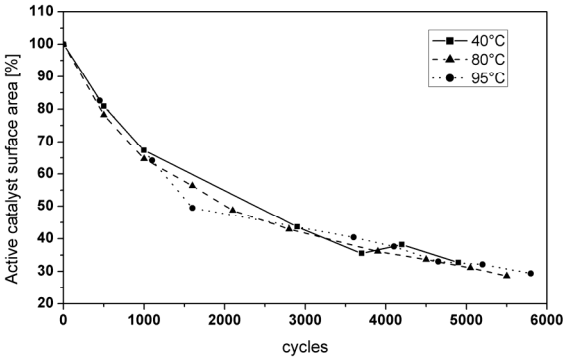

Figure 2. *Decrease of active cathode Pt surface area for cells operated at different temperatures.*

Conclusions

The results show that gas humidity strongly influences start/stop induced degradation. Consequently, it would be beneficial to reduce humidification during shut-down and start-up processes. Contrary to prior published experiments, a temperature effect on the degradation rate was not observed.

References

[1] C.A. Reiser, L. Bregoli, T.W. Patterson, J.S. Yi, J.D. Yang, M.L. Perry, T.D. Jarvi, Electrochem. Solid-State Lett. **8** (6), A273-A276 (2005).

[2] W. Bi, T.F. Fuller, J. Electrochem. Soc. **155**(2), B215-B221 (2008).

[3] R. Borup, DOE Hydrogen Program Review (2005). www.hydrogen.energy.gov/pdfs/review05/fc40_borup.pdf

Adapted flow field geometry for PEFCs

M. Reum, A. Wokaun, F.N. Büchi

phone: +41 56 310 2411, e-mail: felix.buechi@psi.ch

This work describes a new kind of flow field layout for polymer electrolyte fuel cells (PEFC) and first experiments carried out with this design. The idea of optimizing the channel/rib geometry to the conditions at a specific coordinate between inlet and outlet of the cell emanates from the results of current distribution measurements on the scale of channels and ribs [1, 2]. These experiments had revealed that membrane drying is a loss mechanism that is found predominantly under the gas channel, and oxygen starvation is primarily observed seen in the rib covered cell areas for low oxygen partial pressures [1]. Since the inlet regions of the fuel cell are prone to membrane drying – while the outlet regions suffer from poor oxygen supply – it seems reasonable to adapt the channel/rib geometry to the along-the-channel position of a technical size PEFC.
Previous sub-mm current distribution measurements have shown that geometries with small channels and wide ribs can preserve the membrane from drying, and small rib geometries prevent severe mass transport limitations [2]. Hence, a narrow channel combined with wide ribs is proposed for the inlet region of the cell (where membrane drying is likely due to locally high stoichiometries of unsuaturated reactants), while a smaller rib together with a wide channel seems appropriate for the outlet region (where the depleted oxidant causes reactant starvation).

Experimental

Experiments were carried out with a specialized test cell for the measurement of the local current distribution at the single cell level (see Fig.1). It features a 10-fold segmented current collector, where each segment is connected to a Hall-sensor for measuring its respective current (Fig.1a). The flow field plate has 20 straight channels of a length of 400 mm (Fig.1b).

Three different channel/rib geometries were investigated (see Figure 2). A constant narrow channel (geometry NC) with a rib ratio (the percentage of cell area covered

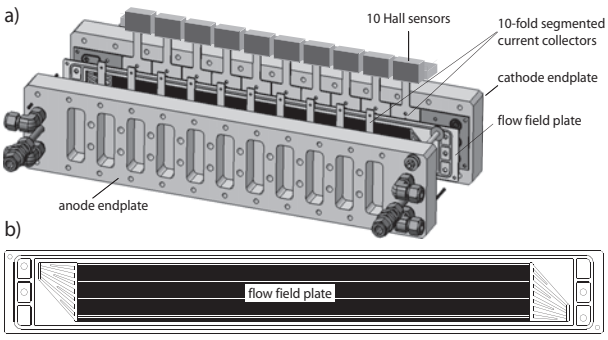

Figure 1. *a) Measurement cell for investigating the along-the-channel current distribution; b) Drawing of the straight channel flowfield plate (20 channels); c) Detail of the adaptive channel geometry used.*

by ribs) of 0.8, a constant wide channel (geometry WC) with a rib ratio of 0.2 and the adapted geometry (geometry AO) starting with a channel width of 0.5 mm and a rib width of 2.0 mm (rib ratio 0.8) and expanding towards the outlet to a channel width of 2.0 mm and a rib with of 0.5 mm (rib ratio 0.2).
Cells were operated on an in-house built test bench using hydrogen/air at a relative humidity of 40% (both gases), gas pressures of 2.0 bar(a) and a cell temperature of 70°C. Local current distributions along the channel were recorded during operation.

Results and Discussion

Polarization curves obtained with the 3 channel

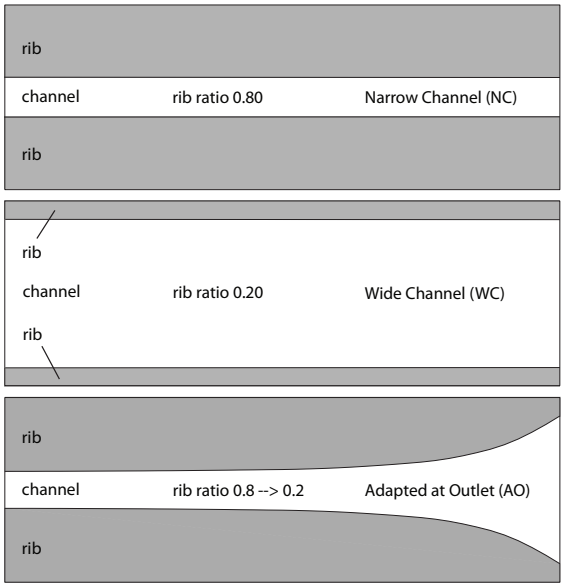

Figure 2. *Different channel geometries; top: constant narrow channel (NC, rib ratio 0.8); middle: constant wide channel (WC, rib ratio 0.2); bottom: adapted geometry with expansion at outlet (AO, rib ratio 0.8 → 0.2).*

geometries *NC*, *WC* and *AO* are shown in Figure 3a). It is seen that the *WC* geometry (constant rib ratio of 0.2) shows a clearly inferior performance as compared to the other two variations. The reason for this is a significantly higher membrane resistance measured (no data provided), owing to the wide channel. When comparing the *NC* (constant rib ratio of 0.8) and *AO* geometries, differences are observed in the mass transport regime of the polarization curve. An explanation for the better performance of the *AO* geometry is the effect of the rib width reduction in the outlet region, reducing mass transport losses in the cell domain with low oxygen partial pressures.

Figure 3b furthermore shows the local current distributions from inlet (z = 0 mm) to outlet (z = 400 mm), measured for the load point 0.5 A/cm^2 and reactant stoichiometries of $\lambda_{an/cath}$ = 1.4. It is seen that losses connected to membrane drying (low currents in the inlet region) are most severe in the case of the wide channel design *WC.* At the same time, this geometry exhibits higher currents in the outlet region, owing to the lower mass transport losses there due to the small rib size. The *AO* geometry shows the most homogeneous current

distribution: the currents in the inlet region are comparable to those of the *NC* design, which can be attributed to the small channel at this position. The expansion at the channel outlet, however, is responsible for a higher current production there, compared to *NC*. This positive effect seems to be strongest for high reactant consumption, or when the oxygen content in the gas is particularly low.

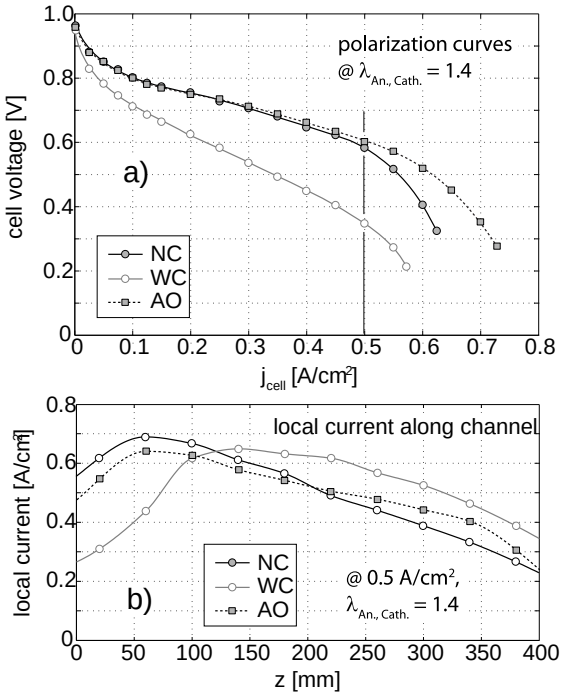

Figure 3. *a) Polarization curves at $\lambda_{an/cath}$ = 1.4 for the channel geometries NC, WC and AO; b) Local current distributions along the channel for these geometries at 0.4 A/cm^2.*

Therefore the stoichiometry dependence of the three geometries was investigated. Figure 4 shows in a) the cell performance at a load of 0.4 A/cm^2 for the variation of the reactant stoichiometry (both gases), indicating that the improvement of performance of *AO* vs. *NC* is indeed highest with low reactant supply. Again, the *WC* geometry shows the weakest performance due to the high membrane resistance. Figure 4b) compares the local current distribution along the flow channel for the case of the lowest point of stoichiometry at $\lambda_{an/cath}$ = 1.1. It is seen that for the *NC* design the low currents in the outlet region go along with a high current density at the inlet. The situation at the inlet is inversed for the WC design. Again, the geometry with the most homogeneous current distribution (*AO*) shows a higher cell performance.

Conclusions

The development and experimental testing of an adapted channel geometry has revealed that tailoring the design of the flow channel to the respective operating conditions is of advantage for homogenizing the along-the-channel current distribution, and therewith minimizing the losses connected to the respective local limitations in PEFC. The results indicate that the processes on the sub-mm scale of channels and ribs have been understood correctly and are important for the current distribution on the superordinate scale of the single cell level. In detail, it is shown that an expansion at the channel outlet reduces mass transport limitations, while a narrow channel at the inlet prevents membrane drying.

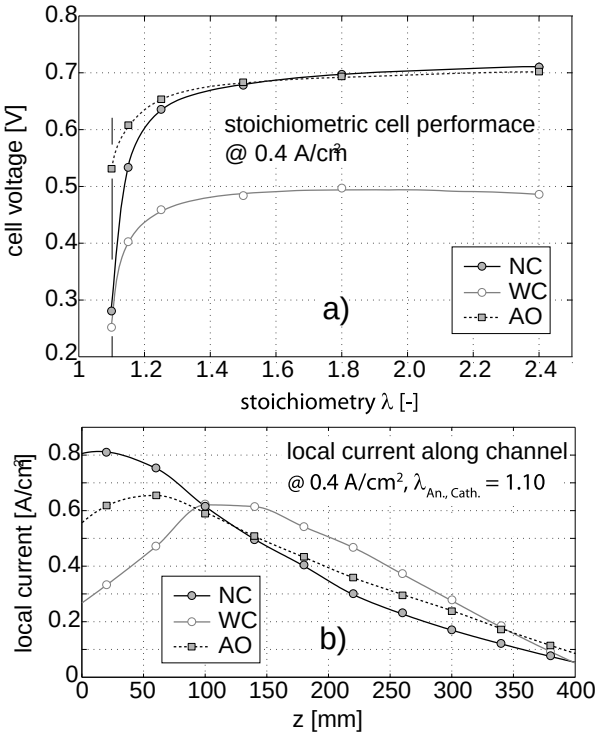

Figure 4. *a) Stoichiometric cell characteristics for NC, WC and AO at 0.4 A/cm^2; b) Local current distributions at $\lambda_{an/cath}$ = 1.1.*

References

[1] M. Reum, S.A. Freunberger, A. Wokaun, F. N. Büchi, J. Electrochem. Soc., in press (2009).

[2] M. Reum, PhD Thesis #17979, ETH Zürich (2008).

[3] J. Scholta, G. Escher, W. Zhang, L. Küppers, L. Jörissen, W. Lehnert, J. Power Sources, **155**, 66 (2006).

The local impedance response of low humidity polymer electrolyte fuel cells

I.A. Schneider, M.H. Bayer, A. Wokaun, G.G. Scherer

phone: +41 56 310 2795, e-mail: ingo.schneider@psi.ch

The Polymer Electrolyte Fuel Cell (PEFC) is a complex macroscopic electrochemical reactor. In a technical PEFC processes in three spatial dimensions determine the local cell performance and therefore, the impedance response. However, to date, conclusions deduced from PEFC impedance response have focused one-sidedly on the identification of limiting processes within the MEA [1], whereas the effect of reactant depletion and water accumulation along the gas flow channels has widely been ignored. However, these processes become limiting at finite gas flow rates and determine the current/voltage characteristics of a PEFC. Hence, their contribution to PEFC impedance response must undoubtedly be taken into account [2]. Recently, we have shown, that the effect of oxygen depletion along the gas flow channels can tremendously affect the local impedance response of an air fed PEFC [3]. The results clearly demonstrate that the interpretation of air fed PEFC impedance spectra must be reconsidered. Both, mass transport by convection along the flow channels and mass transport by diffusion determine concentration polarization losses and, therefore, impedance response. Evidently, this fact put forward an additional challenge for the analysis of results. However, neglecting channel processes can lead to wrong conclusions and therefore, their identification and consideration is crucial for a meaningful interpretation of results [2]. Beyond reactant depletion, also water formation and its accumulation along the gas flow channels must be taken into account for the analysis of PEFC impedance spectra [4]. Under sub-saturated conditions proper hydration of the polymer electrolyte and, therefore, the cell performance hinges upon the formation of product water and its accumulation along the gas flow channels.

Local impedance spectroscopy/neutron radiography in a low humidity PEFC

This phenomenon is illustrated by the results shown in Figure 1 for a low humidity PEFC operated on hydrogen (r.h. 50%) and dry oxygen in co-flow mode. The simultaneous application of neutron radiography and local EIS [5] reveals that the local cell performance in the dry region (seg. 1-4 in Fig 1a-c) is governed by the improving local hydration state of the ionomer, as a result of water formation and its accumulation in flow direction.

In contrast, the local cell performance becomes virtually constant downstream to seg. 5, as the polymer electrolyte becomes almost fully hydrated in the flooded region (seg. 6-9). Note that the cell is operated on pure gases and, since there is no diluting nitrogen, the reactant concentration is constant in flooded regions, as a result of constant water partial pressure. Consequently, neither the water nor the reactant concentration changes with ac current during ac impedance measurements in flooded regions (seg. 6-9) and, therefore, the respective local impedance spectra (Figure 1d) exhibit a single capacitive loop, which must be attributed to fast electrode processes and double layer charging. Note that impedance spectra of fully humidified PEFCs operated on diluted hydrogen (N_2/H_2) and pure oxygen show similar characteristics as observed in case of H_2/air-PEFCs as a result of hydrogen depletion in nitrogen along the anode flow field [6].

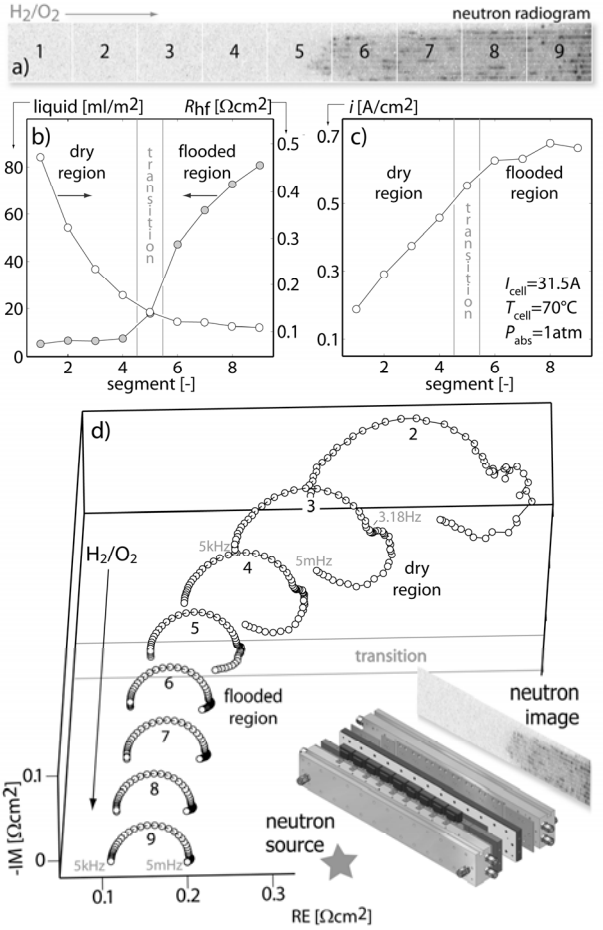

Figure 1: *Simultaneous local EIS/neutron radiography in a low humidity PEFC: a) neutron radiogram, b) local HFR vs. liquid water content of GDL, c) local current density and, d) local spectra (10pts/dec), $\lambda_{H2}=\lambda_{O2}=1.5$, dry O_2, $T_{dew\_H2}=55°C$.*

The situation is different in sub-saturated regions of the cell (seg. 1-4 in Figure 1), where the water and reactant concentration change with ac current at lower modulation frequencies. The appearance of the low frequency capacitive and the low frequency inductive loop in the sub-saturated region at modulation frequencies below f=3.18Hz is associated with this effect, as we have shown earlier [7]. Note that these low frequency features start to appear already in the local spectra of the flooded region, as parts of the flow field in the upper region become dry (Figure 1a).

Effect of ac current on water and reactant concentration in the gas flow channels

The effect of ac current on the water and reactant concentration along the gas flow channels is demonstrated in Figure 2. In the experiment, the ac polarization voltage η_{up} and the high frequency resistance R_{hf} of the outlet segment of the linear cell (seg. 9) were recorded under low humidity conditions

during a frequency sweep in the upstream segments (seg. 1-8). Note that in this experiment no liquid water could be formed in the cell. The results show (Figure 2a,b) that gas concentration oscillations build up along the flow channels at frequencies below $f \approx 3$Hz. The ac polarization voltage η_{up} caused in the outlet segment is essentially the result of a sinusoidal changing ionic resistance ΔR_{hf}, due to hydration/dehydration of the polymer electrolyte with ac current (Figure 2b). Calculation of the complex gain $1/(1-K)$ [4] reveals (Figure 2c) that the formation of the capacitive and the inductive loop at frequencies below $f=3.18$Hz is associated with this process and, therefore, primarily related to the hydration/dehydration of the polymer electrolyte. In this context, the small deviation between $i_{dc}\Delta R_{hf}/\eta_{mod}$ and η_{up}/η_{mod} (Figure 2b) is probably related to the contribution of other processes that depend on the dynamics of membrane hydration (Figure 2a) e.g., proton transport in the catalyst layer. In addition, changing concentration polarization must be taken into account here [2,3,8]. Note that η_{up} becomes zero for fully humidified operation.

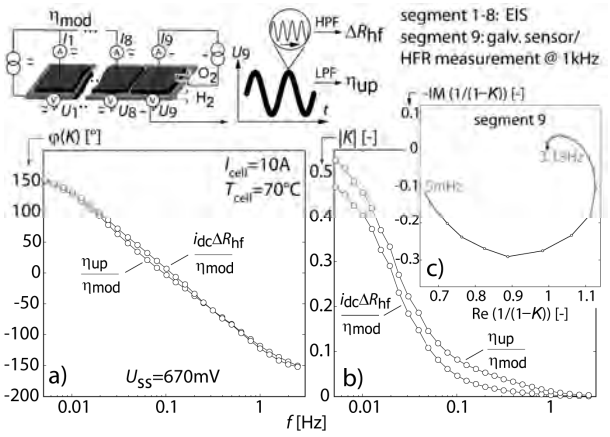

Figure 2: *a, b) Characteristic ac voltage response of seg. 9 $K=\eta_{up}/\eta_{mod}$ vs. characteristic ac response of the ohmic voltage drop $i_{dc}\Delta R/\eta_{mod}$ and, c) complex gain 1/1-K (seg. 9). V_{H2}=990ml/min, V_{O2}=330ml/min, dry O_2, T_{dew_H2}=40°C.*

Effect of water accumulation along the flow field on the local impedance response and i/E characteristic

The effect of the ac current in upstream parts of the cell on the local impedance response of the outlet segment is shown in Figure 3a. In case A, the ac polarization voltage was applied uniformly over the cell area, whereas the upstream segments were operated at the steady state voltage U_{ss} in case B. The build up of water and reactant concentration oscillations in the upstream segments in case A enlarges both, the low frequency capacitive and the low frequency inductive loop (Figure 3a), and thereby effectively lowers the local polarization resistance $Z(f \rightarrow 0\text{Hz})$. The smaller polarization resistance in case A is essentially the result of changing water production in the upstream segments and its effect on the hydration of the polymer electrolyte in the outlet segment. This manifests in a smaller slope of the local current voltage curve at the steady state voltage U_{ss} in case A (Figure 3b,c).

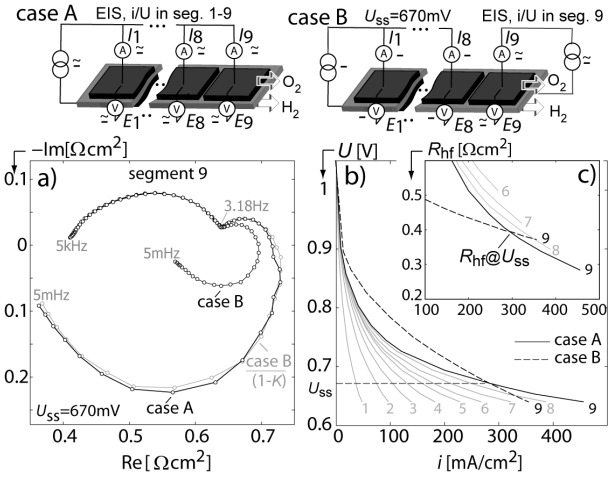

Figure 3: *Effect of water accumulation/reactant depletion in the upstream seg.s 1-8 on (a) local impedance response, (b) local i/u curve and, (c) local i/r_{hf} curve of the outlet segment 9. conditions as stated in Figure 2.*

Conclusions

The results show that the process of water formation and its accumulation along the flow fields governs PEFC impedance response under sub-saturated conditions. In this context, the contribution of the polymer electrolyte to PEFC impedance response is complex. The high frequency resistance (Figure 1b) is characteristic for fast proton transport, whereas the formation of the capacitive and inductive loop at low frequencies (Figure 1d) is associated with the slow hydration/dehydration of the polymer electrolyte [2,4,7]. Proton transport is a local property, yet the hydration/dehydration of the ionomer relies on both, local water formation/depletion and water accumulation/depletion along the flow channels in upstream regions of the cell and both processes determine PEFC impedance response. The results show that the existing one dimensional continuum mechanistic or equivalent circuit based analysis of PEFC impedance spectra [1] is not sufficient to describe the impedance response of low humidity PEFCs, unless special care is taken to exclude inhomogeneities in distinct dimensions [2]. In general 2D EIS models [8] are required to account for the effect of ac current on water and reactant concentration along the flow fields in low humidity PEFCs.

References

[1] P.M. Gomadam, J.W. Weidner, Int. J. of Energy Res. **29**, 1133 (2005).

[2] I.A. Schneider, G.G. Scherer in “Handbook of Fuel Cells “, Vol. 5/6, W. Vielstich, H.A. Gasteiger, H. Yokokawa, Editors, John Wiley & Sons, New York (2009).

[3] I.A. Schneider, D. Kramer, A. Wokaun, G.G. Scherer, J. Electrochem. Soc. **154**, B770 (2007).

[4] I.A. Schneider, M.H. Bayer, P. Boillat, G.G. Scherer, ECS Transactions **11**, 461 (2007).

[5] I.A. Schneider, D. Kramer, A. Wokaun, G.G. Scherer, Electrochem. Comm. **7**, 1393 (2005).

[6] I.A. Schneider, A. Wokaun, G.G. Scherer, unpub. results.

[7] I.A. Schneider, M.H. Bayer, A. Wokaun, G.G. Scherer, J. Electrochem. Soc. **155**, B783 (2008).

[8] M.H. Bayer, A. Wokaun, G.G. Scherer, I.A. Schneider, PSI Electrochemistry Laboratory - Annual Report 2008, ISSN 1661-5379 (2009).

Comparison of miniaturized PEFCs with and without gas diffusion layers

B.C. Seyfang, T. Lippert, A. Wokaun, G.G. Scherer

phone: +41 56 310 2092, e-mail: bernhard.seyfang@psi.ch

Miniaturized polymer electrolyte fuel cell (PEFC) systems are an interesting alternative to batteries to be applied as main energy source in hand-held devices. Miniaturization of PEFCS is often related to a reduction of particular parts. Gas diffusion layers (GDLs) are possible components to be removed, while other particular parts have to take over the various functions of the GDLs. We have developed a PEFC, whose micro-patterned glassy carbon flow fields surround only a catalyst coated membrane (CCM), which can deliver power densities in the range of 400 mW/cm^2 [1]. Despite this relatively high value, it is necessary to assess concept-related limitations by comparison of cells operateing with and without GDLs.

Experimental

The miniaturized PEFC is assembled by sandwiching a CCM between two micro flow fields with 65 parallel channels. When GDLs are utilized, ETEK 1400W is clamped between flow fields and the CCM and surrounded by a 200 µm thick Teflon sealing. A Nafion 212 membrane with catalyst loadings of 0.4 mg/cm^2 (cathode) and 0.15 mg/cm^2 (anode) was employed. The active area is 1 cm^2. The flow fields are surrounded by stainless steel end plates, in which the functions of electrical contact, gas supply to the micro-structures, temperature control and mechanical compaction are combined. Current voltage curves and electrochemical impedance spectra (EIS) were recorded at stoichiometries of 3.5 for both, hydrogen and oxygen, to ensure constant water removal from the flow fields with 65 parallel channels, at a cell temperature of 50°C. Both gases were humidified to a relative humidity of 80%. EIS were recorded at a DC current density of 0.5 A/cm^2 in pseudo-galvanostatic mode (AC voltage amplitude 10 mV).

Results

The current-voltage curves for the three cell configurations are displayed in Figure 1. Without GDL,

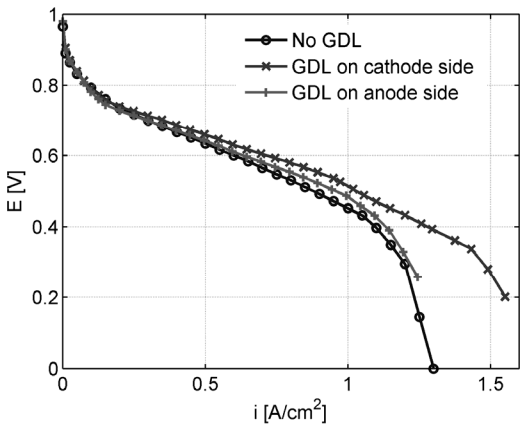

Figure 1.*.Current-voltage curves of a miniaturized PEFC recorded (i) without gas diffusion layers, (ii) with a GDL on either the cathode side or the anode side.*

we could identify the formation of a water layer on the cathode catalyst layer as the reason for a mass transport limitation [2, 3], resulting in a limiting current density i_{lim}. In our example i_{lim} reaches a value of 1.3 A/cm^2. In case of a cathodic GDL, this effect is not visible anymore. The hydrophobic GDL assures a sufficient transport of product water away from the catalyst layer.

Additionally, it is obvious that implementation of a GDL on the cathode side results in enhanced performance of the cell. Losses caused by foregoing the GDL are compensated. In case of a GDL being included on the anode side, the improvement of the performance is limited.

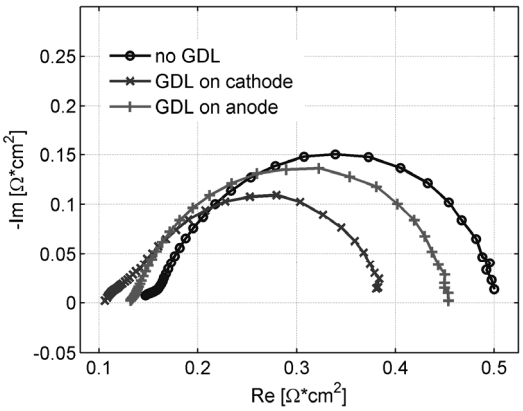

Figure 2. *Electrochemical Impedance Spectra of a miniaturized PEFC, recorded (i) without gas diffusion layers,(ii) with a GDL either on the cathode side or on the anode side.*

Electrochemical impedance spectra, recorded at a current density of 0.5 A/cm^2 are depicted in Figure 2. The shift of the high frequency intercept towards lower real part values shows clearly the reduced ohmic loss. In case of a GDL being implemented on the cathode side this reduction is more pronounced. Reduction of the average travel path for an electron in the thin catalyst layer seems to be the obvious reason here. This does not hold for the anode catalyst layer that is about a factor of two thinner than the cathode catalyst layer. In this case, the implementation of a GDL should even have a higher beneficial effect to the ohmic loss. However, the higher exchange current density for the hydrogen oxidation reaction might result in an inhomogeneous utilisation of anode catalyst particles, i.e. the reaction may take place on particles close to the ribs than in the centre of a micro-channel.

References

[1] B.C. Seyfang, M. Kuhnke, T. Lippert, G.G. Scherer, A. Wokaun, Electrochem. Commun. **9**, 1958-1962 (2007).

[2] B. C. Seyfang, P. Boillat, T. Lippert, G. G. Scherer, A. Wokaun, PSI Electrochemistry Laboratory - Annual Report 2007, 19, ISSN 1661-5379 (2008).

[3] B.C. Seyfang, P. Boillat, F. Simmen, T. Lippert, G.G. Scherer, A Wokaun, to be submitted (2009).

Liquid water constraints in miniaturized PEFC without gas diffusion layers

B.C. Seyfang, B.Boillat, T. Lippert, A. Wokaun, G.G. Scherer

phone: +41 56 310 2092, e-mail: bernhard.seyfang@psi.ch

Micro fuel cells are proposed as possible alternatives to Lithium Ion batteries as energy source in hand-held devices, such as laptops and cell phones. At PSI, a simplified, miniaturized polymer electrolyte fuel cell was developed, whose micro-patterned glassy carbon flow fields surround only a catalyst coated membrane (CCM) [1]. Foregoing the gas diffusion layers results in limitations, which are not understood very well up to now, but seem directly correlated to liquid water constraints. Neutron radiography is the method of choice to detect liquid water in operating fuel cells [2], recent improvements in resolution make it now applicable even to miniaturized PEFCs [3].

Experimental

The micro PEFC is assembled by sandwiching a CCM between two micro flow fields. A Nafion 112 membrane with catalyst loadings of 0.4 mg/cm^2 (cathode) and 0.15 mg/cm^2 (anode) was employed. For these experiments a meander with merging channels, whose number is reduced along the flow field from eleven to three channels, was applied. The flow fields are surrounded by gold-coated aluminum end plates, in which the functions of electrical contact, gas supply to the micro-structures, temperature control, and mechanical compaction are combined.

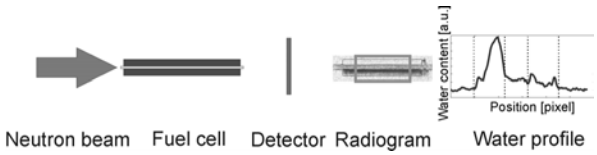

Figure 1. *Measurement principle for in-plane neutron radiography on a GDL-less micro PEFC. The orange rectangle represents area that is analyzed to obtain a water profile.*

We carried out *in plane* neutron radiography, i.e. in parallel to the membrane (Figure 1). Radiograms were referenced with a radiogram recorded at open current voltage (OCV) under dry conditions [2]. The integral liquid water content is obtained by evaluation of the grayscale profile of a referenced radiogram.

Results

While operating the micro PEFC, we could find an optimum operation point for a cell temperature of 50°C and gases humidified to 80% R.H. [1]. This temperature seems to be relatively low in comparison to technical fuel cells, where the optimum operation temperature lies usually in the range of 70-90°C. Data shown in Figure 2 give a reason for this performance.

When the fuel cell is operated at 50°C, no substantial difference in water profiles is observed for different humidification. The fact that the fuel cell reaction is the main source for water at this temperature explains this minimum influence of the R.H. of the feed gases. Only when the anode feed gas is not humidified at all, significant losses occur.

Increasing the fuel cell temperature to 70°C at 80% R.H. results in a reduced cell voltage (558 mV) and in a reduced amount of liquid water in the cathode and the anode channels (Figure 2C). The higher saturation vapour pressure of water in the feed gas results in a drying effect on the anode side. In contrast to a fuel cell with gas diffusion layers, in this micro fuel cell the catalyst area is directly exposed to the gas flows and, consequently, more susceptible towards drying effects.

A reduction of the gas humidification to 35% (Figure 2D) results in an even lower cell voltage (532 mV) and in an even lower water content on the anode side as well as in the membrane. An increased high frequency resistance indicates also the drying of the ionic phase.

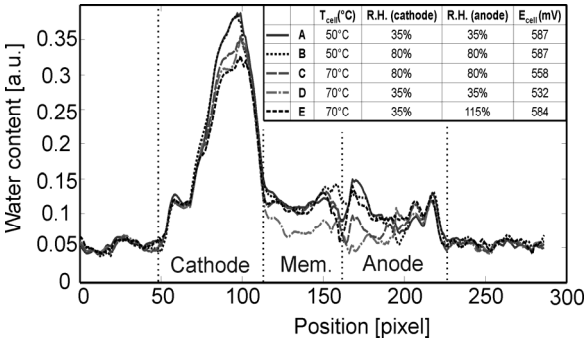

Figure 2. *Water profiles of a micro fuel cell containing a Nafion 112 membrane at different operation points.*

The effect of too dry anode conditions can be antagonized by super-saturation of the hydrogen stream to a relative humidity of 115% (Figure 2E). The water content for the anode channels shows values in the range as obtained for 50°C. The fact that the cell voltage increases again to a value of 584 mV for a current density of 0.6 A/cm^2 finally proves our hypothesis. An increase of the gas humidification above 35% on the cathode side does not bring any benefits, while further increase of the gas humidification above 115% on the anode side results in condensation already at the gas inlets of the cell and, as a consequence in non-stable operation of the micro polymer electrolyte fuel cell.

References

[1] B.C. Seyfang, M. Kuhnke, T. Lippert, G.G. Scherer, A. Wokaun, Electrochem. Commun. **9**, 1958-1962 (2007).

[2] D. Kramer, J. Zhang, R. Shimoi, E. Lehmann, A. Wokaun, K. Shinohara, G.G. Scherer, Electrochim. Acta **50**, 2603-2614 (2005).

[3] P. Boillat, D. Kramer, B.C. Seyfang, G. Frei, E. Lehmann, G.G. Scherer, A. Wokaun, Y. Ichikawa, Y. Tasaki, K. Shinohara, Electrochem. Commun. **10**, 546-550 (2008).

[4] B.C. Seyfang, P. Boillat, T. Lippert, G.G. Scherer, A. Wokaun, Electrochim. Acta, to be submitted.

PEFC parameter extraction from experimental data using multiparameter optimization algorithms

M. Zaglio, G. Schuler, A. Wokaun, J. Mantzaras, F.N. Büchi

phone: +41 56 310 5165, e-mail: maurizio.zaglio@psi.ch

Water management in the ionomer is mainly affecting the performance of a PEFC when the membrane is locally dry. The parameters influencing water transport in the membrane are: water diffusion coefficient, electro osmotic drag coefficient, ionic conductivity, and water sorption isotherm.
A 1+1-D model has been developed to simulate the behavior of a technical size PEFC [1]. When the reactants are dry, the water content of the membrane can be locally very low, and the simulations are not predicting well the cell behavior, due to uncertainties in the employed parameters at these particular operating conditions. The approach proposed herein is to perform a rigorous optimization of the parameters related to water management in the cell.

Experimental data

A linear PEFC with a 200 cm^2 active is used to collect experimental data. The cell is divided into ten segments, in each one the current density is measured. The measurement campaign focused on the collection of data at low hydrogen relative humidity.

Parameter expressions

A sigmoidal shape, Eq. (1), describes the water diffusion coefficient in the membrane as a function of water content λ (H_2O/SO^-_3):

$$D_w = A10^{-11}\left[1+\mathrm{tgh}\left(\frac{\lambda-2.5}{1.4}\right)\right]\left(\frac{\lambda}{25}\right)^{0.15}\exp\left(2416\left(\frac{1}{303}-\frac{1}{T}\right)\right) \quad (1)$$

where A is the parameter to fit.
The water drag coefficient χ is defined by two parameters, the first one (B) giving the initial slope of the curve and the second one (C) the maximum value that this parameter can assume, Eq. (2):

$$\chi = 0.3B\lambda \quad \text{if } \chi < C \text{ and } \lambda \le 14$$
$$\chi = C \quad \text{if } \chi \ge C \text{ and } \lambda \le 14$$
$$\chi = 2.55\exp\left[\frac{4000}{8.314}\left(\frac{1}{303}-\frac{1}{T}\right)\right] \quad \text{if } \lambda > 14 \quad (2)$$

The ionic conductivity K (Sm^{-1}) is assumed to be very low at λ<2, and to linearly increase at higher water content, Eq. (3):

$$K=0.125\,\lambda \quad \text{if } \lambda<2$$
$$K=D\lambda-2D+0.25 \quad \text{if } \lambda\ge 2 \quad (3)$$

The water sorption isotherm λ (H_2O/SO^-_3) is described by a more complicate polynomial equation as a function of water activity a_w, and the parameters to be fitted are two (E and F in Eq. (4)):

$$\lambda = \left(1+\frac{E}{a_w+F}\right)(2\,a_w^5 - 5.2a_w^4 + 11.05a_w^3 - 8.8a_w^2 + 3.9a_w + 0.0063) \quad (4)$$

Optimization procedure

The aim of the optimization algorithms is to minimize the difference between experimental current density and the model predictions at the same distance from the inlet and at the same operating conditions. Three different mathematical algorithms are used: “brute force”, which does not require any particular mathematical/coding skill, Newton’s method, efficient but possibly highly depending on the initial seeking point and an evolutionary algorithm [2], which always converges to the global best solution set.

Results

According to Eqs. (1) - (4), the curves describing the four parameters fitted to the experimental data are shown in Figure 1. The water diffusion coefficient assumes a value lower than the majority those reported in the literature. This can be due to the assumptions used in the model or to the appearance of surface phenomena at dry conditions not included in the model.
Using the optimized parameters the model is validated by local current density of a PEFC over a wide range of operating conditions.

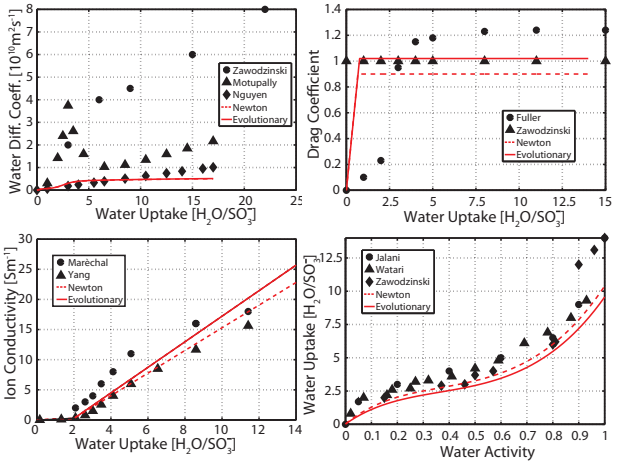

***Figure 1**. Comparison between experimental data and optimized parameters.*

References

[1] S.A. Freunberger, M. Santis, I.A. Schneider, A. Wokaun, F.N. Büchi, J. Electrochem. Soc., **153**, A396 (2006).

[2] M. Warth, PhD Thesis, No. 16357, ETH Zürich (2005).

BATTERIES & SUPERCAPACITORS

MATERIALS

Towards double layer capacitor and lithium-ion battery hybridization

D. Cericola, P. Ruch, R. Kötz, P. Novák, A. Wokaun

phone: +41 56 310 5172, e-mail: dario.cericola@psi.ch

Portable energy sources play an omnipresent role in everyday life. Their demand is expected to increase even further due to the development of hybrid and electric cars. Most applications require pulsed energy delivery, and rechargeable lithium-ion batteries (LiBs) are typically used. However, LiBs are not inherently high-power devices and high currents and power pulses have detrimental effects on their lifetime. In contrast, electrochemical double layer capacitors (EDLCs) are power devices suitable for pulsed applications. EDLCs and LiBs are complementary devices and could provide high energy and high power within a single device through hybridization. Hybrid devices were already presented in literature with different approaches. [1, 2, 3]. The hybridization of materials at the electrode level will allow obtaining an *internal parallel hybrid* (IPH).

Simulation of hybrid devices

The Ragone plot relates the energy available at a specific power demand. Calculations were performed for hybrid devices based on the external serial and the parallel connection of a 2.6 Ah Saft LiB and a 120 F Maxwell EDLC and for the two devices alone. The simulations were performed with the software Matlab – Simulink. A constant power pulse is applied to the fully charged system (at 4.2V or 6.9V in the case of the serial hybrid). The pulse is applied until the voltage drops below 3V (or 1.35V at the EDLC or 3V at the LiB in the case of the serial hybrid) and the required time determines the energy drawn. The effect of a pulsed discharge was also investigated. The device was discharged with pulses (each drawing 1% of the total energy in the device) with a duty cycle of 10%. Ragone plots for the different systems are compared in Figure 1. Serial hybrids exhibit a specific energy comparable with the EDLC and a specific power comparable with the LiB. Parallel hybrids take advantages from both EDLC and LiB, but the specific performance of the hybrid device falls always below that of the single component.

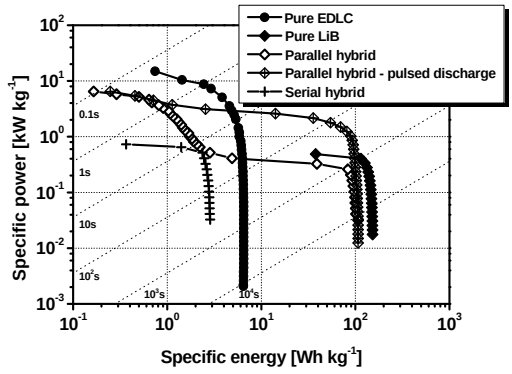

Figure 1. *Simulated Ragone plots of a commercial EDLC and LiB, respectively, as well as their hybrids*

For a pulsed application, however, the hybrid device performs even better than the battery in terms of power. This approach will allow designing systems with tuneable power-to-energy ratios.

Selection of materials

In an IPH, EDLC- and LiB-materials will experience the same conditions such as electrode potential and common electrolyte. For this reason, the knowledge of the behavior of the electrode materials in different electrolytes and at different potentials is required. The state-of-the-art LiB- and EDLC-materials were characterized. Two high surface area activated carbons (YP17 and BP15), three graphites (SLG3, SFG6 and SFG44) and lithium cobalt oxide ($LiCoO_2$) were investigated as electrode materials in electrolytes based on Et_4NBF_4 in acetonitrile or in propylene carbonate, and on $LiClO_4$ dissolved in ethylene carbonate / dimethyl carbonate 1:1 ($LiClO_4$ EC:DMC). The specific capacity (in mAh/g) at different electrode potentials was determined with galvanostatic charge/discharge cycling. The results suggest $LiClO_4$ EC:DMC as the most promising electrolyte for IPH. The capacities of the different electrode materials in this electrolyte are summarized in Figure 2. The activated carbons exhibit capacitive behaviour in the Li-based electrolyte. A suitable combination of EDLC and LiB materials requires the charge storage mechanism to be active in the same potential window. At this stage of the study this requirement is fulfilled for positive electrode with YP17 and $LiCoO_2$.

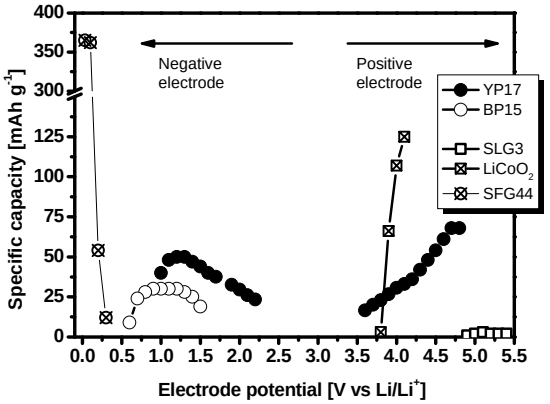

Figure 2. *Capacity (with a coulombic efficiency higher than 95%) versus electrode potential for the different electrode materials characterized in $LiClO_4$ EC: DMC.*

Acknowledgments

The Swiss National Science Foundation (SNF) is gratefully acknowledged for financial support. Special thanks to F. La Mantia, W. Maerkle, P. Maire, S.H. Ng, F. Rosciano, and W. Scheifele for the fruitful discussions.

References

[1] W.G. Pell, B.E. Conway; J. Power Sources **136**, 334-345 (2005).

[2] A. Burke; J. Power Sources **91**, 37-50 (2000).

[3] R. Chandrasekaran, G. Sikha, B.N. Popov; J Appl. Electrochem **35**, 1005-1013 (2005).

Carbon nanotube films as free-standing anodes for Li-ion batteries

S.Y. Chew[1], S.H. Ng, F. Krumeich[2], J.Z. Wang[1], H.K. Liu[1], P. Novák

phone: +41 56 310 2457, e-mail: petr.novak@psi.ch

In spite of the success in the commercial marketplace, there is currently an enormous research aimed at developing more advanced Li-ion battery technology for hybrid electric vehicles and clean energy storage fields. In particular, the search for alternative anode materials superior to graphite in terms of specific power has led to the development of various nanomaterials [1]. Amongst, carbon nanotubes (CNTs) were considered as a viable option due to their intrinsic ability to accept or donate electrons [2].

Industry enthusiasts believe that CNTs will radically improve the performance of batteries, because of their high surface-to-volume ratio and the relatively short diffusion length in the nanosized diameter tubes [3-4]. The lithium storage capacities of CNTs, in particular the single-wall CNTs (SWCNTs), have been determined experimentally to be significantly higher than that of the intercalated graphite (>1000 mAh g^{-1}) [5].

Normally, an electrode preparation technique based on mixing the CNT powders with a polymeric binder is applied [3,5]. But this technique reduces the effective surface area of the active material and limits the working temperature range due to the thermal stability of the binder. Here, a simple filtration technique is introduced to prepare free-standing CNT films, which are applied directly as electrodes in test cells.

Free-standing CNT films are attractive for basic electrochemical characterization due to their ease of handling, favorable mechanical properties, and most importantly absence of the binder. In this study, we compare the properties of SWCNTs, double-wall carbon nanotubes (DWCNTs), and multi-wall carbon nanotubes (MWCNTs), all as free-standing films. When used as the anode, the investigated films possess both the functions of charge storage and of a current collector.

Experimental

A vacuum filtration method was adopted and modified [4] for the preparation of free-standing CNT films. All CNT powders were used as-received. In a typical procedure, 30 mg of CNTs and 10 wt. % of carbon black were dispersed into 1 wt % of Triton X-100 in 60 mL of distilled water. This suspension was ultrasonically agitated. The as-prepared suspension was filtered through a porous PVDF membrane; CNTs were then trapped on the membrane surface, forming an entangled CNT mat. The CNT mat was then washed with 200 mL of distilled water and 100 mL of methanol. Subsequently, the entangled CNT mat was dried overnight at room temperature. The mat was then peeled off from the PVDF membrane and a free-standing CNT film was obtained.

The Brunauer–Emmett–Teller specific surface area (S_{BET}) and the mesopore volume of the powder samples were determined from a nitrogen adsorption/desorption isotherm at 77 K (Autosorb-1, Quantachrome Instruments). Prior to the adsorption process, the samples were out-gassed at 300 °C. The total pore volumes (V_{meso}) were determined with the Density Functional Theory (DFT)/Monte-Carlo method. Field-emission scanning electron microscopy (FE-SEM) images of the CNT film samples after cycling were obtained using the Zeiss Gemini 1530 instrument.

Electrodes from the obtained free-standing CNT films were punched out with a diameter of 11 mm each. They were then dried at 120 °C in a vacuum chamber overnight. Hermetically sealed test cells were assembled using free-standing CNT films as the working electrode and Li metal as both the counter and reference electrode. The electrodes were separated by a glass-fiber separator. The electrolyte was 1 M $LiPF_6$ in EC:DMC (1:1 by weight; Ferro GmbH).

The cells were galvanostatically charged and discharged in the potential window of 0.01 - 2.00 V vs. Li/Li^+ at a specific current of 25 mA g^{-1}. In order to promote complete charge-discharge, a potentiostatic step was included until the current was 10 % of the current used in the galvanostatic step. Cyclic voltammetric measurements were performed at a scanning rate of 0.05 mV s^{-1}.

Results

The electrochemical Li^+ storage properties of the three different types of CNT films were systematically studied (as shown in Figure 1). For the first cycle, both SWCNT and DWCNT films exhibit much higher specific charge compared to the MWCNT film. The MWCNT film exhibits a reversible charge of approximately 300 mAh g^{-1} with a stable cycling behavior. In contrast, the SWCNT and DWCNT films show strong fading upon cycling.

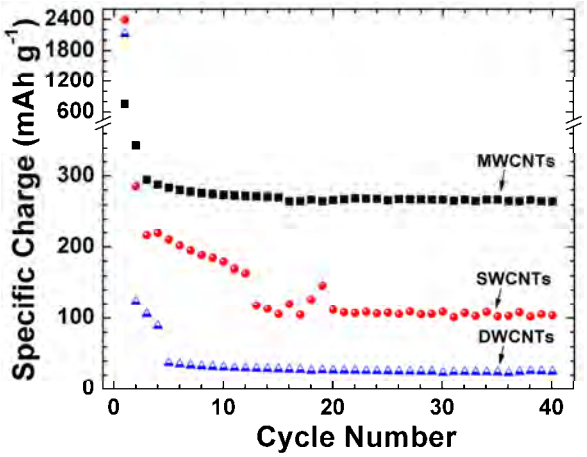

Figure 1. *Cycling behavior of SWCNT, DWCNT, and MWCNT electrodes.*

Basically, the charge (Li^+ insertion) process of the CNT films can be divided into two regions, negative and positive to ≈0.5 V vs. Li/Li^+ (see Figure 2). Negative to 0.5 V vs. Li/Li^+, Li^+ ions are intercalated into the graphitic-type layers. Positive to 0.5 V vs. Li/Li^+, the sharp peak at approximately 0.6 - 0.7 V vs. Li/Li^+ is attributed to the formation of the SEI layer [6]. An extra peak at approximately 1.2 V vs. Li/Li^+ is clearly observed

[1] University of Wollongong, Australia
[2] ETH Zürich

for the SWCNT film. This process is attributed to the reduction of surface species containing oxygen [5].

As for the discharge (Li^+ extraction) process, the MWCNT electrode exhibits a reversible peak at approximately 0.15 V vs. Li/Li^+, which is related to the de-intercalation of the Li^+ ions [7]. In contrast, SWCNT and DWCNT electrodes did not have any well defined peak, which clearly indicates that the reaction mechanism is entirely different to standard graphitic materials. Only a small, broad peak at approximately 1.2 V vs. Li/Li^+ is observed for both. This behavior is attributed to the quasi-reversible interaction between the Li^+ ions and surface-oxygenated functional groups [3]. Li^+ ions can also bind in the vicinity of H atoms in hydrogen-containing carbons enabling further reaction between the lithium and the electrolyte solution [5]. Possibly, the reversible charge obtained for the SWCNT and DWCNT films is related to such doping/de-doping processes.

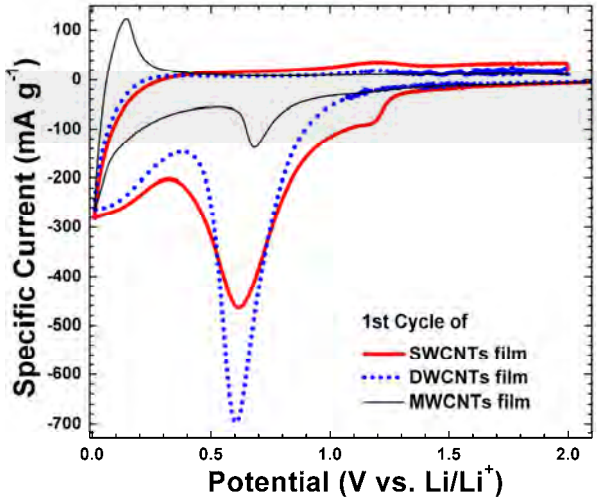

Figure 2. *Cyclic voltammograms at the 1st cycle for the free-standing CNT electrodes.*

Electrochemical reactions intrinsically occur at the interface between the solid electrode and the liquid electrolyte. The relevant data are summarized in Table 1, where we arbitrarily assign the irreversible charge (C_{irr}) in the potential window from 2.0 to 1.0 V vs. Li/Li^+ to the reduction of the surface functional groups, and from 1.0 to 0.3 V vs. Li/Li^+ to the SEI formation.

	Free-Standing Films		
	SWCNT	**DWCNT**	**MWCNT**
S_{BET} ($m^2\ g^{-1}$)	435	473	50
V_{meso} ($cm^3\ g^{-1}$)	0.75	0.93	0.13
C_{irr} by surface functional groups, 2.0 – 1.0 V vs. Li/Li^+ (mAh g^{-1})	600	147	29
C_{irr} by SEI formation, 1.0 – 0.3 V vs. Li/Li^+ (mAh g^{-1})	1091	1583	233
Total C_{irr}, 2.0 – 0.3 V vs. Li/Li^+ (mAh g^{-1})	1691	1730	262

Table 1. *Physico-chemical characteristics of the CNTs obtained by the BET and the DFT/Monte-Carlo method, and the irreversible charge (C_{irr}) of the free-standing CNTs electrodes during the initial reduction process.*

For carbonaceous materials, there is a fairly good relationship between the irreversible charge with respect to the S_{BET} [6] and the V_{meso} [3]. The higher the S_{BET} and the V_{meso}, the higher the total irreversible charge of the electrode. Our measurements are consistent with this relationship. Having a low S_{BET} value and low V_{meso} is beneficial for the electrochemical performance, as proved by the MWCNT electrode here.

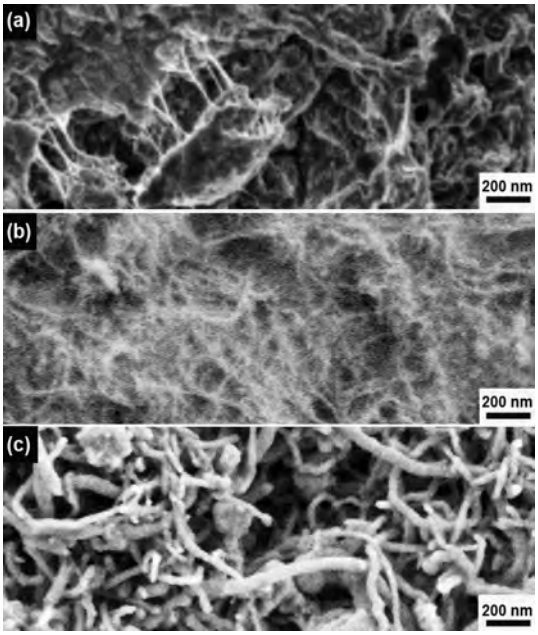

Figure 3. *SEM images of (a) a SWCNT, (b) a DWCNT, and (c) a MWCNT electrode, respectively, after 100 cycles.*

The morphology of the CNT electrodes after prolonged cycling was examined, as shown in Figure 3. For the MWCNT electrode, the shape and the mechanical integrity are still retained, a proof of its good mechanical stability. For the SWCNT and DWCNT electrodes, a thick and dense layer of the SEI together with other electrolyte decomposition products are observed not only on the surface of the CNTs but also in the spaces between the entangled CNTs.

Conclusion

Although the MWCNT film shows the best electrochemical performance, neither the irreversible nor the reversible specific charge are satisfactory for practical applications at the present state. Despite that, our results illustrate the feasibility of the free-standing MWCNT films as model electrodes for studies of electrochemical interface reactions, without the influence of binder and current collector.

References

[1] P.G. Bruce, B. Scrosati, J.-M. Tarascon, Angew. Chem. Int. Ed. **47**, 2930-2946 (2008).

[2] G.L.Che, B.B. Lakshmi, E.R. Fisher, C.R. Martin, Nature **393**, 346-349 (1998).

[3] E. Frackowiak, F. Béguin, Carbon **40**, 1775-1787 (2002).

[4] S.H. Ng, J.Z. Wang, Z.P. Guo, J. Chen, G.X. Wang, H.K. Liu, Electrochim. Acta **51**, 23-28 (2005).

[5] W. Lu, D.D.L. Chung, Carbon **39**, 493-496 (2001).

[6] M. Winter, P. Novák, A. Monnier, J. Electrochem. Soc. **145**, 428-436 (1998).

[7] M.E. Spahr, T. Palladino, H. Wilhelm, A. Würsig, D. Goers, H. Buqa, M. Holzapfel, P. Novák, J. Electrochem. Soc. **151**, 1383-1395 (2004).

$LiMn_2O_4$ thin films by flame spray deposition and *in situ* annealing method

S.Y. Chew[1], T.J. Patey, S.H. Ng, R. Büchel[2], F. Krumeich[2], J.Z. Wang[1], H.K. Liu[1], S.E. Pratsinis[2], P. Novák

phone: +41 56 310 2457, e-mail: petr.novak@psi.ch

A thin film electrode is a useful model system to study the electrochemical properties of $LiMn_2O_4$ without the influence of the binder and conductive carbon black [1]. $LiMn_2O_4$ thin film cathodes also have the potential to be applied in microbatteries for miniaturization of electronic devices. $LiMn_2O_4$ nanoparticles can be prepared by flame spray pyrolysis (FSP) [2]. There are also examples to prepare nanostructured sensing films by direct deposition of SnO_2 nanoparticles onto sensor substrate and *in situ* annealing [3], leading to a stable and highly sensitive gas sensor. The opportunity to produce $LiMn_2O_4$ thin film cathode is realized by considering these examples.

Experimental

Figure 1 displays the schematic diagram of the flame spray deposition (FSD) experimental setup. $LiMn_2O_4$ nanoparticles were directly deposited onto the current collector. Two different types of current collector were used, i.e. stainless steel (SS) and aluminum coated with primer (ACP). After deposition, the film was *in situ* annealed by xylene flame. The $LiMn_2O_4$ films were cut into 1.0 cm^2 squares and used as electrodes directly.

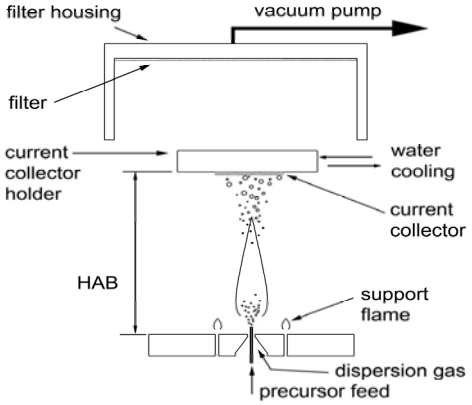

Figure 1. *Schematic of flame spray deposition of $LiMn_2O_4$ onto a water-cooled current collector.*

Results

The XRD pattern of the films after *in situ* annealing on SS and ACP are consistent with the known spinel phases, with a space group Fd3m (JCPDS 35-0782). Based on the Rietveld method, average crystal size of 10 nm was obtained for the nanoparticles on both current collectors after FSD. When *in situ* annealing was applied, no discernible crystal size change was observed for the ACP films. In contrast, the crystal size of the films on SS increased by 30 % (13 nm) after *in situ* annealing, indicating significant crystal growth.

When the SS films undergo annealing, most of the nanoparticles are rather densely packed together. This is quite different to the ACP films that remained unchanged by annealing. It should be noted that the film on ACP current collector is not stable after annealing.

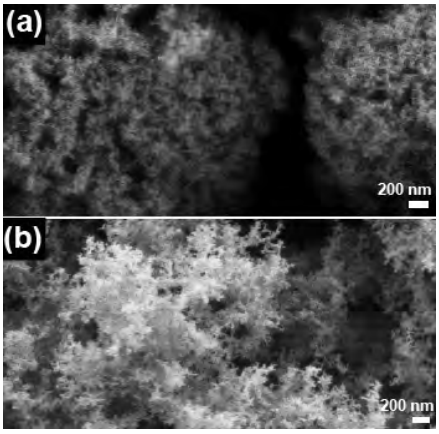

Figure 2. *The morphology of $LiMn_2O_4$ nanoparticles after in situ annealing onto the (a) SS and (b) ACP current collectors.*

Figure 3 shows the reversible charge of the thin film electrodes prepared with the *in situ* annealing upon cycling. Fading is observed after several cycles in all cases, but the decay for *in situ* annealed $LiMn_2O_4$ nanoparticles deposited on the SS current collector is much slower than those on the ACP current collector.

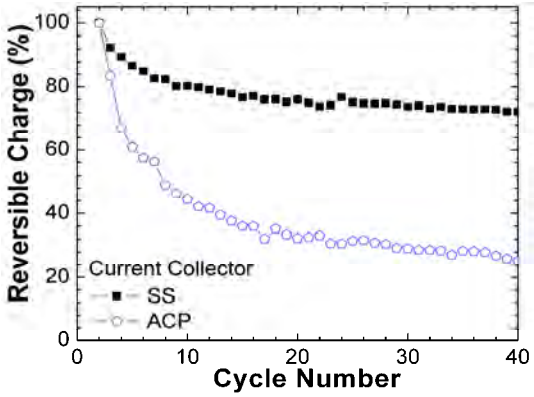

Figure 3. *Reversible charge as a function of cycle number from the galvanostatic experiments of the in situ annealed $LiMn_2O_4$ thin film electrodes on the SS and ACP current collectors.*

The studies indicate that $LiMn_2O_4$ thin films can be prepared by simple, fast and efficient FSD and *in situ* annealing method. This method has never been applied for the preparation of electrode materials. In particular, SS films with increased crystal size by annealing perform better electrochemically than ACP films.

References

[1] K.A. Striebel, A. Rougier, C.R. Horne, R.P. Reade, E.J. Cairns, J. Electrochem. Soc. **146**, 4339-4347 (1999).

[2] F.O. Ernst, H.K. Kammler, A. Roessler, S.E. Pratsinis, W.J. Stark, J. Ufheil, P. Novák, Mater. Chem. Phys. **101**, 372-378 (2007).

[3] A. Tricoli, M. Graf, F. Mayer, S. Kühne, A. Hierlemann, S.E. Pratsinis, Adv. Mater. **18**, 1969-1976 (2008).

[1] University of Wollongong, Australia
[2] ETH Zürich

Effects of electrode density on the electrochemical performance of graphite negative electrodes in Li-ion batteries

S.H. Ng, F. La Mantia, P. Novák

phone: +41 56 310 2457, e-mail: petr.novak@psi.ch

Graphitic carbons are currently the most often employed material for the negative electrode due to their low cost, excellent cyclability and reliability, and non-toxicity [1]. One of the key areas where improvement of graphite is of great importance is the reduction of the irreversible charge loss (ICL) measured during the first electrochemical Li^+ insertion. There are 3 types of ICL in graphite negative electrodes [2]: (i) charge loss related to the reduction of the surface groups between 3.0 and 0.8 V vs. Li/Li^+; (ii) charge loss due to solid electrolyte interphase (SEI) film formation between 0.8 and 0.2 V vs. Li/Li^+; and (iii) charge loss due to the irreversibilities in the insertion and extraction of lithium ions. Only a few reports [3,4] are on the changes in the ICL for graphite anodes when mechanical pressure (or compression) is applied. Here, ICL of highly crystalline synthetic graphite electrodes is explored as a function of electrode density.

Experimental

The graphite (SLX50, TIMCAL SA) negative electrodes were prepared by doctor-blading slurries of graphite active material (90 wt.%) and poly(vinylidene fluoride) binder (10 wt.%, SOLEF 1015, Solvay SA) in a N-methylpyrrolidinone (NMP) solvent onto a copper foil. The electrodes were vacuum dried at 120 °C overnight. After drying, electrode disks (1.3 cm^2) were punched for test cell assembly in an argon-filled glove box. Hermetically sealed laboratory test cells were used, where the working and counter (metallic lithium) electrodes were slightly pressed together against a glass fiber separator soaked with a standard battery electrolyte [1 M $LiPF_6$ in EC:DMC (1:1 by weight), Ferro Corp. USA]. Galvanostatic measurements were performed at specific currents of 10 mA g^{-1} (of graphite) in order to complete the SEI formation during the first electrochemical Li^+ insertion. When a potential of 5 mV vs. Li/Li^+ was reached, the discharge step was continued potentiostatically until the specific current dropped below 5 mA g^{-1}. The charge step was performed at a constant specific current of 10 mA g^{-1} until a cut-off potential of 1.5 V vs. Li/Li^+ was reached.

Results

The first cycle ICL of the graphite anode decreased with an increase in the apparent electrode density through compression (see Figure 1a and 1b). In addition, high mass loading also contributed to a decrease in the first cycle ICL of the graphite anode (see Figure 1c). The reduction of the ICL was attributed to a more efficient SEI formed on the carbon after compression. Furthermore, higher over-potential was observed for the compressed graphite anode due to higher electrode density, which led to higher apparent electrolyte resistance in the porous structure of the electrode [5]. In summary, we have shown here that electrode engineering on graphite negative electrodes is an important step towards optimization of the ICL during the first electrochemical Li^+ insertion in a Li-ion battery system.

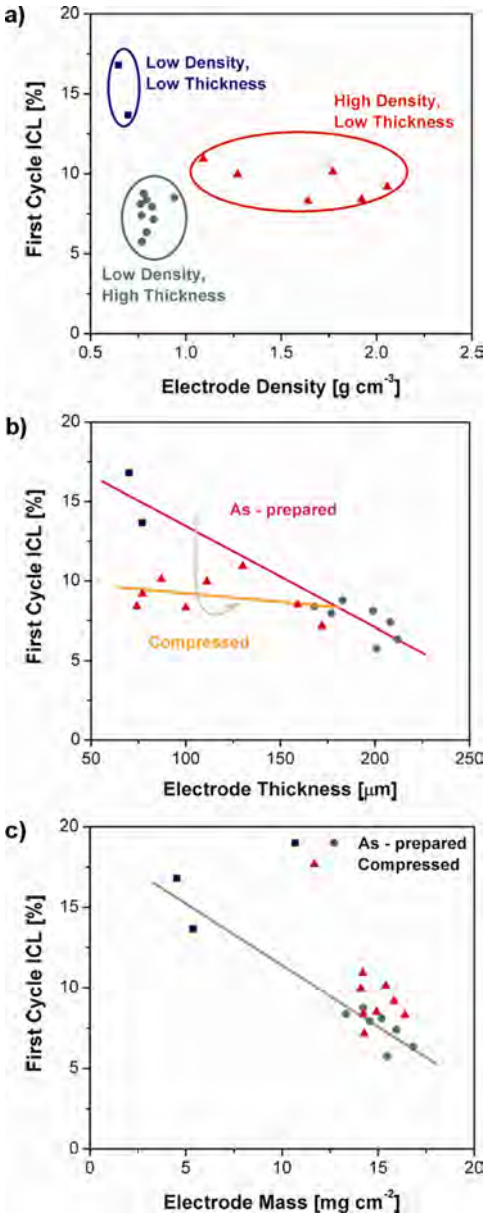

Figure 1. *The first cycle ICL of the SLX50 graphite anode as a function of the electrode's: (a) density, (b) thickness, and (c) mass loading.*

References

[1] M. Winter, J.O. Besenhard, M.E. Spahr, P. Novák, Adv. Mater. **10**, 725-763 (1998).

[2] F. Joho, P. Novák, O. Haas, A. Monnier, F. Fischer, Mol. Cryst. Liq. Cryst. **310**, 383-388 (1998).

[3] J. Shim, K.A. Striebel, J. Power Sources **130**, 247-253 (2004).

[4] K.A. Striebel, A. Sierra, J. Shim, C.W. Wang, A.M. Sastry, J. Power Sources **134**, 241-251 (2004).

[5] S.H. Ng, F. La Mantia, P. Novák, in preparation (2009).

Influence of the coating of the glassy carbon substrates on the properties of $Li_{1+x}Mn_2O_{4-\delta}$ films

F. Simmen, T. Lippert, P. Novák, M. Horisberger, M. Döbeli, M. Mallepell, A. Wokaun

phone: +41 56 310 4194, e-mail: franziska.simmen@psi.ch

$Li_{1+x}Mn_2O_{4-\delta}$ is an promising electrode material for lithium-ion batteries. It has lower toxicity, lower material cost, and a relative high energy density in the potential range of 3.5-4.4 V, making it a promising alternative electrode material to $LiCoO_2$. A disadvantage of the $Li_{1+x}Mn_2O_{4-\delta}$ material is the capacity decrease during cycling. A possible reason for lower performance of the aged batteries could be the formation of the solid electrolyte interphase (SEI) on the active material. To study the SEI formation it is necessary to use, e.g., thin films instead of composite material consisting of powder material and additives (such as binder and carbon black), to exclude the influence of the additives. Thin films can be prepared by different methods such as pulsed laser deposition (PLD) [1], radio frequency magnetron sputtering [1,2], electron beam evaporation [2,3], and electrostatic spray deposition (ESD) [4]. The pulsed laser deposition of the $Li_{1+x}Mn_2O_{4-\delta}$ films was done on different substrates such as silicon, stainless steel [5,6], platinum [7], and glassy carbon [6]. As reported [6], there is a weak adhesion of the thin films on pure glassy carbon. To overcome that problem and to improve the film properties different metallic coatings were used as an intermediate layer between glassy carbon and the pulsed laser deposited $Li_{1+x}Mn_2O_{4-\delta}$ thin films.

Experimental

$Li_{1+x}Mn_2O_{4-\delta}$ films were prepared by PLD (KrF Lambda Physik, 248 nm, 20 ns, 10 Hz, 4.0 – 4.3 Jcm^{-2}, 18000 pulses, d_{t-s} = 4 cm, p_{O2} = 0.2 mbar) on coated/uncoated glassy carbon substrates (T ~ 500 °C). The rod-like target was prepared by mixing $Li_{1.03}Mn_2O_4$ (99.7 % purity, Honeywell) with an excess of 2.5 Mol% Li_2O, pressing (4000 bar), and sintering in oxygen (10 h, 750 °C).

The basis substrate was glassy carbon (GC, SIGRADUR G, HTW, Thierhaupten, Germany) which was sputtered with an additional, around 10 nm thick metallic layer [Au, Pt, and combination of Au(10 nm)/Pt(10 nm)]. The technique was DC Magnetron Sputtering [TIPSI, 200 W (Au), 50 W (Pt), PK75 target, Argon, 0.003 mbar].

The thin films were cycled in the potential range of 3.5 - 4.4 V versus Li/Li^+ using Li foil (Aldrich) as anode. The used electrolyte was 1 M $LiClO_4$ in propylene carbonate (PC) (Ferro, USA, H_2O < 15 ppm). The electrode material was tested with cyclic voltammetry at 0.05 mV s^{-1} and galvanostatic charge/discharge experiments.

Results

The average composition of the ca. 300 nm thick films was $Li_{1.06}Mn_2O_{3.8}$. Compared to the nominal target composition of $Li_{1.08}Mn_2O_{4.03}$ the films showed a lithium deficiency of 1.9% and an oxygen deficiency of 5.7%. The lithium deficiency could be due to a noncongruent process during pulsed laser deposition caused by collision and scattering of the light lithium by heavier elements in the plasma or by the oxygen background gas molecules and/or by sputtering/backscattering of the volatile lithium from the growing film [8,9].

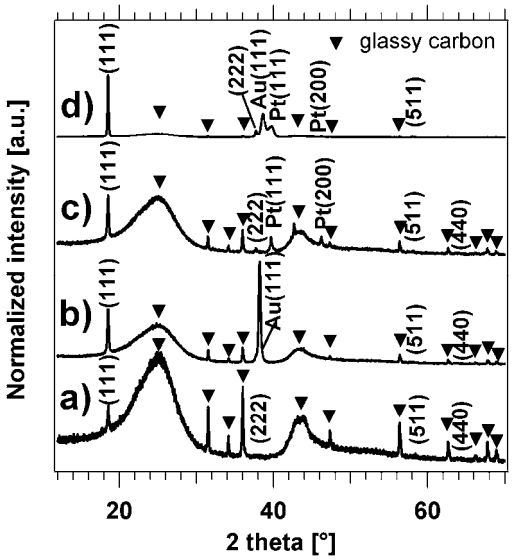

Figure 1. X-ray diffraction pattern of thin $Li_{1+x}Mn_2O_{4-\delta}$ films (a) on glassy carbon, (b) on Au coated glassy carbon, (c) on Pt coated glassy carbon, and (d) on Au/Pt coated glassy carbon substrates. The reflexes of glassy carbon are marked with ▼.

The crystallinity of the films increased with using additional metallic intermediate layer. The most intense (111) reflexes were observed for films deposited on Au/Pt/GC

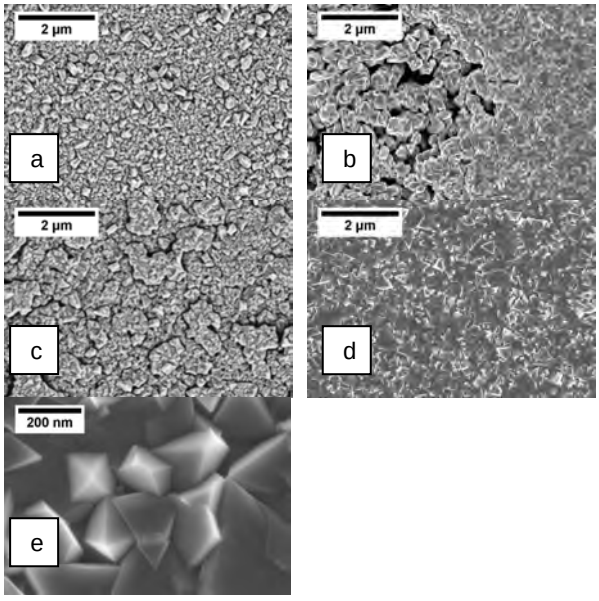

Figure 2. *SEM images of thin $Li_{1+x}Mn_2O_{4-\delta}$ films deposited (a) on glassy carbon, (b) on Au coated glassy carbon, (c) on Pt coated glassy carbon and (d,e) on Au/Pt coated glassy carbon substrates.*

(see Figure 1). No crystalline impurities were observed. The most regular surface morphology was observed for films on uncoated glassy carbon and on Au/Pt/GC (see

Figure 2). The films on Au/Pt/GC consist of octahedral and tetrahedral crystallites. The use of Au and Pt single intermediate layer resulted in a less homogenous surface morphology with parts of increased roughness and not closely packed regions. The nonuniform film formed on Au is a result of changes in the underlaying Au layer occurring upon heating in the PLD chamber. The films deposited on pure glassy carbon or Au-coated glassy carbon had the lowest adhesion.

During charging (oxidation) of the $Li_{1+x}Mn_2O_{4-\delta}$ thin films lithium is deinserted in a two step-process and MnO_2 is nominally formed. During discharging (reduction) the lithium is inserted in to the oxide electrode and finally the original spinel is reformed. For all different film-substrate combinations the typical two oxidation/reduction peak pairs were observed. These agreed well with the redox peak pairs of the standard composite material. The cyclic voltammogram of a film deposited on uncoated glassy carbon is shown in Figure 3.

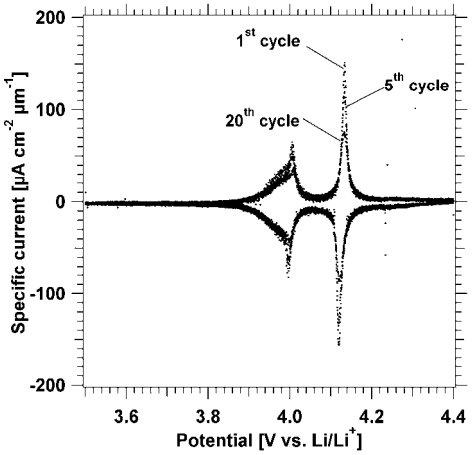

Figure 3. *Typical cyclic voltammogram in 1M $LiClO_4$/PC electrolyte at 0.05 mV s^{-1} of thin $Li_{1+x}Mn_2O_{4-\delta}$ films deposited on glassy carbon.*

The thin films were tested with respect to their cycleability with galvanostatic charge/discharge experiments. The highest specific charge was obtained for the $Li_{1+x}Mn_2O_{4-\delta}$ /Pt/GC combination and the lowest one for films deposited on Au coated glassy carbon substrates. The highest amount of irreversible capacity was measured for films deposited on Pt and Au/Pt coated glassy carbon substrates. The comparison of the relative charge capacities showed that, films deposited on Pt coated glassy carbon had the highest cycling stability (see Figure 4). The cycling stability was influenced through the film – substrate adhesion. The highest adhesion was observed for films on Pt coated glassy carbon. The film was still intact after the cycling. The films deposited on pure glassy carbon and on the Au and Au/Pt coated glassy carbon showed the lowest adhesion.
The decrease of specific charge could further be due to a possible SEI formation and/or aging of the oxide electrode itself.

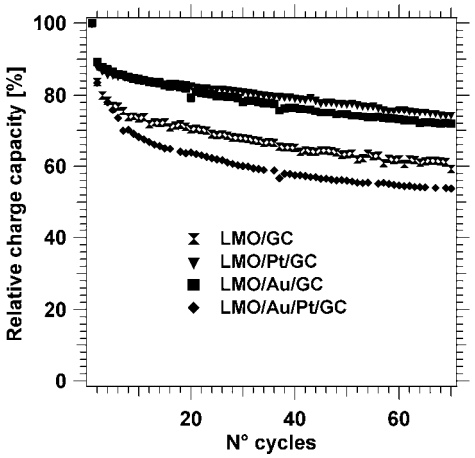

Figure 4. *Relative charge capacities of the films deposited on glassy carbon, on Au coated glassy carbon, on Pt coated glassy carbon, and on Au/Pt coated glassy carbon substrates.*

Conclusions

The use of different metallic intermediate layers (Pt, Au, Au/Pt) resulted in a variation of the final $Li_{1+x}Mn_2O_{4-\delta}$ film properties compared to the use of pure glassy carbon substrates. The additional metallic layer improved the crystallinity of the deposited spinel with a preferred (111) orientation, especially in the case of Au/Pt intermediate layer. Only the use of the Pt intermediate layer lead to a stronger adhesion of the films and better electrochemical performance.

References

[1] C.C. Chen, K.F. Chiu, K.M. Lin, H C. Lin, C.R. Yang, F M. Wang, Physica Scripta **T129,** 74-79 (2007).

[2] S.W. Jin, H.N.G. Wadley, J. Vacuum Sci. & Techn. A Vacuum, Surf. Films **26,** 114-122 (2008).

[3] V.K. Vani, O.M. Hussain, AIP Conf. Proc. **1004,** 58-62 (2008).

[4] K. Dokko, N. Anzue, M. Mohamedi, T. Itoh, I. Uchida, Electrochem. Commun. **6,** 384-388 (2004).

[5] F. Simmen, T. Lippert, P. Novák, M. Döbeli B. Neuenschwander, M. Mallepell, A. Wokaun, Appl. Phys. A Mater. Sci. & Proc. **93,** 711-716 (2008).

[6] F. Simmen, T. Lippert, P. Novák, B. Neuenschwander, M. Döbeli, M. Mallepell, A. Wokaun, Appl. Surf. Sci. In press.

[7] D. Singh, R. Houriet, R. Giovannini, H. Hofmann, V. Craciun, R. K. Singh, J. Power Sources **97-98,** 826-831 (2001).

8] T. Dumont, T. Lippert, M. Dobeli, H. Grimmer, J. Ufheil, P. Novák, A. Wursig, U. Vogt, A. Wokaun, Appl. Surf. Sci. **252,** 4902-4906 (2006).

[9] D. O'Mahony, J. Lunney, T. Dumont, S. Canulescu, T. Lippert, A. Wokaun, Appl. Surf. Sci. **254,** 811-815 (2007).

BATTERIES & SUPERCAPACITORS

DIAGNOSTICS

In situ X-ray diffraction study of the intercalation of PF_6^- anions in graphite.

J.-F. Colin, W. Maerkle, P. Novák

phone: +41 56 310 2410, e-mail: jean-francois.colin@psi.ch

Graphite is widely used as anodic material in commercial Li-ion batteries. But as metal oxides used as cathodic materials are poorly conductive, graphite is also often used as an additive in the cathodic part of the batteries, to increase their electronic performance. In the look for higher energy, interest for high-potential cathodic materials has increased. At these potentials, the reversible intercalation of PF_6^- anions into graphite in oxidatively stable electrolytes like ethyl methyl sulfone was reported [1]. This intercalation of PF_6^- anions could lead to structural changes or even amorphization of the graphite that could be detrimental to the performance of the electrode. We thus decided to investigate the influence of graphite morphology on this phenomenon by *in situ* synchrotron X-ray diffraction at the SLS (Swiss Light Source).

Experimental

Four types of graphite were investigated, that means TIMREX® SFG6 and SFG44 (TIMCAL) and their heat treated derivatives SFG6HT and SFG44HT. These graphites differ by particle size (d_{90} values: SFG6 - 6.5µm; SFG44 - 48.8µm) and cristallinity (the heat treated samples present better cristallinity) allowing us to study the influence of these two parameters. The investigation was carried in "coffee bag" cell configuration, using the sample changer developed in our group for the MS-beamline of the SLS [2]. The electrodes were constituted as follows: 90%wt studied graphite and 10%wt binder (SOLEF PVDF 1015, Solvay). The electrolyte used was 1M $LiPF_6$ in PC/DMC (Ferro, PC = propylene carbonate, DMC = dimethyl carbonate). Patterns were recorded using a 17.5 keV X-Ray beam corresponding to a 0.70834Å wavelength. The diffractograms were acquired for 2*20s, the time between two diffractograms is approximately 10min, leading to a good time resolution. The electrochemical cycling was carried following two different protocols. The first one consists in a cyclovoltammetry at 0.1mV.s^{-1} rate in the 3.0V-5.2V (vs. Li/Li^+) window. The second one is a galvanostatic cycling between 3.0V and 5.5V (vs. Li/Li^+) with a first cycle carried at C/5 rate and a second one at C/10.

Results

The changes in the graphite structure were followed by looking at the evolution of the 002 peak. Its position is indeed linked to the average distance between two graphene planes as formulated by the Bragg's law: $2\, d_{002} \sin\Theta_{002} = \lambda$, where d_{002} is the average interlayer distance and Θ_{002} is the position of the 002 peak. The intercalation should then be reflected by an increase of the interlayer distance leading to a shift of the 002 peak to a smaller angle. The formation of staged phases can also be checked by looking at the appearance of new peaks, the n index of the staging, representing the number of graphene layers between each PF_6^- layer is then calculated thanks to the following formula:

$$n = \frac{1}{\frac{(\sin\theta_{00n+1})}{(\sin\theta_{00n})} - 1}$$

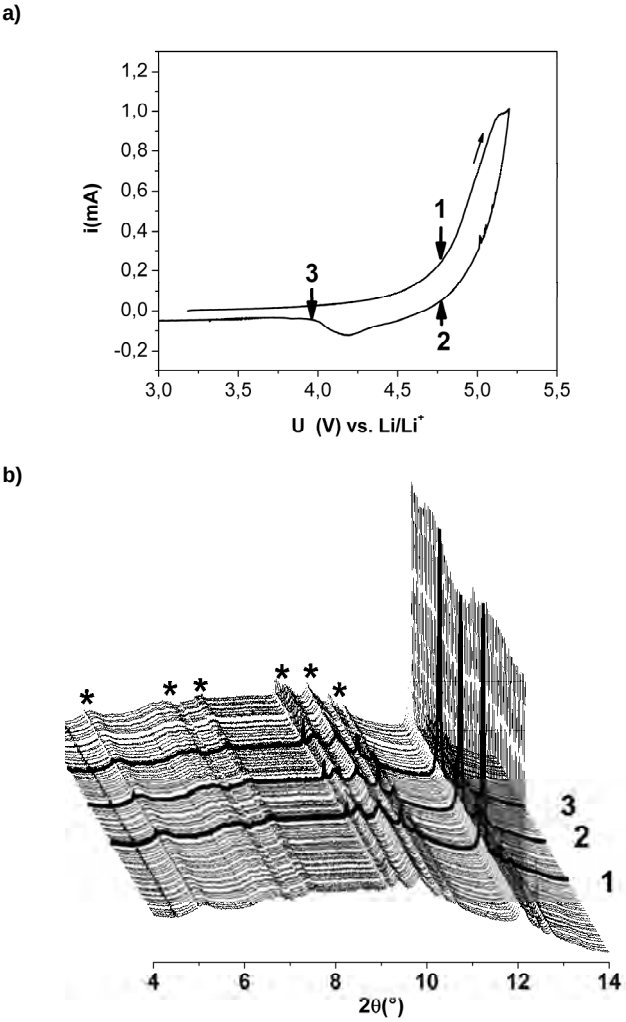

Figure 1. *a) Cyclovoltammogram of SFG6 in 1M $LiPF_6$ in PC/DMC. b) Evolution of the diffractogram of SFG6 during cycling. Asterisks indicate peaks coming from the cell.*

where 00n and 00n+1 are the new peaks appearing respectively at the left and at the right of the former 002 peak.

Figure 1 shows the evolution of the SFG6 diffractogram along the cyclovoltammetry; only small change in the intensity of the dominant 002 peak is observed. The intensity decreases slowly from **1** to **2**, when the potential is higher than 4.8V and then recovers when the potential reaches 4V again (**3**). The weak change in the intensity indicates that the intercalation of PF_6^- anions in SFG6 is a minor phenomenon. Unlike SFG6, SFG44 shows clear evolution along the cyclovoltammetry. As soon as the potential reaches 4.6V, a shift of the 002 peak towards smaller angles indicates intercalation of PF_6^-. This intercalation leads to the formation of a n=4 staged phase with further oxidation, as indicated by the appearance of two peaks at 11.3° and 14° (Fig.2, **2**). But as shown by the low intensity of these peaks, the crystallinity of these intercalated phases is poor; this could explain the weak reversibility of the phenomenon as observed down to 4V (Fig. 2, **3**). Comparing these

two graphites, it seems that bigger particles are more prone to intercalate PF_6^-. This could be explained by the possibility for the mechanical stress created during the beginning of intercalation to be released on the larger surface of bigger particles.

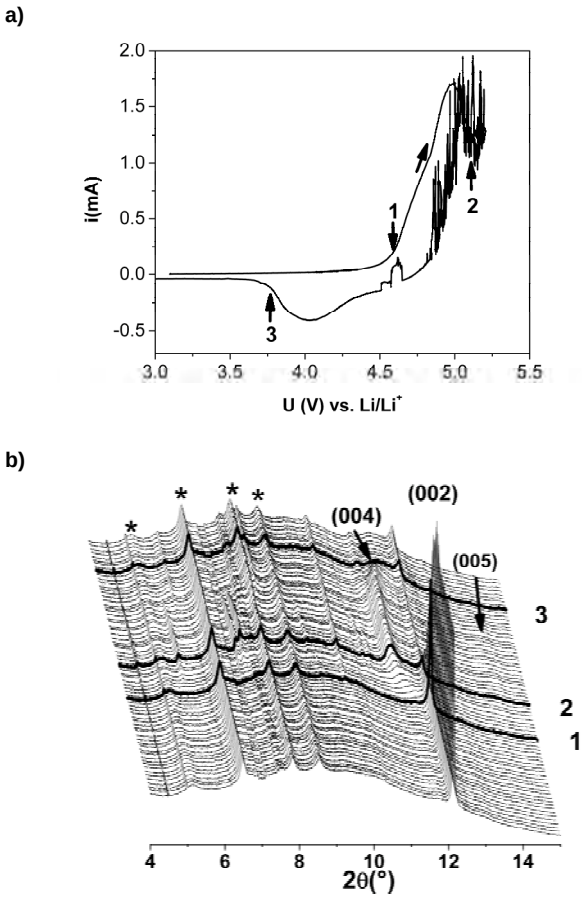

Figure 2. *a) Cyclovoltamogram of SFG44 in 1M $LiPF_6$ in PC/DMC. b) Evolution of the diffractogram of SFG44 during cycling. Asterisks indicate peaks coming from the cell.*

Figure 3 presents the evolution of the SFG44HT diffractogram during galvanostatic cycling. Here again intercalation occurs when the potential reaches 4.8V, leading to the formation of a n=4 staged phase. Like in the SFG44 the intercalation is only partly reversible (Fig. 3, **2**). But contrary to the intercalated phase obtained with SFG44, this phase possesses a good crystallinity, as indicated by the intensity of the 004 peak (11.3°). This shows that a better crystallinity of the starting phase is favorable to the intercalation. This is certainly related to a better path of diffusion in the bulk when the crystallinity is higher. Similar results were obtained with SFG6HT, although no intercalation was observed into SFG6, confirming thus the favorable character of intercalation in crystalline graphite.

Conclusions

This study has shown that the morphology of graphite is an important parameter regarding its stability as electrode additive at high potentials. Among the studied graphites, SFG6 presents the higher stability with almost no structural changes during cycling. Increasing the particle size (SFG44) or the crystallinity (SFG6HT, SFG44HT) of the graphite leads to irreversible intercalation of PF_6^- anions, which can be detrimental to the electronic behavior of the electrode (loss of contact between the oxide and graphite particles, lower conductivity).

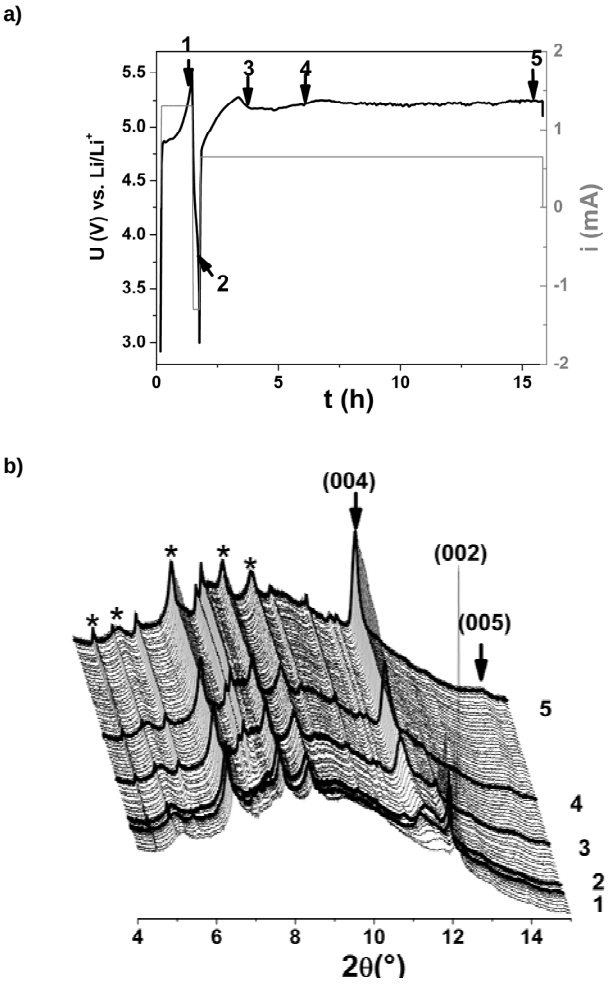

Figure 3. *a) Galvanostatic cycling of SFG44HT in 1M $LiPF_6$ in PC/DMC. b) Evolution of the diffractogram of SFG44HT during cycling. Asterisks indicate peaks coming from the cell.*

Acknowledgments

We are thankful to the MS beamline team at the SLS for their help during these experiments and TIMCAL SA for graphite samples and fruitful discussions, respectively.

References

[1] J.A. Seel, J.R. Dahn, J. Electrochem. Soc., **147** (3), 892-898 (2000).

[2] F. Rosciano, M. Holzapfel, H. Kaiser, W. Scheifele, P. Ruch, M. Hahn, R. Kötz, P. Novák, J. Synchrotron Rad. **14**, 487-491 (2007).

.

In situ Raman microscopy of graphite electrodes

A. Hintennach, P. Novák

phone: +41 56 310 4542, e-mail : andreas.hintennach@psi.ch

Increasing cost for the supply with fossil fuels and the need of reduction of carbon dioxide emissions claim the need of fuel-efficient cars. With electricity-based hybrid drivetrains the fuel-efficiency can be significantly increased. An important part in the hybrid concept is the energy storage unit, usually a battery. Due to their high energy density and long-term stability, lithium-ion batteries play therefore a gradient role in individual mobility.[1-3] Graphite is the preferred material for the negative electrodes of lithium-ion batteries. Graphite is also used as a conductive additive in positive electrodes. One of the limiting factors concerning the life-time are deterioration effects caused by changes in the morphology of the graphite. These changes in the morphology can be induced by exfoliation of the graphite and can accordingly be detected as permanent changes in its structure (refer to Figure 1 for SEM images) with *in situ* Raman microscopy (refer to Figures 2 and 3 for examples). In order to determine the mechanisms of aging and the relationship between micro-, nano-, and defect structure, *ex situ* Raman microscopy [4] was used in previous work.[5-9] This type of Raman microscopy offered resolutions of around 1 μm^3. It was subsequently enhanced to methods of *in situ* Raman microscopy mapping the whole surface of electrodes, in order to describe the mechanisms of intercalation processes of lithium-ions into graphite materials. This mapping method is now used in a more advanced way to determine the process of exfoliation of the used graphites and to correlate information from *in situ* Raman microscopy and *post mortem* SEM images.[10, 11] In particular, the exfoliation process at very positive potentials is investigated here.

Experimental

Graphite (90 %, SFG44, TIMCAL SA, Bodio, Switzerland) was used as an electrically conductive model "additive". Polyvinylidene fluoride binder (8 %, PVDF SOLEF 1015, Solvay) was dissolved in *N*-methyl-pyrrolidinone (NMP, Fluka) and Triton X-100 (2 %, Sigma-Aldrich) was used to avoid agglomerations during the preparation of the electrodes. The proportion of the materials used for the preparation of the electrodes equals to 90:8:2 by mass. All used materials were mixed with an ultra-sonic stirrer (Hielscher UP200H, Teltow, Germany) for 2 minutes at 100 % amplitude. The suspensions were doctor-bladed at a height of 250 µm on a carbon coated aluminum foil (GAIA, Nordhausen, Germany) and dried under vacuum at 110°C overnight to prepare the electrodes. Afterwards circular working electrodes with a diameter of 13 mm were punched out and dried under vacuum at 120°C overnight. Then the *in situ* Raman cell was assembled with a fiber glass separator (1 mm) which ensured the distance between metallic lithium and the working electrode while being soaked with 300 µl of electrolyte (1 M $LiClO_4$ in acetonitrile). The metallic lithium served as both reference and counter electrode. *In situ* Raman spectra were collected at 25°C with a confocal Raman microscope (LabRAM series, HoribaJobinYvon SA), using a Helium Neon laser as exciting source (632.8 nm, 7 mW). The laser light was focused through a small hole (d = 1 mm) in the current collector onto the surface of the electrode with a 80x objective (Olympus) and filtered to 0.9 mW to avoid thermal degradation of the electrode. The electrodes of the cell were galvanostatically cycled from 2.0 to 5.5 V vs. Li/Li^+ to study exfoliation even at very positive potentials.

After disassembly of the electrodes of the *in situ* Raman cell, the electrodes were washed with pure acetonitrile. Then SEM images were recorded (Zeiss Supra 55, InLens, 3 kV*)* to give a *post mortem* overview of the surface of the electrodes.

Results and discussion

Both SEM images in Figure 1 show highly exfoliated particles on the surface of graphite electrodes as a consequence of electrochemical cycling up to very positive potentials (+5.5 V vs. Li/Li^+).

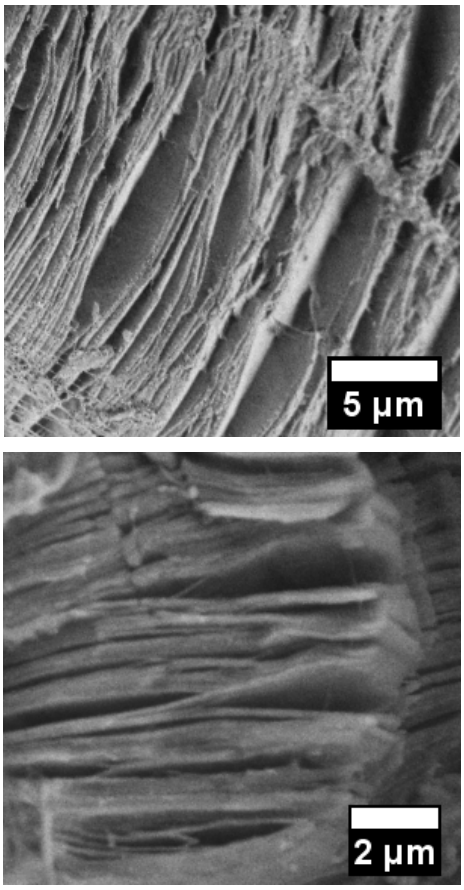

Figure 1. *SEM images of exfoliated parts of electrodes (graphite: SFG44) after electrochemical cycling (2.0-5.5 V vs. Li/Li^+).*

In addition to these *post mortem* information provided by SEM images, electrochemical cycling with *in situ* Raman microscopy offers information concerning the structure of the used graphite in real-time and therefore correlated with the electrochemical state of the electrodes. With spectral information from previous work [9, 12] new indicators of the exfoliation processes were found.

The position, shape, and magnitude of the D- and G-bands was previously used to describe the state of the intercalation process of lithium ions into graphite materials and to calculate the L_a value from the Tuinstra and Koenig equation [13], which provides a measure of the local surface disorder and represents the length of the graphene crystallite sheets. Moreover an E-band assigned to the exfoliation of graphite has been detected at lower potentials of the negative electrode (refer to Figure 2).[11, 14]

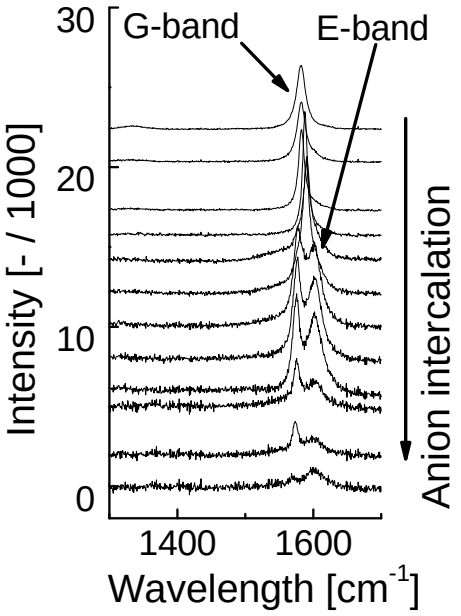

Figure 2. *G- and E-band during electrochemical cycling (2.0-5.5 V). The relation of the integrals of the G- and E-band is determined for the exfoliation process at very positive potentials.*

This E-band was here detected for very positive potentials and is used in addition to the relation of the D- and G-bands to give new markers for *in situ* Raman measurements. Therefore an investigation of exfoliation processes is henceforward facilitated due to the described set of spectral information (D-band shift and the relation of the integrals of D- and G- or E-band, respectively).

Figure 3 shows the shift of the D-band in the spectrum of graphite material during electrochemical cycling. After completed electrochemical cycling, the remaining shifts indicate exfoliated areas and can be detected and correlated with SEM information to give space-resolved mappings of the surface of the electrode.

The combination of *in situ* Raman and *post mortem* SEM information offers therefore a new possibility to describe the surface of electrodes for lithium-ion batteries with respect to exfoliation effects at high potentials, correlated with electrochemical behavior of these electrodes.

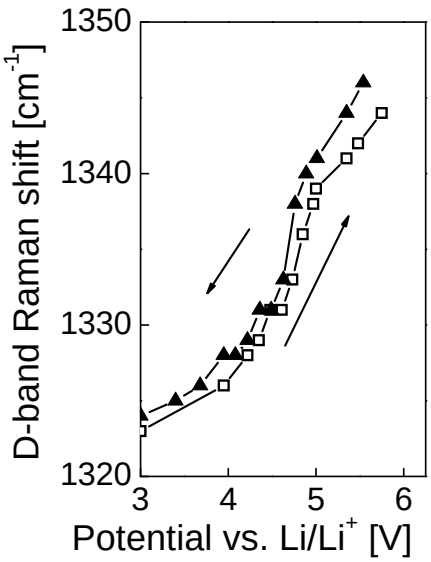

Figure 3. *Shift of the D-band of the Raman signal of a graphite electrode. The specific shift indicates exfoliation processes and can be used as marker signal in addition to the relationship of the D- and G-band of the Raman signal.*

References

[1] E. Karden, P. Shinn, P. Bostock, J. Cunningham, E. Schoultz, D. Kok, J. Power Sources **144**, 505-512 (2005).

[2] J. Milliken, F. Joseck, M. Wang, E. Yuzugullu, J. Power Sources **172**, 121 - 131 (2007).

[3] T. Kojima, T. Ishizu, T. Horiba, M. Yoshikawa, J. Power Sources, Article in Press, Corrected Proof. doi: 10.1016/ j.jpowsour. 2008.1010.1082 (2009).

[4] R. Baddour-Hadjean, S. Bach, M. Smirnov, J.P. Pereira-Ramos, J. Raman Spectrosc. **35**, 577-585 (2004).

[5] D. Goers, H. Buqa, L.J. Hardwick, A. Wuersig, P. Novák, Ionics **9**, 258-265 (2003).

[6] L.J. Hardwick, H. Buqa, P. Novák, Solid State Ionics **177**, 2801 (2006).

[7] L.J. Hardwick, P. Novák, GDCh-Monograph **32**, 220-228 (2005).

[8] L.J. Hardwick, PhD thesis No. 16992, ETH Zürich (Zürich), 2007.

[9] L.J. Hardwick, M. Marcinek, L. Beer, J.B. Kerr, R. Kostecki, J. Electrochem. Soc. **155**, A442-A447 (2008).

[10] H. Buqa, A. Wuersig, D. Goers, L.J. Hardwick, M. Holzapfel, P. Novák, F. Krumeich, M.E. Spahr, J. Power Sources **146**, 134-141 (2005).

[11] M.E. Spahr, H. Buqa, A. Würsig, D. Goers, L.J. Hardwick, P. Novák, F. Krumeich, J. Dentzer, C. Vix-Guterl, J. Power Sources **153**, 300-311 (2006).

[12] L.J. Hardwick, P.W. Ruch, M. Hahn, W. Scheifele, R. Kötz, P. Novák, J. Phys. Chem. Solids **69**, 1232-1237 (2008).

[13] F. Tuinstra, J.L. Koenig, J. Chem. Phys. **53**, 1126-1130 (1970).

[14] L.J. Hardwick, H. Buqa, P. Novák, Solid State Ionics **177**, 2801-2806 (2006).

Failure mode of the commercial supercapacitor BCAP350

R. Kötz, P. Ruch, D. Cericola

phone: +41 56 310 2057, e-mail: ruediger.koetz@psi.ch

The failure mode of supercapacitors is of utmost importance for the design of reliable and safe applications. Particularly, the failure mode of capacitors in modules with many capacitors connected in series determines the design strategy. If the capacitor would fail in an open circuit mode, the total module fails. On the other hand, if the capacitor develops a short circuit, the module will function properly with a slightly increased voltage of the single capacitors [1]. In the present communication, the failure mode of commercial capacitors of the type BCAP350 from Maxwell Technologies was investigated during accelerated constant voltage load tests.

Experimental

In order to determine the failure mode of commercial capacitors, several BCAP350 from Maxwell Technologies were tested at elevated temperatures at constant load (constant voltage) until the capacitors failed or until the end of life criteria, which corresponds to 20% capacitance loss and/or doubling of the internal resistance, were reached.

The test setup consisted of a power supply, a switching unit and a temperature-controlled chamber. In order to be able to test many capacitors with a single power supply, the capacitors were charged one by one and held at open circuit afterwards. During the open circuit period of one capacitor, the power supply was free to charge other capacitors. When the voltage of the capacitor reached a certain lower voltage limit, typically 50 mV below the nominal voltage, the capacitors were recharged. From the time, current and voltage difference for recharge the capacitance was calculated. From the open circuit time we calculated the average leakage current and from the voltage jump during current switching the internal resistance was determined. For each experiment, typically five capacitors were tested to assess the reproducibility. Tests were performed at different temperatures between 30ºC and 85ºC and at different voltages between 2.5 V (nominal voltage) and 3.5 V.

Results

As a reference, the behaviour of a capacitor in terms of capacitance and resistance at nominal conditions (2.5 V and 30ºC) is reproduced in Figure 1. During the test time of more than 3 months, the capacitance decreased by about 10 % and the internal resistance increased by 20 %. Both values are far below the end of life criteria, which correspond to 20 % capacitance loss and 100 % resistance increase.

The decay of the leakage current is also reproduced in Figure 1. A drastic decrease of the leakage current by about 3 orders of magnitude is observed. This finding is rather important for backup applications of supercapacitors where the capacitor has to be trickle charged permanently.

As expected and demonstrated in a previous investigation, the rate of aging of the capacitors increased with temperature and with load voltage [2].

However, none of the tested capacitors developed a short circuit, an open circuit state or any other catastrophic failure mode.

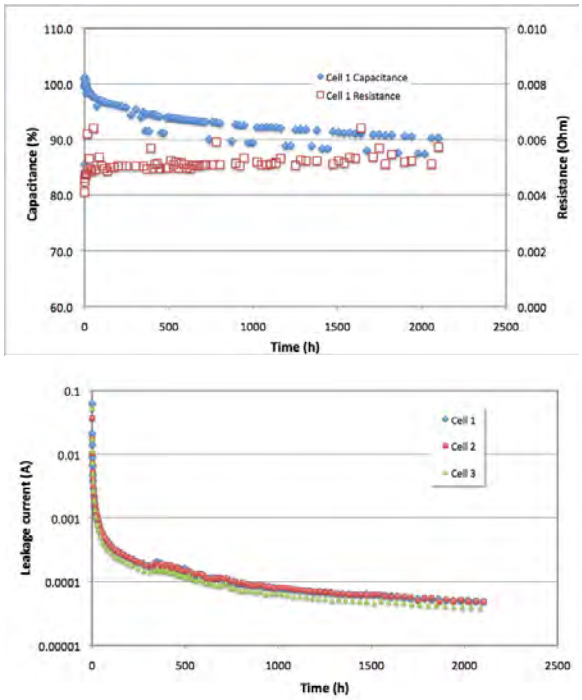

Figure 1. *Capacitance (top) and leakage current (bottom) of a BCAP350 during constant load test at nominal conditions of 2.5 V and 30ºC.*

In most cases, the aging of the capacitors was continuous and predictable, i.e. the capacitance decayed monotonically with time while the internal resistance increased. This finding is rather important for the possible failure mode of a capacitor module, which would totally fail in case of an open circuit for one of the capacitors.

The only drastic failure mode observed was can opening at the predesigned pressure valve which is supposed to open at about 14 bars internal pressure. This process was observed for all five capacitors during the test at a temperature of 70ºC and at 3.0 V load voltage.

The typical capacitance, internal resistance and leakage current evolution during this test is reproduced in Figure 2 for one of the five capacitors. While the capacitance decrease was accelerated after can opening, the internal resistance increases significantly. In addition,, the leakage current shows a sharp jump of one order of magnitude after can opening.

However, even after can opening the capacitor functioned safely for some time, with decreasing performance.

The most significant change after can opening was observed for the leakage current, which increased drastically. Therefore, monitoring of the leakage current would be an important means to detect the failure of

capacitors in a module. In all other tests without can opening, the leakage current decreases monotonically during the constant load test.

The evolution of the capacitance and the internal resistance for the test at 70°C and 3.0 V is shown in Figure 2 for one of five capacitors. The capacitance has decreased by 20% after 150 hours. After about 180 hours the pressure valve of the capacitor opened, resulting in a

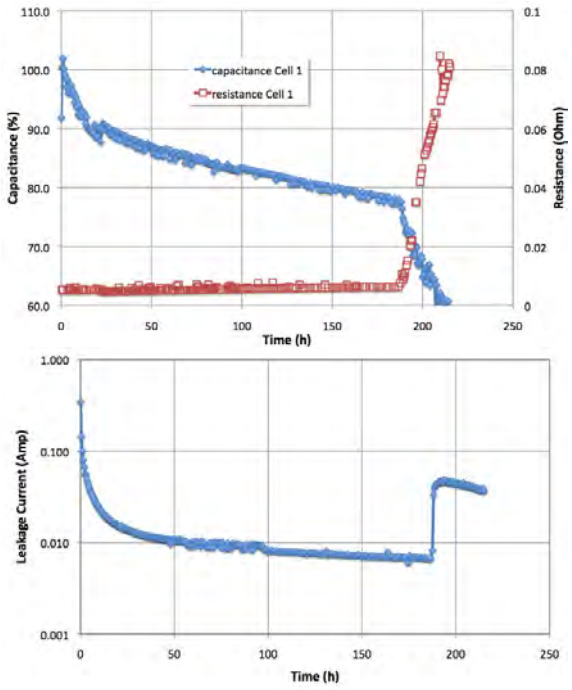

Figure 2. *Capacitance and internal resistance (top) and leakage current (bottom) of a BCAP350 tested at 3.0 V and 70ºC.*

sharp step-like increase of the leakage current by one order of magnitude. Simultaneously, the capacitance decreased and the internal resistance increased. For the four other capacitors, the qualitative behaviour is identical, with the only difference that can-opening occurred at different times between 120 h and 190 h.

Figure 3. *Picture of the opened can of a BCAP350 capacitor after the test at 70ºC and 3.0 V.*

During can opening some of the electrolyte is lost, which is visible by the salt deposit at the opening (see Figure 3). The decrease in capacitance and the increase in resistance can be tentatively explained by the loss of electrolyte. The increased leakage current most probably is a consequence of moisture entering the capacitor.

Conclusion

Supercapacitors perform well at rather high temperatures or high voltages for at least 100 hours before the end-of-life criteria are reached. Therefore, extreme imbalance of voltage or temperature within a module will not result in an instant failure of the capacitors. There will be sufficient time to take countermeasures or shut down the module in a controlled way.

Supercapacitors at high temperatures (≈ 85ºC) or at high voltages (≈ 3.5 V) do not develop a short or open circuit state when failing. This is important for the performance of large capacitor modules.

If the capacitors fail it is by can opening as a consequence of internal pressure developed by electrolyte decomposition.

In terms of electric performance, the capacitance and internal resistance decrease or increase in a monotonous way.

The leakage current, which is important for backup applications, decreases by several orders of magnitude during constant load tests.

In most cases, the end-of life criteria of 20% capacitance loss and doubling of the internal resistance are reached before failure by can opening occurs.

Acknowledgement

We thank Dr. O. Barbieri of Maxwell Technologies SA for providing the BCAP350 capacitors.

References

[1] R. Kötz, J.-C. Sauter, P. Ruch, P. Dietrich, F.N. Büchi, P.A. Magne, P. Varenne, J. Power Sources, **174,** 264-271 (2007).

[2] R. Kötz, M. Hahn, R. Gallay, J. Power Sources **154**, 550–555 (2006).

Colorimetric determination of lithium content in electrodes of lithium-ion batteries

P. Maire, A. Evans, H. Kaiser, W. Scheifele, P. Novák

phone: +41 56 310 5810, e-mail: pascal.maire@psi.ch

We have recently shown that the state of charge (SOC) of a lithiated graphite electrode can be determined by measuring its color [1]. Graphite is known to undergo a color change upon intercalation of lithium, from black in the pristine state to golden yellow in the fully charged state of composition LiC_6. Intermediate compounds are of dark blue and reddish color. The color of electrodes - expressed as intensities of red, green, and blue color components - is easily measured using a digital photo camera. Once a quantitative correlation between RGB-color values and lithium content is established, the RGB values of each pixel in a photograph can be directly translated into values of SOC. The colorimetric method was used for the post mortem analysis of negative electrodes from aged lithium-ion batteries. Colorimetry revealed a very uneven distribution of lithium in electrodes of aged lithium-ion batteries [2]. Heterogeneous distribution of lithium in the battery may lead to local overcharging of the electrode materials, with the consequences of premature ageing and even safety problems.

However, because standard batteries have to be opened and thus destroyed to perform a colorimetric analysis, it was not possible to follow the evolution of lithium distribution over the whole lifespan of a battery electrode. In this contribution we describe the design and application of a novel electrochemical cell for *in situ* colorimetric investigation of battery materials.

Cell design and testing

In order to obtain a quantitative correlation between a graphite electrode's lithium content and its color, a newly developed electrochemical cell with a glass window was used (Figure 1).

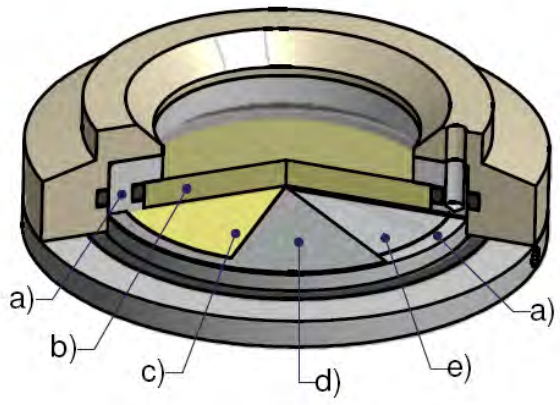

Figure 1. *Drawing of the newly developed electrochemical cell with glass windows. a) Titanium current collectors; b) glass window; c) graphite (or other) electrode on stainless steel mesh; d) separator (glass fiber or porous polyolefin); e) lithium counter electrode.*

The cell permits to follow color changes *in situ*, while the graphite is charged and discharged. The graphite active material is coated onto a metal mesh current collector, which enables transverse electrolyte diffusion. Working and counter electrode are connected by ring-shaped titanium current collectors. A glass window of 28 mm diameter coated with an anti-reflex layer permits taking pictures of the electrode during electrochemical cycling. Graphite electrodes were cycled vs. metallic lithium at low rate, typically C/24, and pictures were taken every 5 min. The color components expressed in values of red R, green G, and blue B were averaged over an area of 50 × 50 pixels on the electrode surface and plotted vs. the state of charge (Figure 2).

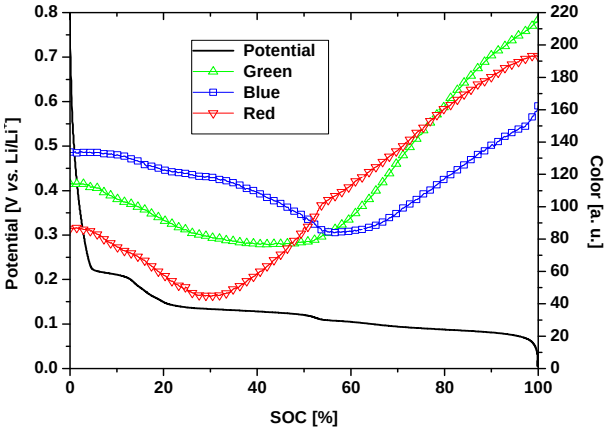

Figure 2. *Calibration curves for electrodes composed of graphite SFG44 (90%) and PVDF (10%).*

Graphite electrodes showed excellent stability when cycled vs. metallic lithium in the glass cell (within 20 cycles the discharge capacity was still > 98% of the initial value, and the irreversible capacity loss was less than 0.4 % for cycles 4 to 20). The optical properties of the electrode remained stable during electrochemical cycling, as shown in Figure 3.

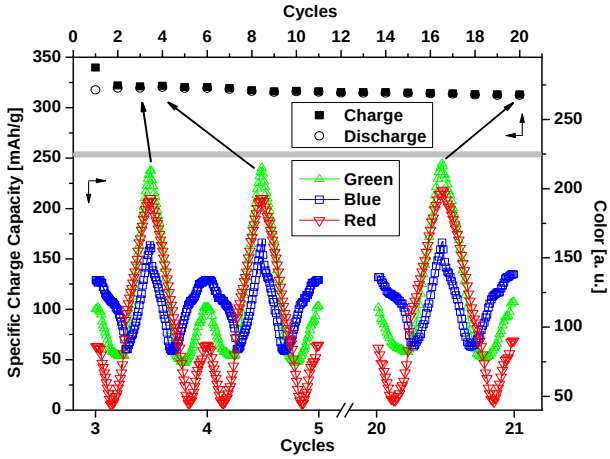

Figure 3. *Demonstration of the excellent stability of both capacity (top/left axes) and color response (bottom/right axes) during prolonged cycling.*

Kinetic studies

The knowledge of intercalate diffusion processes within host materials and the electrolyte constitutes an important aspect of battery designs. In view of the large inhomogeneities found in negative electrodes of aged high-power cells (Figure 4), electrodes permitting a faster diffusion of lithium should be developed. In this way local overcharging or over-discharging leading to irreversible structural changes in the active material could be prevented. Several factors like crystallinity and particle size of the carbon material, porosity and thickness of the electrode, or the presence of conductive additives influence the apparent diffusion coefficient of lithium in composite electrodes. A simple yet reliable procedure to measure these diffusion coefficients is thus needed for fast screening of different electrode formulations.

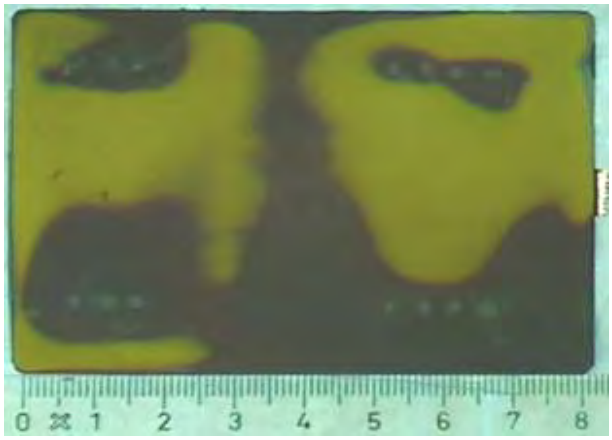

Figure 4. *Negative electrode of a commercial high-power cell after 800 cycles at a charge and discharge rate of 6 C.*

The combination of good spatial and temporal resolution predestines colorimetry in the glass cell as a tool to study the kinetics of lithium distribution in composite electrodes. It was of interest to measure the rate at which an inhomogeneous lithium distribution equilibrates. To induce an artificial inhomogeneity, the circular lithium foil serving as counter electrode was replaced by a semicircle covering only half the cell surface (Figure 5). Charging of a graphite composite electrode in such a cell led to two distinct domains: the part opposed to the lithium counter electrode became fully lithiated, while the rest of the electrode remained practically uncharged (Figure 5c). The diffusion of lithium into the yet uncharged parts was monitored while the cell voltage was kept at 5 mV vs. Li/Li^+ (Figure 5c → 5d). Pictures were taken in intervals of 1 h and analyzed using the calibration curves shown in Figure 3. The growth rate of the highly lithiated yellow part is a direct measure for the mobility of lithium in the electrode. In Figure 6 the propagation of a borderline between graphite containing more than 0.75 lithium ions per six carbon atoms ($x > 0.75$ in Li_xC_6) and the rest of the electrode is shown. We propose to use the slope of these curves as an indicator of lithium mobility in composite graphite electrodes. The example of two cells kept at 10 °C and 50 °C respectively demonstrates the increased mobility of lithium ion at elevated temperatures.

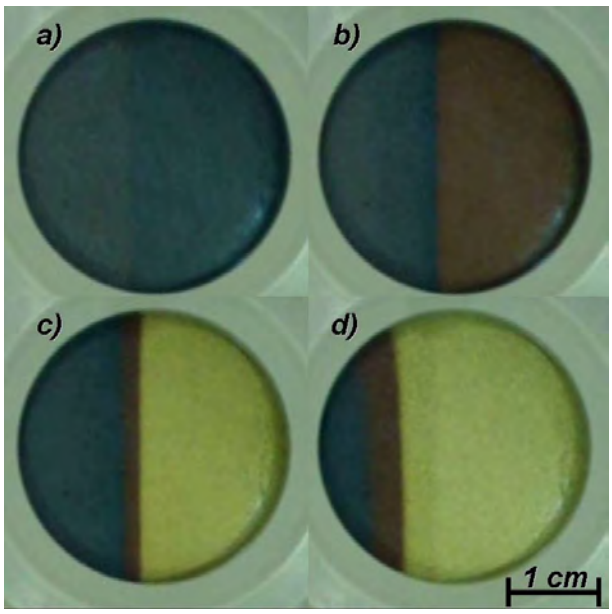

Figure 5. *Kinetic studies using the newly developed glass cell. The pictures shown here were taken at 0 h (a), 11 h (b), 26 h (c), and 110 h (d).*

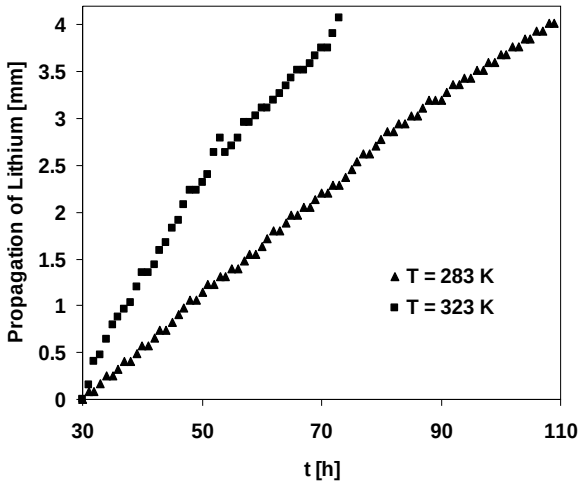

Figure 6. *Temperature dependent equilibration of heterogeneously charged composite graphite electrodes.*

Conclusion

Experiments with the newly developed glass cell can lead to a better understanding of the processes occurring in the graphite electrodes used in lithium-ion batteries and finally to improved electrodes.

References

[1] W. Scheifele, P. Maire, P. Novák, PSI Electrochemistry Laboratory - Annual Report 2007, 46 ISSN No. 1661-5379 (2008).

[2] P. Maire, A. Evans, H. Kaiser, W. Scheifele, P. Novák, J. Electrochem. Soc. **155** (11), A862-A865 (2008).

Time-dependency of electrolyte wetting of graphite electrodes

W. Märkle, D. Goers[1], M. E. Spahr[1], P. Novák

phone: +41 56 310 2474, e-mail: wolfgang.maerkle@psi.ch

Graphite is commonly used as active material for the anode in lithium-ion batteries due to its low cost, good cycleability, and reasonable specific charge [1]. In applications which require high current rates, e.g., for electric or hybrid vehicles, fast kinetics of the graphite electrode are inevitable. For that purpose, a large contact area between the graphite particles and the electrolyte is desired [2]. Therefore porous electrodes, which contain small active particles kept together with a binder, are used. The porosity is responsible for the drastically increased internal surface compared to the geometrical surface. Thus, a large number of reaction sites where the Li^+ insertion/deinsertion in the particles can take place is provided. Nevertheless, a full utilization of the electrode can be achieved only if the internal surface is completely wetted, which means that all pores are filled [3]. If the electrode is soaked with electrolyte during cell assembling, it is expected that the whole internal surface of the active mass is not wetted immediately but it takes a certain time until the pores are filled. Additionally, the porosity of the electrode is not uniform but consists of macro-, meso-, and micropores, which are filled at different rates. Parameters which may influence the overall wetting time of the electrode are particle size and morphology, active mass density, electrolyte, pressure in the cell, and temperature. Herein, we report the time dependent wetting behaviour of a porous graphite electrode with electrolyte after assembling the cell. As indicator, the capacitance of the double layer, which is related to the wetted area, was followed within certain time intervals. Additionally, the influence of vinylene carbonate, an electrolyte additive beneficial for improving the performance of graphite anodes [4], on the wetting behaviour was investigated.

Experimental

Electrodes were prepared from a mixture of 91% TIMREX® SFG10, 1% carbon black, and 8% polymeric binder PVDF1015. All components were dispersed in N-methylpyrrolidon. After casting the dispersion on a copper foil and drying, electrode disks (1.32 cm^2, mass loading 4.6 – 4.9 mg) were punched out and the thickness of the active layer was adjusted to 30 +/- 3 µm by rolling. The density of the active mass was thus set to about 1.3 g/cm^3, corresponding to a void volume of 46-49 %. The electrodes were afterwards vacuum dried at 120°C for 12 h. In an argon filled glove box, two electrodes were symmetrically arranged in a lab cell with their active layer “face to face” and an electrolyte soaked glass fiber separator in between. The pressure on the electrodes was set with a spring to 2 kg/cm^2. As electrolyte, a mixture of ethylene carbonate (EC) and dimethyl carbonate (DMC) 1:1 (w/w), 1 M $LiPF_6$ was used with and without 1% (w/w) vinylene carbonate (VC). Impedance spectra were recorded after short circuiting the cell. The frequency range was 100 kHz to 100 mHz, the amplitude was set to 10 mV. All times reported are related to the final assembly step of the cell (tightening with a torque wrench). The cells were stored and measured at 25 °C.

Results

The impedance spectra of the symmetrical cell, recorded at different times after assembling, are shown in Figure 1. All spectra have a similar shape with a semicircle at high frequencies and a tail at lower frequencies originating from diffusion processes.

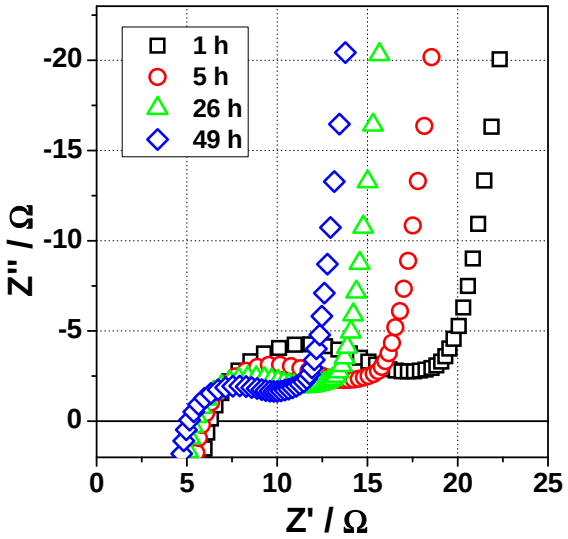

Figure 1. *Impedance spectra of two symmetrically arranged graphite electrodes in EC:DMC 1:1 (w/w), 1 M $LiPF_6$ at different times after cell assembling.*

The semicircle becomes smaller the longer the cell is stored, revealing a decrease in the overall resistance during storage. These spectra can be represented by the model of a Randles equivalent circuit [5], where an Ohmic resistance R_s is coupled in series with a parallel circuit of a double layer capacitance C_{dl} and an Ohmic resistance R_{ct} due to a charge transfer (polarization) resistance. The latter is additionally coupled in series with a diffusion element, which was neglected in our considerations. The intersections of the semicircle (which has to be fitted in the spectra) with the x-axis at Z'' = 0 Ω represent the values of R_s and R_s+R_{ct} respectively. For C_{dl}, which is proportional to the wetted area, the following equation is valid:

$$C_{dl} = \frac{1}{R_{ct} \cdot \omega_m}$$

with ω_m as the frequency at the top of the semicircle. R_{ct} corresponds to the distance between the two intersections of the semicircle with the x-axis at Z'' = 0 Ω. The double layer capacitance C_{dl} rises during the storage of the cell (Figure 2), indicating an increasing contact area between the particles and the electrolyte. Even after 80 h the wetting of the porous electrodes, prepared as described and under the given experimental conditions, is not yet complete. Therefore, some parts of the electrode might be still inactive if it would be electrochemically utilized at this time. It is suggested that gas trapped in the pores hinders the penetration of the electrolyte in the electrode active mass.

[1] TIMCAL Ltd., Bodio

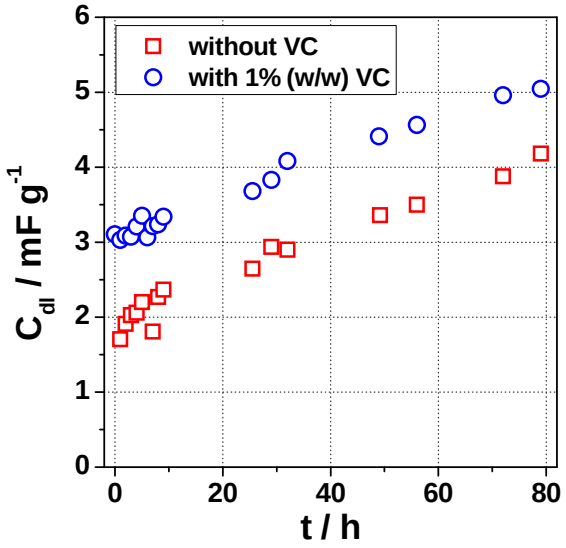

***Figure 2**. Double layer capacitance of the electrodes in EC:DMC 1:1 (w/w), 1 M $LiPF_6$ with and without VC at different times after cell assembling.*

If 1% (w/w) vinylene carbonate is added to the electrolyte, the double layer capacitance is remarkably higher throughout the whole experiment compared to pure EC:DMC 1:1, 1 M $LiPF_6$, although both wetting rates are similar. Probably this behaviour is not due to a change in viscosity by the additive but due to different interactions of the vinylene carbonate containing electrolyte with the graphite surface, resulting in an increased value of C_{dl} per active mass unit. This is supported by the fact that the wetting rate of the two electrolytes is not remarkably different.

If the cell is stored for a longer time (about one week and more), a massive increase of the semicircle can be observed (Figure 3). The behaviour for the pure EC:DMC 1:1, 1 M $LiPF_6$ electrolyte is similar but with a significant longer delay of the increase (not shown here).

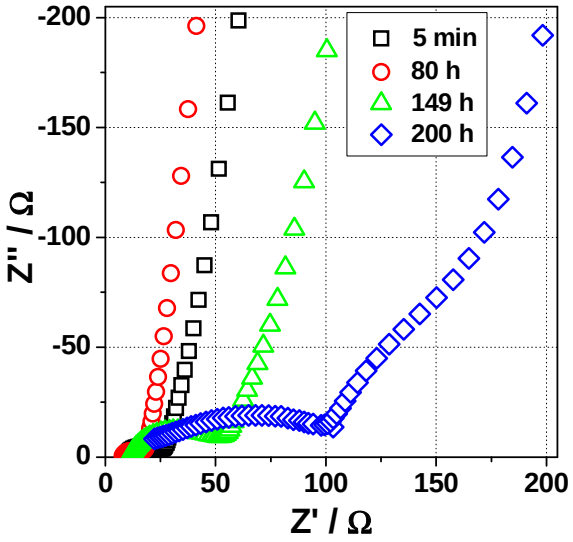

***Figure 3.** Impedance spectra of two symmetrically arranged graphite electrodes in EC:DMC 1:1 (w/w), 1 M $LiPF_6$ + 1% VC at different times after cell assembling.*

Additionally, the semicircle at high frequencies becomes distorted, pointing to additional processes, which can no longer be described with the simple Randles circuit. The Nyquist plot resembles that of an electrode with a SEI layer formed by electrolyte reduction [4]. Post-mortem Scanning Electron Microscopy (SEM) of the electrode stored in the cell over 200 h shows clearly the coverage of the particles with a layer (Figure 4), which obviously stems from electrolyte decomposition.

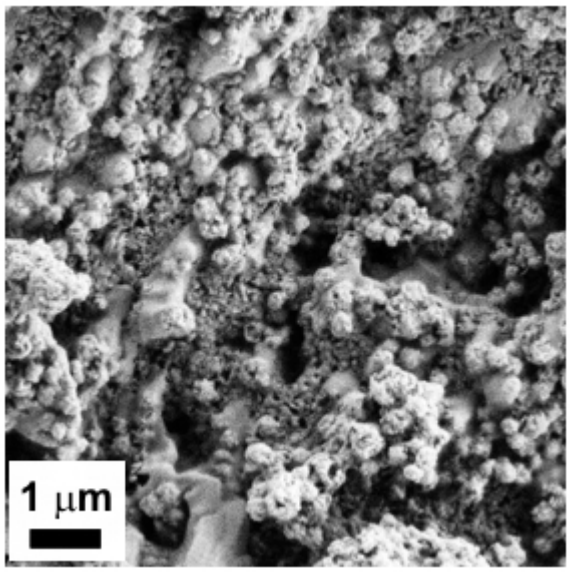

***Figure 4**. Post-mortem SEM of a graphite electrode after long-term storing in EC:DMC 1:1 (w/w), 1 M $LiPF_6$ + 1% VC.*

The trigger for this decomposition reaction is not yet clear. Possibly, a shift in the electrodes' open circuit potential during storage induces an electrochemical process which starts a polymeric chain reaction. It also might be that surface groups on the graphite particles interact with the electrolyte molecules.

The results show that a fairly long time is needed for the electrolyte to penetrate a porous electrode and wet the entire graphite surface even is pressure is applied. To get more insight about the parameters which influence the wetting time, especially the pore size distribution and its consequence on the electrochemical behaviour, will be subject of further investigation.

References

[1] M. Winter, J. O. Besenhard, M. E. Spahr, P. Novák, Adv. Mater. **10**, 725-763 (1998).

[2] M.-S. Wu, T.-L. Liao, Y.-Y. Wang, C.-C. Wan, J. Appl. Electrochem. **34**, 797-805 (2004).

[3] P. Novák, W. Scheifele, M. Winter, O. Haas, J. Power Sources **68**, 267-270 (1997).

[4] D. Aurbach, K. Gamolsky, B. Markovsky, Y. Gofer, M. Schmidt, U. Heider, Electrochim. Acta **47**, 1423-1439 (2002).

[5] E. Barsoukov, J. R. MacDonald (eds.), Impedance Spectroscopy. Theory, Experiment, and Applications 2nd ed., 70 (2005).

Measuring current density distribution across an electrode with the multiple-working-electrode electrochemical cell

S.H. Ng, F. La Mantia, P. Novák

phone: +41 56 310 2457, e-mail: petr.novak@psi.ch

One of the requirements needed for the mass production of lithium-ion batteries for use in the HEV applications is to increase the rate capability of the electrode materials [1]. However, the rate capabilities of both negative and positive electrode materials are hindered due to the non-uniformity of current density distribution (CDD) across the porous electrode with increasing specific current applied [2]. Therefore, it is important to understand the degree of this non-uniformity across a porous electrode (perpendicular to the current collector), which is the general case for Li-ion batteries.

In the literature, there are mainly two classes of models on CDD in porous electrodes, two-phase and single-phase models. For a two-phase model, the liquid electrolyte and the solid electrode are treated as separate phases [3]. The pores have a well-defined geometrical shape. Meanwhile, the single-phase model considered the current to be generated in the volume of the porous electrode [4]. In 1962, Newman and Tobias [5] introduced the effect of diffusion along the x-axis and the dependence of the polarization resistance on the CDD in the single phase model [4]. The transmission line model (TLM), developed by de Levie in the middle of the 1960's [6] is based on the two-phase model of Daniel-Bekh [3], and considers only the radial diffusion of reactants and products.

In summary, most of the research work on the specific current distribution in the Li-ion battery system performed until now was mainly focused on theoretical modeling or dynamic simulations. Herein, we report on a multiple-working-electrode (MWE) electrochemical cell (see Figure 1a) with the capability to measure directly and quantitatively the CDD across the electrode thickness, where inhomogeneity in CDD occurs due to the different electrochemical overpotentials across the electrode thickness, mainly due to concentration effects [7]. To the best of our knowledge, this is the first time in the Li-ion battery field that a "real" experimental result is directly obtained rather than based on theoretical or mathematical modeling.

Experimental

TIMREX® SFG44 synthethic graphite (TIMCAL SA, Switzerland) was applied as the electroactive material. The graphite negative electrodes were prepared by doctor-blading slurries of graphite active material (90 wt.%) and poly(vinylidene fluoride) binder (10 wt.%, SOLEF 1015, Solvay SA) in a N-methylpyrrolidinone (NMP) solvent, onto a non-adhesive paper, from which the electrode mass was easily removed once dried. The electrodes were vacuum dried at 120 °C overnight. After drying, these free-standing electrodes (2 cm x 2 cm) were removed from the non-adhesive paper and subsequently pressed onto the respective current collectors (expanded copper mesh, ~50 µm thick). The mass loading of each working electrode (WE) was typically 3-4 mg of active material per cm^2. "Coffee bag"-type composite foil [8] is used as the host/body for the MWE electrochemical cell assembly. All cell components are dried in vacuum at 120 °C overnight and subsequently transferred into an argon-filled glove box. Finally, in the glove box, the MWE electrochemical cells are assembled through precise layer-by-layer arrangement of the WEs (see Figure 1a). Each WE and the counter electrode (from metallic lithium) are separated via a layer of polymeric separator (Celgard 2500) soaked with a standard battery electrolyte (1 M $LiPF_6$ in EC:DMC (1:1), Ferro GmbH), which was placed in-between each electrode. The neatly arranged electrode stack was later vacuum-sealed in the "coffee bag"-type cell. Galvanostatic measurements were performed at a specific current of 10 mA g^{-1} (of graphite) in order to complete the solid electrolyte interphase (SEI) formation in the first electrochemical cycle. When a potential of 5 mV vs. Li/Li^+ was reached, the lithiation step was continued until the total specific current dropped below 5 mA g^{-1}. The delithiation step was performed at a constant specific current of 10 mA g^{-1} until a cut-off potential of 1.0 V vs. Li/Li^+. In addition, the specific current for each WE was monitored using individual general-purpose potentiostats, which are labeled as P1 to P3 in Figure 1b.

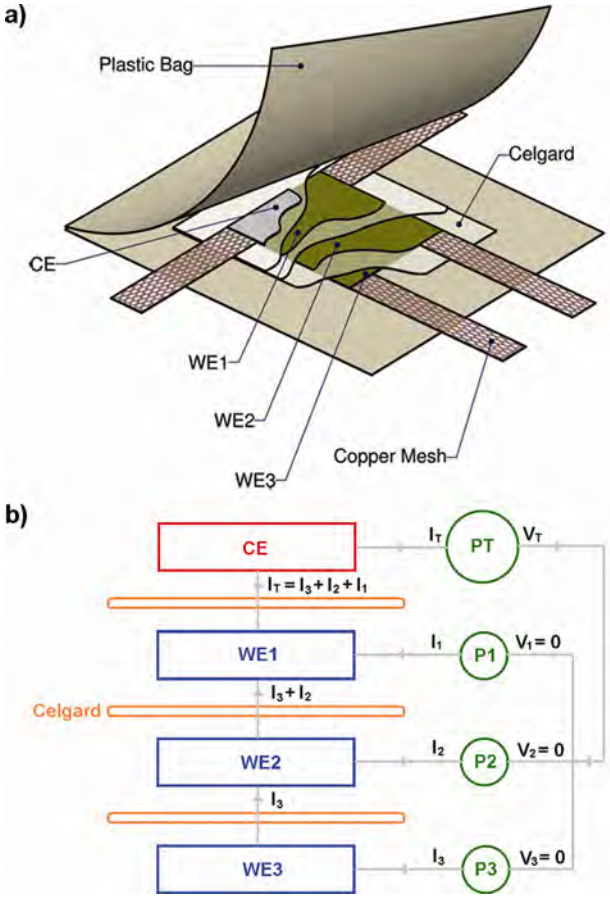

Figure 1. *(a) Sketch of the MWE electrochemical cell. (b) Schematic representation of the electrical circuit applied in this study.*

Results

The electrical connections between the WEs for this CDD study are of utmost importance because the main objective of this study is to quantify the specific current for each WE, while neglecting the mutual influence of each WE. In order to achieve this objective, we have applied 3 additional potentiostats (P1, P2, and P3) for direct measurement of the respective specific current that passed into each layer of the WEs, as shown in Figure 1b. The role played by each of these potentiostats in this case could be likened to a "current follower" [9], which is a device measuring current without inducing a potential drop.

Graphite was chosen as the model negative working electrode material in this study because non-uniform CDD in graphite electrodes is a scientific challenge in the Li-ion battery system [2]. Furthermore, graphite electrodes also provide an additional proof of non-uniformity in CDD via color change [10]. In order to demonstrate these phenomena without a noticeable influence of other electrochemical cycling parameters, the galvanostatic measurements were performed at very low C-rates, namely at approximately C/37 rate (~10 mA g^{-1}). The first galvanostatic cycle in which the SEI layer is formed is not shown here.

Galvanostatic plot of the second electrochemical reduction cycle is shown in Figure 2. We could clearly observe that the nearer the working electrode (WE1) to the counter electrode (CE), the higher the specific charge achieved. The redox plateaus were also better defined when the working electrode was nearer to the CE, due to lower overpotential of the electrode. During the reduction process (Li^+ insertion) in the second cycle, the specific charge differences between the WEs when compared to the total charge applied were +4.6 %, -1.1 %, and -3.5 %, for WE1, WE2, and WE3, respectively. Therefore, even at the low C-rate cycling of the MWE cell, we could still observe an inhomogeneity in the average CDD of more than 8 %.

It is possible to estimate the state of charge (SOC) of a graphite negative electrode using an *in situ* colorimetry technique [10]. This technique is based on the fact that the graphite negative electrode has different colors at different levels of lithiation, where golden-yellow regions are lithium-rich while dark regions are lithium-deficient.

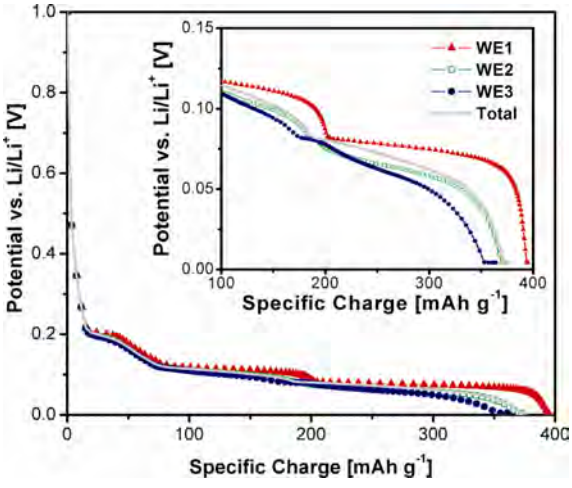

Figure 2. *Galvanostatic plot of the MWE cell in the second electrochemical cycle during reduction, with inset showing the enlarged plot.*

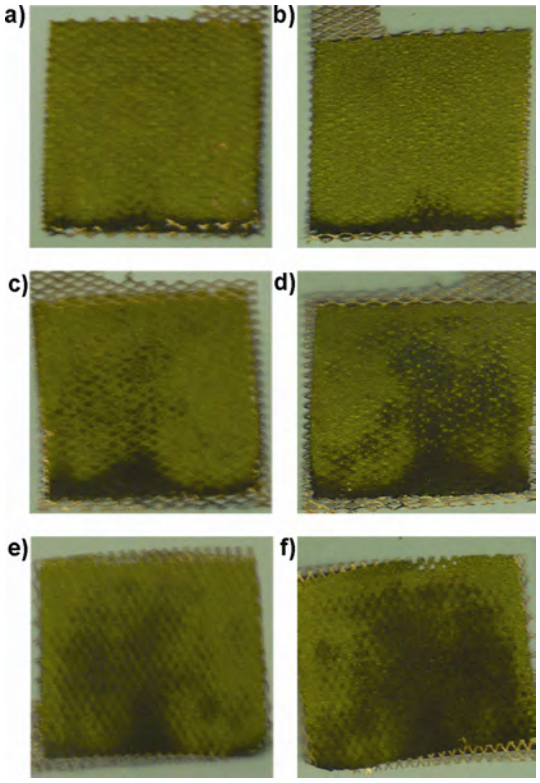

Figure 3. *(a), (c), and (e) depicting the top-side view (facing to the CE); while (b), (d), and (f) correspond to the bottom-side view of lithiated graphite WEs for WE1, WE2, and WE3, respectively.*

After the MWE cell was left for equilibration under open-circuit conditions for 15 h at 80 % SOC (~297 mAh g^{-1}), the cell was disassembled to reveal the color difference in each WEs (see Figure 3). In addition to lateral inhomogeneities as discussed elsewhere [10], the analysis of the yellowish/dark color regions provided an additional proof of the non-uniformity in the CDD between the WEs. We also observed some differences in color distribution between the top- and the bottom-side of the WEs, which confirmed that the inhomogeneities exist also perpendicular to the current collector.

In summary, we have shown here that the MWE electrochemical cell is a unique tool for the quantitative study of CDD in a Li-ion battery.

References

[1] M. Armand, J.M. Tarascon, Nature **451**, 652-657 (2008).

[2] H. Buqa, D. Goers, M. Holzapfel, M.E. Spahr, P. Novák, J. Electrochem. Soc. **152**, A474-A481 (2005).

[3] V.S. Daniel-Bekh, Zh. Fiz. Khim. SSR. **22**, 697-710 (1948).

[4] J. Euler, W. Nonnenmacher, Electrochim. Acta **2**, 268-286 (1960).

[5] J.S. Newman, C.W. Tobias, J. Electrochem. Soc. **109**, 1183-1191 (1962).

[6] R. de Levie, Electrochim. Acta **8**, 751-780 (1963).

[7] S.H. Ng, F. La Mantia, P. Novák, Angew. Chem. Int. Ed. **48**, 528-532 (2009).

[8] F. Rosciano, M. Holzapfel, H. Kaiser, W. Scheifele, P. Ruch, M. Hahn, R. Kötz, P. Novák, J. Synchrotron Rad. **14**, 487-491 (2007).

[9] http://en.wikipedia.org/wiki/Buffer_amplifier

[10] P. Maire, A. Evans, H. Kaiser, W. Scheifele, P. Novák, J. Electrochem. Soc. **155**, A862-A865 (2008).

Surface reactions of $LiMn_2O_4$ nanoparticles

T.J. Patey, M. Nakayama[1], P. Novák

phone: +41 56 310 4071, e-mail: timothy.patey@psi.ch

Reactions involving microparticles are characterized by bulk properties as << 1 % of the atoms are surface atoms. With nanoparticles, the influence of bulk properties decreases as the % of surface atoms increases. For particles 20 and 5 nm in size, 10 and 40 % of the atoms are on the surface [1], respectively, increasing the influence of surface properties. Understanding these properties could lead to innovations in useful devices like the lithium-ion battery [2]. Flame spray pyrolysis is an efficient route to produce $LiMn_2O_4$ nanoparticles for sizes between 7 nm (200 m^2g^{-1}) and 22 nm (65 m^2g^{-1}) [3]. Investigation of these powders provides insight into the influence of particle size on electrochemical surface properties. In this work, the extraction/insertion of lithium from/into the structures of $LiMn_2O_4$ powders (particle diameters of 7 nm, 13 nm, and >1 µm) are investigated.

Experimental

Flame spray pyrolysis is used to produce the $LiMn_2O_4$ nanoparticles [3]. The experimental set-up is described elsewhere [4]. Nanoparticles with sizes of 7 and 13 nm were produced, and the sizes were calculated based on X-ray diffraction and Brunauer-Emmett-Teller specific surface area measurements. The close agreement of these calculations indicates that the nanoparticles are single particles. Commercial $LiMn_2O_4$ microparticles (Sigma-Aldrich) are used for comparison. For electrochemical cycling, the $LiMn_2O_4$ powders are prepared into electrodes with mass ratios of 7:2:1 for $LiMn_2O_4$ nanoparticles : carbon black : polymer binder.

Results

Transmission electron micrograph (TEM) confirmed the size of the crystalline $LiMn_2O_4$ nanoparticles produced by flame spray pyrolysis, as seen in Figure 1 for the 7 nm sized particles.

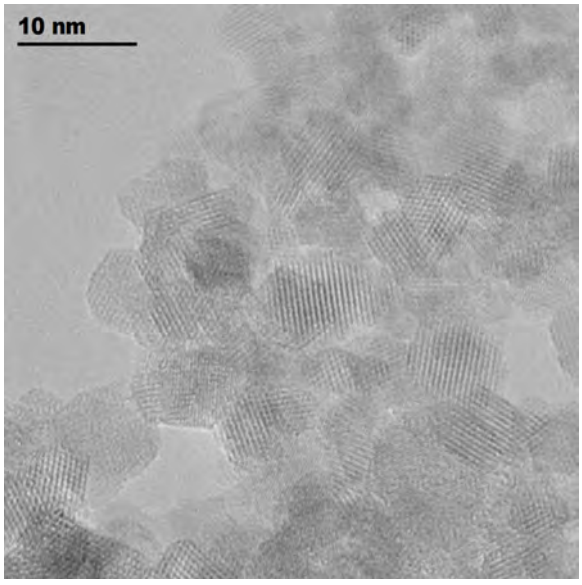

Figure 1. *TEM of FSP-produced $LiMn_2O_4$ nanoparticles.*

Cyclic voltammetry experiments were conducted at a potential scan rate of 0.1 mV s^{-1} in the range of 3.5-4.5 V vs. Li/Li^+. For the 1st charge, the potential is plotted as a function of normalized capacity (Figure 2).

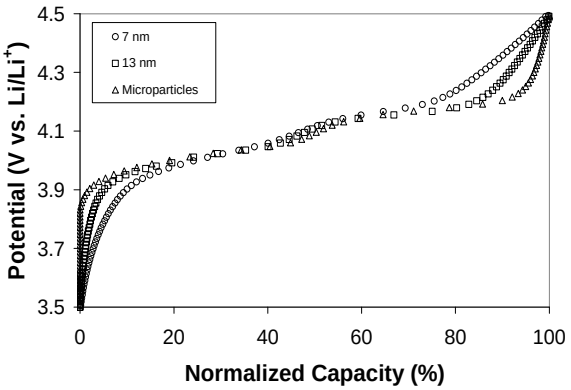

Figure 2. *Voltammetric charging (delithiation) at 0.1 mV s^{-1} of $LiMn_2O_4$ samples. Normalized capacity is the capacity expressed as a % of the total capacity.*

Charging of the electrodes from 3.5 V to 3.9 V shows that as particle size decreases, the % normalized capacity increases for this potential range. This is also seen between 4.2 and 4.5 V. Clearly, the nanoparticles are storing more charge in these low and high potential ranges. Furthermore, the 7 nm nanoparticles have a higher % normalized capacity in these potential ranges than the larger 13 nm nanoparticles. This is attributed to the proportion of extraction/insertion of lithium from/into the surface structures compared to bulk structures: it increases as nanoparticle size decreases. Lithium insertion/extraction from surface structures are known to occur at various redox potentials, as has been calculated for $LiFePO_4$, where the redox potentials for different surfaces range from 2.95 to 3.84 V, compared to the calculated potential of 3.55 V for the bulk [5]. The surface and bulk redox potentials all contribute to charge storage, but the contribution of surface redox potentials is most apparent for the 7 nm sized $LiMn_2O_4$ nanoparticles. This suggests that as the % of surface atoms increase, the role of surface redox potentials does as well.

References

[1] A. Roessler, G. Skillas, S.E. Pratsinis, Chem. unserer Zeit **35**, 32-41 (2001).

[2] A.S. Arico, P. Bruce, B. Scrosati, J. M. Tarascon, W. Van Schalkwijk, Nat. Mater. **4**, 366-377 (2005).

[3] F.O. Ernst, H.K. Kammler, A. Roessler, S.E. Pratsinis, W.J. Stark, J. Ufheil, P. Novák, Mater. Chem. Phys. **101**, 372-378 (2007).

[4] L. Madler, H.K. Kammler, R. Mueller, S.E. Pratsinis, J. Aerosol Sci. **33**, 369-389 (2002).

[5] L. Wang, F. Zhou, Y.S. Meng, G. Ceder, Phys. Rev. B **76**, art. no.-165435 (2007).

[1] Tokyo Institute of Technology, Japan

In situ small-angle X-ray scattering of carbons in supercapacitors

P. Ruch, D. Cericola, A. Menzel, R. Kötz, A. Wokaun

phone: +41 56 310 4131, e-mail: patrick.ruch@psi.ch

Activated carbons used in supercapacitors rely upon a very high inner surface area (> 1000 m^2/g) in order to maximize the amount of charge which can be stored within the electrochemical double layer. In these materials, the microporosity approaches the dimensions of the ions involved in double layer charging, resulting in a significant interest in processes occurring on the nanometer scale. Small-angle X-ray scattering (SAXS) was performed *in situ* on activated carbons in a supercapacitor electrolyte in order to study the charging mechanism in these systems.

Theory

Activated carbons can crudely be described as inhomogeneous materials consisting of two phases (solid and void space) arranged in a random fashion. The following equation can be used to describe the X-ray scattering of these materials [1, 2]:

$$I(q) = \frac{A}{q^4} + \frac{B}{\left(\frac{1}{a_1^2} + q^2\right)^2} \qquad (1)$$

where I is the scattered intensity and q is the momentum transfer. The parameter a_1 is the Debye correlation length [3], which is a measure of the mean distance between the interfaces of the two phases. The first and second terms describe the scattering from macropores (> 50 nm), which includes voids between grains, and micropores (< 2 nm), respectively. The mesoporosity of the carbon used in this work is not very pronounced and was thus not taken into account. For macropores, $1/a_1^2$ is very small compared to q^2, leading to the q^{-4} dependency. Both terms are directly proportional to the square of the difference in electron density of the two phases and to the interfacial area, i.e. $A \propto (\Delta\rho_{ma})^2 S_{ma}$ and $B \propto (\Delta\rho_{mi})^2 S_{mi}$ for macropores and micropores, respectively.

Experimental

Activated carbon (YP17, Kuraray Chemical Co.) was packed into an electrochemical cell designed for X-ray transmission measurements (Figure 1). Teflon-bound YP17 was used as the counter electrode, which was oversized by a factor of 30 with respect to the working electrode. All cell components were dried at 120°C at a pressure of 10^3 Pa for at least 24 hours. The cell assembly and electrolyte addition (1 M Et_4NBF_4 in acetonitrile (AN), Honeywell Specialty Chemicals Seelze GmbH) was carried out in an argon-filled glovebox (H_2O and O_2 contents less than 1 ppm).

The SAXS measurements were performed at the cSAXS beamline at the Swiss Light Source (SLS) using a photon energy of 17.5 keV. The sample-detector distance was 2.215 m. The Pilatus 2M detector was used for detection of the scattered X-rays, which ensured a fast read-out along with a very low background noise. Prior to each acquisition, the potential of the working electrode was held constant for at least 15 minutes using a battery tester (Astrol Electronics AG) in order to allow the charging current to drop to negligible values.

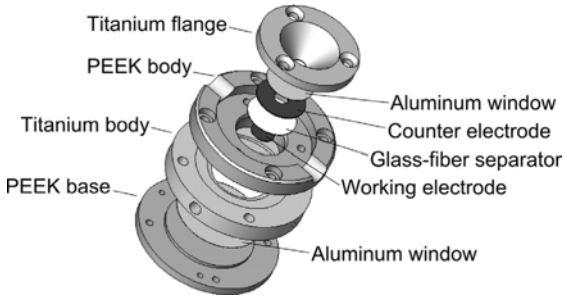

Figure 1. *Electrochemical cell for* in situ *SAXS measurements.*

Results

The separate SAXS contributions of YP17 and the electrolyte were measured in glass capillaries (Figure 2). In the range of q < 0.2 $Å^{-1}$, the scattering contribution of the electrolyte is very small compared to the scattering of the carbon. The scattered intensity of YP17 was fitted with (1) by varying A, B and a_1. The intensity plateau of the measured intensity in the range 0.08 < q < 0.2 $Å^{-1}$ arises from the microporosity of YP17 and is described well by the second term of (1). At low values of q, the first term of (1) and hence the scattering from macropores becomes dominant. In this region, the experimental intensity deviates from the fitted curve, approaching a slope of -3 in the log-log plot as q→0 in Figure 2. This can be due to "smearing effects" due to the finite size of incident X-ray beam [1] or a more complicated pore structure [4] than that assumed in Equation (1). The corresponding analysis is still ongoing and both effects are currently being considered.

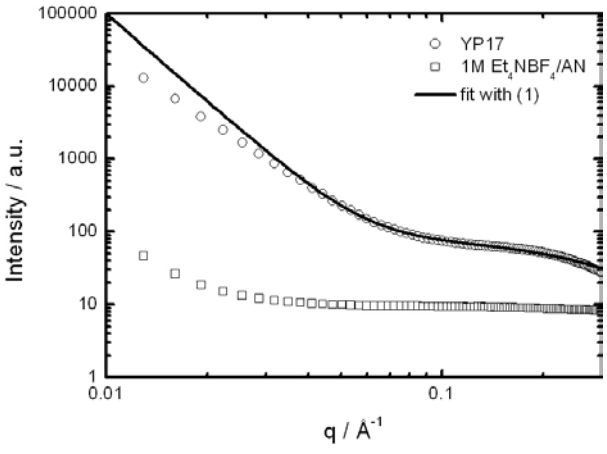

Figure 2. *SAXS intensity of YP17 and 1M Et_4NBF_4/acetonitrile.*

During negative charging of YP17, the measured SAXS pattern was found to vary as shown in Figure 3. The scattered intensity decreased most notably in the plateau region, i.e. in the region of microporosity. No significant change in the scattering curve could be observed at low q-values, i.e. in the region of macroporosity.

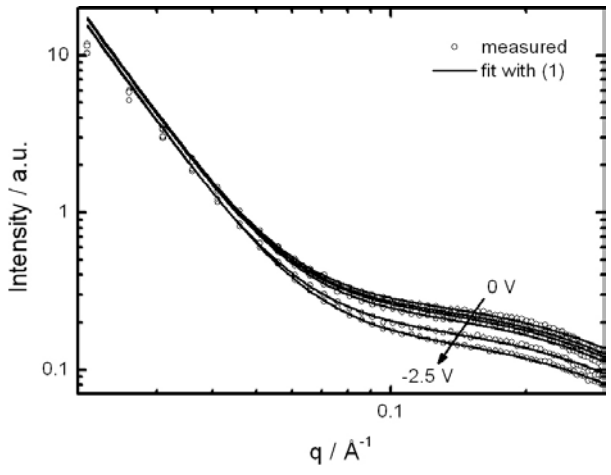

Figure 3. *In situ SAXS intensity of YP17 in 1M Et_4NBF_4/acetonitrile during negative charging in potential steps of 0.5 V. The potential of the working electrode is given against that of the counter electrode.*

The values for the parameters A, B and a_1 obtained from the fits in Figure 3 are summarized in Figure 4 as a function of cell voltage. The parameter B is three orders of magnitude larger than A, which reflects the high surface area contained within micropores. Further, B was found to decrease steadily upon negative polarization while parameter A did not change much, particularly before reaching -2 V. At -2.5 V, A and B decreased by 10% and 40% of their respective initial values.

The Debye correlation length a_1 was found to first increase upon charging, then reach a maximum value around -1 V and finally decrease again at more negative potentials. At -1 V, the increase in a_1 was nearly 4% with respect to its initial value.

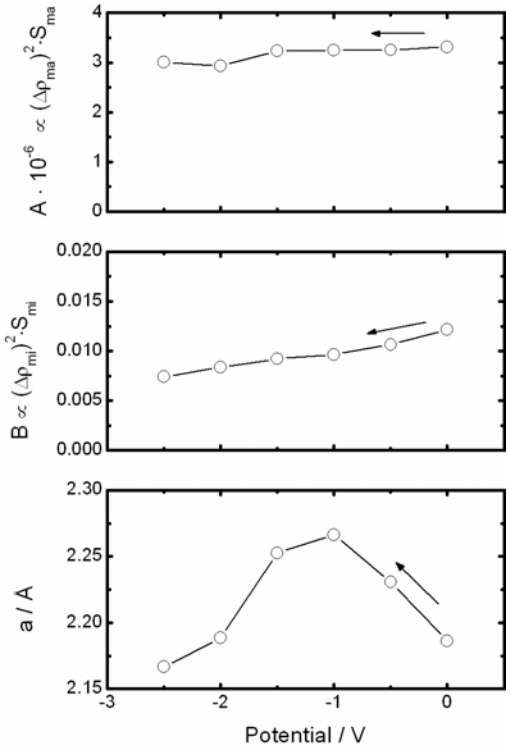

Figure 4. *Evolution of the fitting parameters of (1) during negative polarization of YP17 in 1M Et_4NBF_4/acetonitrile.*

Discussion

The simple model formalized in (1) fits the experimental SAXS data quite well. The reduction in SAXS intensity during negative polarization is most pronounced in the q-range in which micropore scattering is dominant. The decrease in B may be due to a decrease in the electron density contrast between the carbon and the electrolyte and/or a decrease in the interfacial area between the two phases within the illuminated sample volume. Since a reduction of the interfacial area by 40% appears unlikely, we propose that the change in B reflects the changes in electron density within the two phases. While negative charge is accumulated within the carbon during charging, the corresponding counter-ions are accumulated within the electrochemical double layer, thus increasing the electrolyte concentration within micropores significantly (Figure 5).

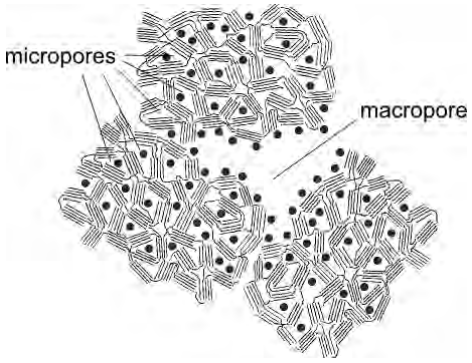

Figure 5. *Illustrative representation of negative charging of activated carbon. For clarity, only excess positive charges (dark dots) are shown.*

The non-monotonous change in the Debye correlation length a_1 with potential is not well understood at the moment. An expansion of activated carbon upon charging has been measured previously and has been attributed to the swelling of small micropores as ions are inserted into them or to the expansion of graphitic domains as ions are intercalated in between graphene sheets [5, 6]. If a_1 is a measure for the average micropore spacing, then an initial increase in a_1 could indicate micropore swelling, while the subsequent decrease in a_1 could represent pore shrinking, perhaps as ion intercalation occurs and expansion of the crystallites compresses the pores. However, further work is needed to support these hypotheses.

We conclude that *in situ* SAXS can provide valuable information about the charging mechanisms of activated carbons in supercapacitors which is not accessible by other techniques.

References

[1] A. Gibaud, J.S. Xue, J.R. Dahn, Carbon **34,** 499-503 (1996).

[2] M. Kalliat, C.Y. Kwak, P.W. Schmidt, In: New Approaches to Coal Chemistry (Ed. B.D. Blaustein et al.), American Chemical Society, Washington, DC (1981).

[3] P. Debye, H.R. Anderson, H. Brumberger, Journal of Applied Physics **28,** 679-683 (1957)

[4] B. Smarsly, M. Antonietti, T. Wolff, Journal of Chemical Physics **116,** 2618-2627 (2002).

[5] M. Hahn, O. Barbieri, F.P. Campana, R. Kötz, R. Gallay, Applied Physics A **82,** 633-638 (2006).

[6] P.W. Ruch, R. Kötz, M. Hahn, A. Wokaun, in preparation.

Effective transport parameters of a PEFC catalyst layer

R. Flückiger, P.C. Sui[1], N. Djilali[1], A. Wokaun, F.N. Büchi

phone: +41 56 310 4189, e-mail: reto.flueckiger@psi.ch

In the cathode catalyst layer (CL) of a polymer electrolyte fuel cell (PEFC) coupled transport of electrons, protons, gases, liquid water and heat takes place on the smallest length scale. Every species has its own tortuous pathway to and from the reaction zone resulting in different transport resistances. Structural effective parameters are difficult to measure experimentally. However, especially on the channel-rib scale of a few millimeters these parameters can have a distinct influence on the current density distribution. Therefore a mesocopic catalyst pore scale model was developed in order to bridge the gap between a microcsopic (nm-scale) and macroscopic (µm-scale) model. The resulting physical parameters are dependent on each other and confine the large range of values used in literature. A more detailed introduction to the model can be found in [1].

Modelling

The model has two parts and is realized in Fortran. First the structure of the CL is generated using the carbon sphere radius r_C, the number of carbon spheres per repetitive unit n and the ionomer coating thickness δ_i as input parameters. The carbon structure is generated on an N^3 grid by random distribution of the sphere centers and subsequent labeling of the ionomer layer grid points.

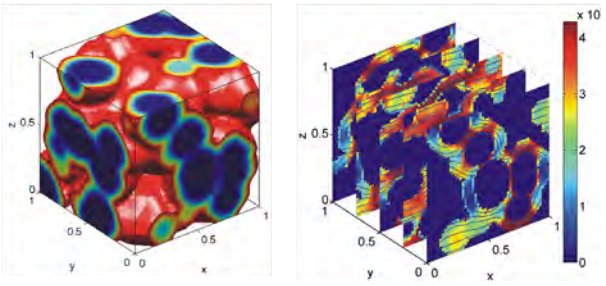

Figure 1. *Left: repetitive unit (100 nm side length) of a catalyst structure. Blue: carbon particles. Red: ionomer coating. Right: dimensionless proton flux distribution in x-direction.*

In the second part the uncoupled Laplace equation $\Delta\phi=0$ is solved for either the oxygen concentration, the H^+ potential or the e^- potential. The discretization of the differential equation is based on the control volume formulation [2]. The resulting system of algebraic equations is solved using the generalized minimal residual solver (GMRES). The extraction of the effective transport parameters was done with dimensionless simulations. Therefore the resulting flux is a direct measure of the effective relative transport parameter ε/τ.

Results and Discussion

Figure 2 shows the effective relative transport parameters as a function of carbon sphere radius. In the same plot the corresponding void ε_v, ionomer ε_i and solid fractions ε_s are shown as gray areas summing up to 1. The solid fraction and the effective electric conductivity increase by increasing the carbon particle radius.

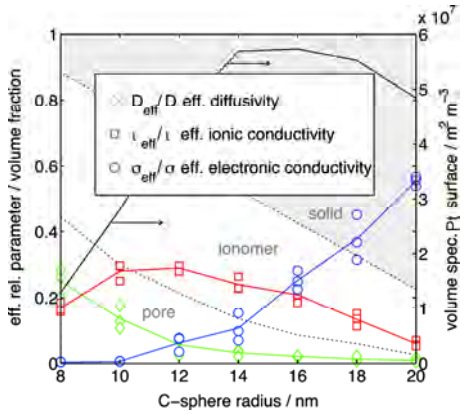

Figure 2. *Effective relative transport parameters, volume fractions and volume specific Pt surface as a function of carbon particle radius. n = 64, δ_i = 10 nm, d_{cl} = 10 mm.*

However, a good electric conductivity can not be achieved without impeding the effective diffusivity. The latter was considered less critical as oxygen dissolves into the ionomer and diffuses to the reaction sites. The effective electric conductivity instead is critical and shows a percolation effect below a radius of 10 nm where no continuous path for electrons is present. The volume specific active surface can be derived by assuming a homogenous Pt coating of the carbon spheres. The maximum is observed due to an increased overlapping of the carbon spheres at large radius. The mean values are approximately an order of magnitude higher compared to literature (Table 1). However it is expected that not the entire surface is available for reaction and an effective Pt surface ratio needs to be introduced.

parameter	modeled value	literature
ε_V	0.3	0.1 [3], 0.35
ε_V	0.49	0.25, 0.5 [3]
A [M^2/M^3]	2.8E7	3.6E5 [3] 1.1E7
D_{eff}/D	0.13	$\varepsilon_V^{1.5}$
ι_{eff}/ι	0.27	0.19 [4], 0.27 [5]
σ_{eff}/σ	0.005	0.075, 0.14 [4] 0.004 [5]

Table 1*. Parameters (r_c=10nm, n=64, d_i=10nm, d_{cl}=10mm).*

References

[1] P. Sui, J. Hu, N. Djilali, Proceedings of AIChE Annual Meeting, (2007).

[2] S. V. Patankar, Numerical Heat Transfer and Fluid Flow, Taylor and Francis, (1980).

[3] W. Sun, B. A. Peppley, K. Karan, Electrochim.. Acta, **50,** 3359 (2005).

[4] M. Secanell, K. Karan, A. Suleman, N. Djilali, Electrochim. Acta, 6318, **52** (2007).

[5] K. Karan, Electrochem. Commun. **9,** 747 (2007).

[1] University of Victoria BC, Canada

A novel preparation chamber for *quasi in situ* XPS measurements of electrochemically treated electrodes

A. Foelske, M. Hahn[1], H. Kaiser, R. Kötz, C. Marmy, P.W. Ruch, B. Schnyder[2]

phone: +41 56 310 4193, e-mail: annette.foelske@psi.ch

As electrochemical reactions occur at the electrode electrolyte interface and X-ray photoelectron spectroscopy (XPS) is a powerful tool for surface analysis, XPS surface analysis is of utmost importance for several projects of the Electrochemistry Laboratory at the Paul Scherrer Institut (PSI). XPS analysis of the samples, however, has one big disadvantage, namely, surface contamination and oxidation in air during transfer of the electrochemically treated electrode into the ultra high vacuum (UHV). In order to avoid contamination and to follow the electrochemical processes, such as deposition, adsorption, corrosion, intercalation, oxidation or reduction under *quasi in situ* conditions an "electrochemical preparation chamber" directly attached to the UHV system has been set up. This extension allows preparing electrodes electrochemically at atmospheric pressure under inert nitrogen atmosphere with subsequent sample transfer into the UHV for surface analysis without air exposure.

Setup

The setup of the "electrochemical preparation chamber" is outlined in figures 1 and 2. The full extension is composed of two chambers which are i) the transfer chamber (figure 1; 2) directly attached to the distribution chamber of the UHV system (figure 1; 1) and ii) the preparation chamber in which electrochemical preparation is performed (figure 1; 3).

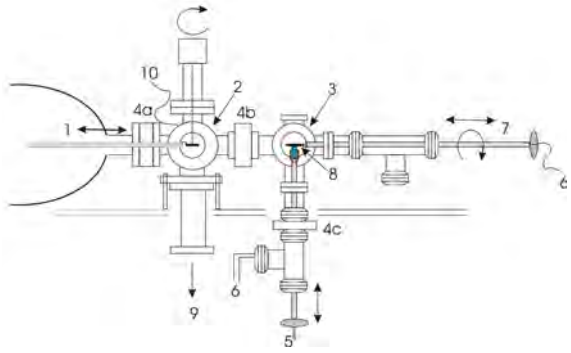

Figure 1. *1) distribution chamber; 2) transfer chamber; 3) electrochemical preparation chamber; 4) gate valves; 5) pipes for liquids; 6) connections to counter, reference and working electrode; 7) manipulator; 8) working electrode; 9) turbo pump; 10) pressure control*

For electrochemical preparation the samples mounted on the standard sample holder made from stainless steel are inserted into the UHV via the fast entry air lock (FEAL) and can be sputter cleaned by argon ion etching in the analyzer chamber of the UHV system. Subsequently, the sample is transferred through the distribution chamber (figure 1; 1) into the transfer chamber (figure 1; 2) which is pumped by a turbo pump reaching pressures of $1*10^{-8}$ mbar. After transfer and rotation of the sample holder horizontally by 180° the gate valve 4a is closed and the valve 4b is opened so that the transfer and preparation chambers are flooded by nitrogen until the atmospheric pressure is reached. The sample is transferred with the manipulator (7) into the preparation chamber (4) and vertically rotated by 180° reaching its position for electrochemical preparation. The reaction vessel (E-Cell, figure 2a; 2) mounted on a hollow rod comes from the bottom after opening the gate valve 4c. The feedthrough for approaching the E-Cell was designed by the vacuum group at PSI and allows movement of the rod while it is tight enough to maintain its position when the E-Cell reaches the position for preparation, namely right under the sample i.e. working electrode (WE). The E-Cell contains a reference (RE) and a counter electrode (CE) as well as pipes for feeding and exhausting liquids. Electric feedthroughs provide connections of the RE and the CE to a potentiostat (Versastat) for potential control. A cap on top of the vessel allows restricting the contact with the electrolyte to a defined area of the WE. Filling of the E-Cell with electrolyte is done using syringes mounted at the outlet of the pipes (figure 2a; 5).

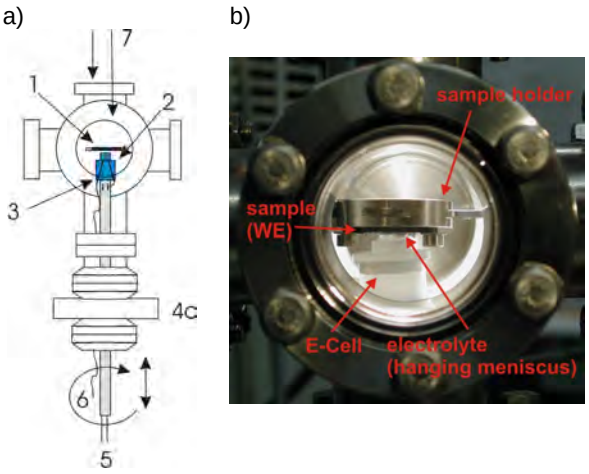

Figure 2. a) *1) sample; 2) electrochemical cell; 3) feed through and electric connections to WE and CE; 4c) gate valve; 5) pipes for liquids; 6) electric connections of WE and CE; 7) windows;* ***b)*** *photograph of HOPG during electrochemical preparation showing the hanging meniscus geometry.*

Surface tension is utilized to form a droplet between the cap and the sample. After contacting the WE with the electrolyte, electrochemical preparation can be performed utilizing a hanging meniscus geometry throughout the experiment (figure 2b). After the preparation, the electrolyte is exhausted and the electrode can be rinsed with a solvent. The sample is then relocated back to the transfer chamber, the valve 4b is closed, and the chamber is pumped down to appropriate pressure for the transfer into the analyzer chamber and subsequent surface analysis. The setup has been tested in both, aqueous and, what is even more interesting, non-aqueous electrolyte which to the best of our knowledge has not yet been reported in literature.

[1] Honeywel Specialty Chemicals Seelze GmbH, Seelze, DE
[2] Photolito, Microcrystal, Grenchen

Testing the Setup

For testing the setup in aqueous solution cyclic voltammetry (CV) has been performed on platinum electrodes in nitrogen saturated 0.1 M H_2SO_4 solution. The WE was a platinum film sputtered on indium tin oxide (ITO) covered glass. The RE and the CE were platinum wires (diameter: 1mm).

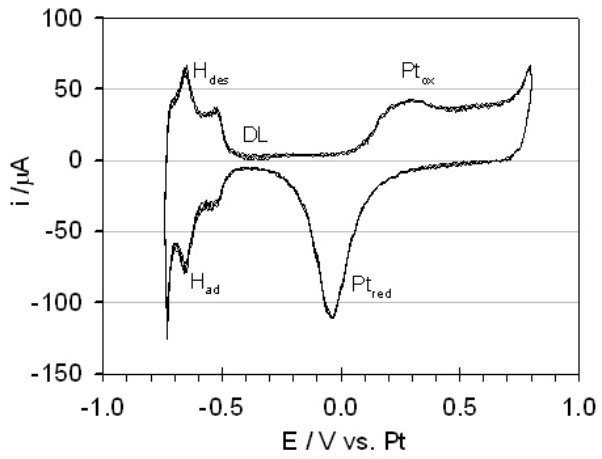

Figure 3. *CV of Pt on ITO in 0.1 M H_2SO_4; dE/dt = 50mV/s.*

The platinum CVs recorded using this setup show all textbook features typical for this system (figure 3). In the potential range of hydrogen adsorption (-0.75 V < E < -0.5 V) three peaks occur indicating hydrogen adsorption reaction on different oriented crystal planes of the platinum film. This area is followed by a double layer region (DL) with subsequent oxidation of platinum starting at 0.03 V and corresponding reduction current at -0.03 V vs. Pt RE. The measured CV verifies the cleanliness of the setup.

For electrochemical measurements in non-aqueous electrolyte, CVs of freshly cleaved highly oriented pyrolythic graphite (HOPG) in 1M tetraethylammonium tetrafluoroborate ($TEABF_4$) dissolved in propylene carbonate (PC) have been recorded. The RE and the CE were activated carbon electrodes (YP17) connected to titanium wires (diameter: 1mm).

An HOPG sample has been polarized at an intercalation potential of 1.8 V vs. YP17 for 5 minutes. After intercalation the electrode has been rinsed with PC, transferred back to the UHV, and, subsequently, analyzed with XPS using the monochromatic Al Kα X-ray source of the VG ESCALB 220iXL spectrometer for excitation. Prior to electrochemical treatment the E-Cell was cleaned by rinsing it several times with electrolyte solution.

The recorded CVs of HOPG in $TEABF_4$/PC (figure 4) are in good agreement with our previous findings [1]. In the positive potential range (1.7 V < E < 2.0 V) electrochemically induced intercalation and de-intercalation of BF_4^- ions occur whereas in the negative potential range (-1.0 V > E > -2.5 V) similar reactions are recorded for the TEA^+ ions. The fact that a potential window of ΔE = 4.5 V was stable over a time range of > 4 h proves that the setup allows for electrochemical preparation in non-aqueous electrolyte in the absence of oxygen and water.

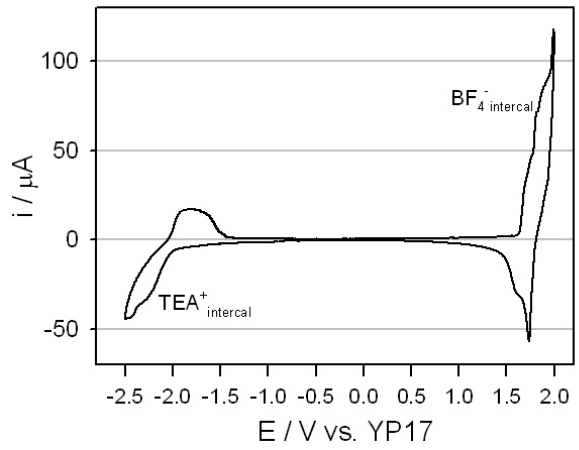

Figure 4. *CV of HOPG in 1.0 M TEABF4/PC; dE/dt = 20mV/s.*

XP-spectra of the B 1s and F 1s signals after intercalation of the anions at 1.8 V vs. YP17 for 5 min show negative shifts in binding energy (BE) of 2.0 eV in comparison to the spectra obtained from measurements of the $TEABF_4$ salt (figure 5).

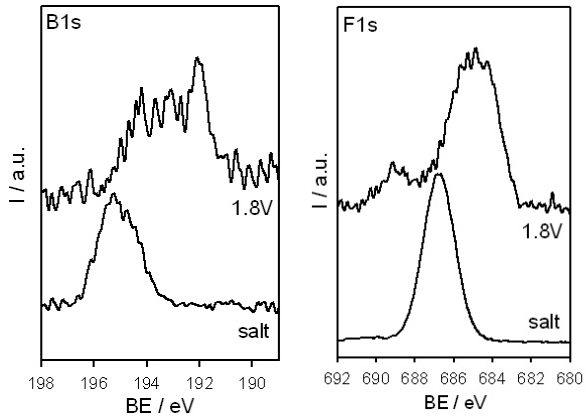

Figure 5. *B 1s and C 1s XP-spectra of $TEABF_4$ (bottom), and HOPG polarized at 1.8 V vs. YP17 in 1.0 M TEABF4/PC for 5 min (top).*

These shifts are in agreement with our previous findings of XPS measurements of electrochemically intercalated HOPG in aqueous [2] and in non-aqueous solution [3] and can be explained by a shift of the Fermi level of the intercalated layers.

Acknowledgement

Extensive support from the vacuum group of PSI is gratefully acknowledged.

References

[1] P.W. Ruch, M. Hahn, F. Rosciano, M. Holzapfel, H. Kaiser, W. Scheifele, B. Schmitt, P. Novak, R. Kötz, A. Wokaun, Electrochim. Acta **53,** 1074-1082 (2007).

[2] B. Schnyder, D. Alliata, R. Kötz, H. Siegenthaler, Appl. Surf. Sci. **173**, 221-232 (2001)..

[3] A. Foelske, P. Ruch, R.Kötz, PSI Electrochemistry Labaratory – Annual Report 2007, 52, ISSN No. 1661-5379 (2008).

Photon-assisted catalytic activation of methane over supported catalysts using a xenon excimer lamp

F. Loviat, J. Wambach, I. Czekaj, A. Wokaun

phone: +41 56 310 4266, e-mail: joerg.wambach@psi.ch

Photon-assisted catalytic reactions making use of lasers represent an interesting strategy to activate methane and to convert it into oxygenated compounds or higher hydrocarbons. The use of lasers for industrial applications, however, is disadvantageous, because of their high costs, low photon efficiency and small illuminated area. The aim of our work was to investigate the effect of photons from a Xe excimer lamp (λ: 172 nm = 7.2 eV) towards the activation of methane over mono- and bi-metallic Ni-Pd/γ-Al_2O_3/Si model catalysts.

Experimental

The construction of a miniature, UHV-compatible excimer lamp was a pre-requisite for the project and is described elsewhere [1]. Tested with respect to reactivity were the pure Ni, pure Pd, and the systems given in Table 1. The catalysts were exposed to 100% CH_4, respectively to 95% CH_4 - 5% O_2. The surface composition of the different catalysts was evaluated based on AES (Auger Electron Spectroscopy), XPS (X-ray Photoelectron Spectroscopy) and TPR (Thermal Programmed Reaction) measurements. The carbon surface uptake during TPR experiments (ramping the temperature of the catalyst up to 773 K with 20 K/min) was measured for each model catalyst, with and without VUV irradiation, referred as “bright” and “dark”. The amount of carbon formed during the reactions was considered as a catalyst reactivity indicator.

	0.8Ni/0.2Pd	**0.5Ni/0.5Pd**	**0.2Ni/0.8Pd**
1st metal: **Ni**	0.8 ML	0.5 ML	0.2 ML
2nd metal: Pd	0.2 ML	0.5 ML	0.8 ML
	0.8Pd/0.2Ni	**0.5Pd/0.5Ni**	**0.2Pd/0.8Ni**
1st metal: **Pd**	0.8 ML	0.5 ML	0.2 ML
2nd metal: Ni	0.2 ML	0.5 ML	0.8 ML

Table 1. *Description of the bi-metallic catalysts tested.*

Results

The various catalysts exhibit clearly different reactivities. In the case of pure CH_4 (Figure 1), the final surface carbon concentration appears always to be higher in the bright experiments. Moreover for the bimetallic catalysts, the difference of carbon concentration between bright and dark experiments seems to increase with the nickel content. This suggests a photon-assisted catalytic methane activation, which is remarkable, as the emission of the xenon excimer lamp is centred at 172nm, while CH_4 in the gas phase does not absorb above 140nm.

It was observed also that each pair of bi-metallic catalysts characterized by the same average composition (see Table 1) exhibit a comparable reactivity, which seemed not to depend on which metal was deposited first on the substrate. A possible reason for this behaviour might be that an almost identical surface composition for each pair of bimetallic catalysts with the same average composition was found always. In addition, AES measurements suggested a palladium surface enrichment of the metal clusters present on the different catalysts. This phenomenon is in agreement with literature data [2].

In the case of 95% CH_4 - 5% O_2 (Figure 2), contrary to what was observed with 100% CH_4, the concentration of carbon on the surface appeared to be significantly lower in the bright experiments. This could be explained by the formation of ozone or other oxygen radicals from the splitting of oxygen molecules by the VUV photons, which can then oxidize the carbon formed on the catalyst surface, leading to a desorption of CO and/or CO_2.

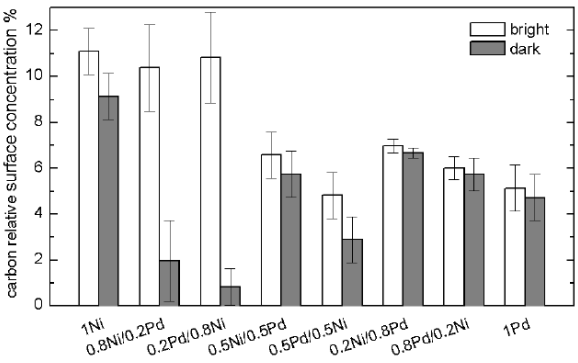

Figure 1. *Relative carbon concentration determined by XPS after TPR experiments with 100% CH_4 on various catalysts.*

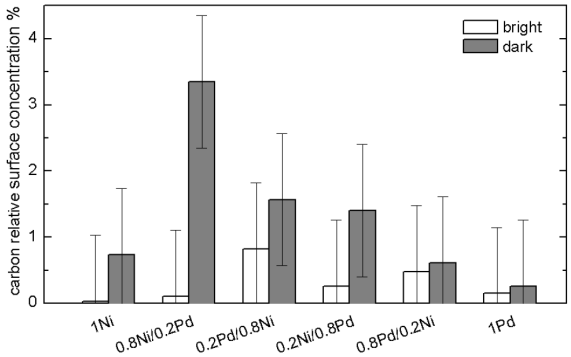

Figure 2. *Relative carbon concentration determined by XPS after TPR experiments with 95% CH_4 - 5% O_2 on various catalysts.*

For all bi-metallic catalysts, nickel was partly oxidized to what seems to be $Ni(OH)_2$. It was observed that pure nickel was completely oxidized in the bright experiment while it remained metallic in the dark experiment. No significant difference of oxidation level could be observed in the bi-metallic catalysts between bright and dark experiments. This fact supports the suggestion that the final catalyst structure does not depend on the deposition sequence of nickel and palladium. The addition of palladium seems to form a palladium rich shell over the metal clusters protecting the catalyst against total oxidation.

References

[1] F. Loviat, S. Stutz, M. Isler, U. Kogelschatz, T. Jung, T. Lippert, J. Wambach, R. Kötz, A. Wokaun, PSI Electrochemistry Laboratory – Annual Report 2007, 54, ISSN No. 1661-5379 (2008).

[2] A. de Siervo et.al., J. Mol. Catal. A: Chem. **281**, 3 (2008).

Extreme ultraviolet interference lithography for production of platinum nanoparticles on glassy carbon

A. Savouchkina, A. Foelske-Schmitz, R. Kötz, G.G. Scherer, A. Wokaun, C. Padeste, V. Auzelyte, H. Solak

phone: +41 56 310 5532, e-mail: anastasia.savouchkina@psi.ch

The lifetime of polymer electrolyte fuel cells (PEFC) is greatly limited by the degradation of their catalyst and/or its support. Therefore, monitoring electrochemically induced corrosion or Ostwald ripening using surface-sensitive techniques such as *in situ* scanning probe microscopy (SPM), scanning electron microscopy (SEM) or X-ray photoelectron spectroscopy (XPS) is of utmost importance. In order to correlate these processes to the size of platinum (Pt) nanoparticles model electrodes consisting of Pt nanoparticles of various but defined sizes on a flat carbon support have to be designed. Central issues of the design, which have to be addressed, are producing nanoparticles with a desired size and position and afterwards preventing them from self-diffusion and agglomeration. The approach presented here is based on extreme ultraviolet (EUV) interference lithography on modified glassy carbon supports. It allows producing carbon electrodes covered with Pt nanoparticles, which form a regular pattern. EUV lithography was performed at the X-ray interference lithography (XIL) beamline of Swiss Light Source (SLS) and followed by sputtering of a thin platinum layer and a subsequent lift-off process (see Figure 1).

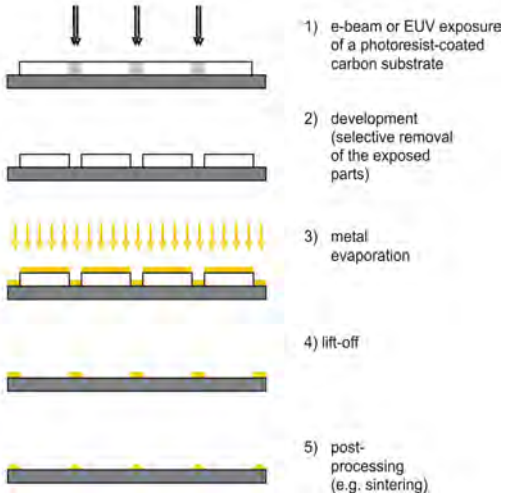

Figure 1. *Lithographic preparation of metal nanoparticle arrays on carbon substrates [1].*

Experimental

The 15x15 mm glassy carbon (GC) substrates were first heated in air for 0, 10, 20 and 30 minutes at 450°C and afterwards spin-coated with a 65 nm thick poly(methyl methacrylate) (PMMA) photoresist film. Sample exposure with 92 eV EUV radiation was performed at the XIL beamline according to the methods described by Solak et al. [1]. Silicon nitride masks with gratings of various periods were used to create interference patterns with periodicity in the range of 141 to 1410 nm. On each sample, nine fields were exposed using EUV doses of 25-107.5 mJ/cm^2. The exposed samples were developed using a mixture of 1:3 of isopropanol and chlorobenzene as a selective solvent.

Deposition of a 10 nm Pt layer was performed with a DC magnetron-sputtering device TIPSI with an Ar pressure of 10^{-3} mbar and a power of 30 W.

After Pt deposition the lift-off process was accomplished by soaking the GC samples overnight in acetone and ultrasonicating them for five minutes in acetone the following day.

Results

The possibility of producing micro- and nanostructured Pt model electrodes via EUV interference lithography has been successfully tested. In order to find optimized conditions for the lithographic process upon each spincoated GC sample 9 fields were generated, field 1 having the lowest EUV dose of 25 mJ/cm^2 and field 9 the highest (107.5 mJ/cm^2). On each field the pattern shown in Figure 2 was generated: The micro- and nanostructures comprised either holes (fields 1 and 3 in Figure 2) created by four-beam or lines (fields 2, 4 and 5 in Figure 2) created by two-beam X-ray interference.

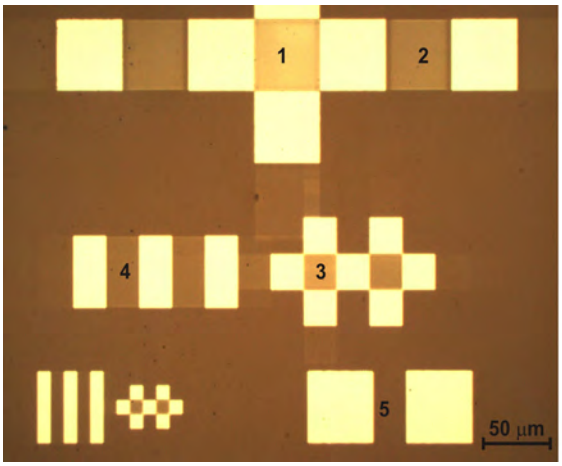

Figure 2. *A light microscope image of a field with various structures created in one exposure. The fields of interest are indicated as following 1) 141 nm holes; 2) 100 nm lines; 3) 283 nm holes; 4) 200 nm lines; 5) 1000 nm lines.*

On the patterned GC sample heated for 20 minutes at 450°C 10 nm Pt were deposited. This pre-treatment was chosen to open the pores within the material as described by A. Braun et al. [2]. The opened pores are supposed to improve the adhesion of platinum to the carbon support and, thus, prevent it from falling off during the lift-off procedure. Each of the nine fields irradiated with a different EUV dose was investigated via SEM. High magnification images of the holes in the 141 nm period structures (field 1 in Figure 2) reveal that the hole shape and the degree to which the holes are “open” depends on the EUV dose (see Figure 3). Increasing this dose enhances the definition of the structures (compare dose 36 mJ/cm^2 Figure 3 a) and dose 107.5 mJ/cm^2 Figure 3 f)).

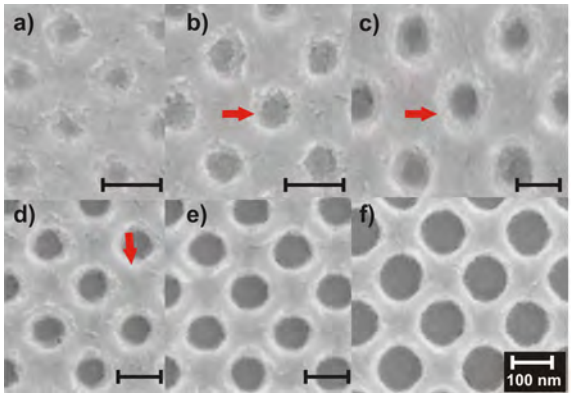

Figure 3. *SEM images of 141 nm period hole structures on GC with EUV dose of a) 43.2 mJ/cm^2; b) 51.8 mJ/cm^2 ; c) 62.2 mJ/cm^2 ; d) 74.6 mJ/cm^2 ; e) 89.6 mJ/cm^2; f) 107.5 mJ/cm^2 before lift-off.*

The diameter of the formed nano-holes also depends on the EUV dose, and is barely 50 nm for 43.2 mJ/cm^2 and 97 nm for 107.5 mJ/cm^2 (see Figure 4). This observation indicates that preparation of structures using interference lithography allows for tuning the size of the platinum nanoparticles on glassy carbon support to a certain extent by varying the exposure dose.

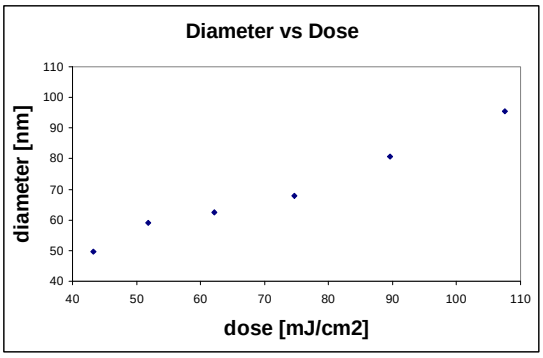

Figure 4. *Dependence of the holes' diameter upon EUV dose.*

Apart from a smaller diameter, the nanostructures with lower EUV dose also show so-called "skirts" around the holes (indicated by arrows in Figure 3). These "skirts" can hamper the lift-off process, because they induce the formation of a continuous Pt film covering the photoresist as well as the GC surface. Thus, either the lift-off process is expected to be incomplete or too much Pt is removed.

After the lift-off, the sample was investigated once again with SEM. The success of the lift-off procedure was dependent on the EUV dose of the investigated field. The 141 nm structures on the fields with lowest EUV dose were completely removed by the process (d < 62.2mJ/cm^2), while for the fields with higher EUV dose the procedure was successful.
The best result has been achieved for the dose of 89.6 mJ/cm^2 (Figure 5): Dark parts of the image represent the photoresist-free GC where only carbon support is left, the bright, almost white area is the photoresist covered with Pt and the gray area displays a successful lift-off. The gray area covers ca 80 % of the exposed field proving that most of the structures withstood the lift-off process under the chosen preparation conditions. Some of the "skirts" remained (Figure 6), which shows that although the lift-off procedure was quite successful, it can still be improved by modifying the ultrasonication time or depositing a thinner Pt layer after EUV exposure.

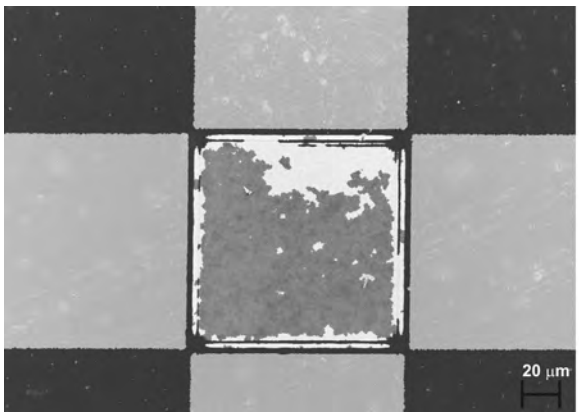

Figure 5. *An SEM image of the field with 141 nm period hole structures on GC with EUV dose of 89.6 mJ/cm^2 after lift-off.*

The lift-off process on fields with lower EUV dose, however, almost completely destroyed the structures except for few exceptions (gray dots in Figure 6 a)). The evaluation of the diameter of the remaining dots has shown that after lift-off their diameter has increased in comparison to the holes and measures 62 nm for the dose of 62.2 mJ/cm^2 to 100 nm for 107.5 mJ/cm^2.

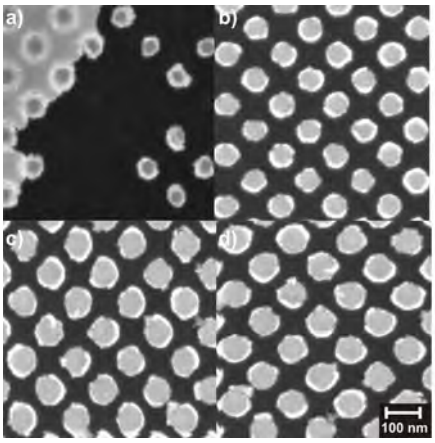

Figure 6. *An SEM image of 100nm dots on GC with EUV dose of a) 62.2 mJ/cm^2 ; b) 74.6 mJ/cm^2 ; c) 89.6 mJ/cm^2; d) 107.5 mJ/cm^2 after lift-off.*

We have successfully generated arrays of Pt nanoparticles with a diameter of 100 nm which will serve as model electrodes for the electrochemical investigation of carbon supported Pt catalyst. The promising process parameters will be further investigated and improved to produce even smaller structures.

The authors would like to thank Swiss National Foundation for financing the project 200021_121719/1. Help and support of K. Vogelsang, S. Neuhaus and M. Horisberger are gratefully acknowledged.

References

[1] H. H. Solak, C. David, J. Gobrecht, V. Golovkina, F. Cerrina, S. O. Kim, P. F. Nealey, Microelectron. Eng. **67-68**, 56-62 (2003).

[2] A. Braun, M. Bärtsch, B. Schneider, R. Kötz, O. Haas, H. G. Haubold, G. Goerigk, J. Non-Cryst. Solids **260**, 1-14 (1999).

High mass activity of $PtCo_3$ nanoparticles for the oxygen reduction reaction

H. Schulenburg, G. Khelashvili[1], E. Müller[2], T. Roser, H. Bönnemann[1], A. Wokaun, G.G. Scherer

phone: +41 56 310 2125, e-mail: hendrik.schulenburg@psi.ch

Polymer electrolyte fuel cells (PEFCs) are widely developed as clean power sources for electric cars, consumer electronics, domestic power plants, and other applications. A broad market penetration of PEFCs is mainly hindered by the high cost and moderate stability of several PEFC components, as well as by the missing hydrogen infrastructure. The PEFC shows an efficiency advantage over the internal combustion engine; however, the thermodynamic efficiency of 83% for a hydrogen/oxygen PEFC is by far not achieved, mainly due to losses at the fuel cell cathode, where the oxygen reduction reaction (orr) is taking place (1).

$$O_2 + 4H^+ + 4e^- \rightarrow 2H_2O \qquad \text{(eq.1)}$$

For this reaction, carbon supported platinum nanoparticles (Pt/C) are usually used as catalysts. They suffer from a high overpotential (>0.3V) for the orr, high cost and catalyst degradation. A consensus becomes apparent that at fuel cell relevant potentials adsorbed oxygen blocks active sites of the Pt surface and therefore limits the catalytic activity [1]. Appropriate alloying of Pt with Fe, Ni or Co seems to facilitate the desorption of oxygen species and leads to higher surface site availability and higher catalytic activity. Commercial $PtCo_x$/C catalysts already show mass activities, which are about twice as high as Pt/C. $PtCo_x$/C catalysts also seem to be more stable towards sintering than Pt/C, especially under varying load conditions [2]. In this work, we prepared $PtCo_3$/C catalysts and characterized their catalytic and structural properties, aiming for a better understanding of the improved activity of base-metal rich Pt-alloy nanoparticles.

Experimental

Cobalt nanoparticles are prepared by thermolysis of $Co_2(CO)_8$ in the presence of tetraoctylaluminum as detergent. The Co nanoparticles were supported by carbon black (Vulcan XC72) and the detergent was removed. Dimethyl(1,5-cyclooctadiene)platinum(II) (Me_2PtCOD) was added and reduced by hydrogen afterwards. The obtained catalyst precursors were heated under reductive conditions. Finally, excessive Co was leached by cyclic voltammetry. The catalytic activity for oxygen reduction was investigated by thin-film rotating disc electrode measurements [3].

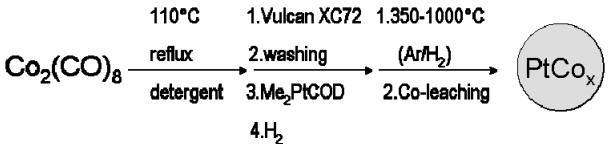

Figure 1. *Synthesis of carbon supported $PtCo_x$ nanoparticles.*

Results and Discussion

Transmission electron microscopy (HRTEM)

Heat treatment in the temperature range of 350 to 1000°C, does not lead to a significant particle growth until 600°C. At higher temperatures the particle size increases clearly and reaches a maximum of (7.8±5.4)nm for the catalyst tempered at 1000°C. EDX measurements of single catalyst particles show that before heat treatment separated Co and Pt nanoparticles are present. After treatment at 800°C both, Pt and Co, are detected in single nanoparticles.

Temperature/[°C]	350	600	800	1000
Particle size/[nm]	4.7±2.0	4.7±3.0	6.3±4.9	7.8±5.4

Table1. *HRTEM-particle size of heat-treated $PtCo_3$/C catalysts*

Electrochemical activation

All $PtCo_x$/C catalysts were activated by cyclic voltammetry. The catalyst covered electrodes were inserted into the electrolyte at a potential of 0.05V before they were cycled 25 times in the potential range between 0.05 and 1.2V. During the first cycles heat-treated catalysts (T = 600 to 1000°C) show a strong oxidation peak in the potential range between 1.0 and 1.2V, which is decreasing with the number of cycles. The CV of $PtCo_x$/C-800°C is displayed in Figure 1. After 25 cycles, peak positions and intensities do not change significantly. The ratio of the total anodic and cathodic charge is then very close to unity (inset figure 1).

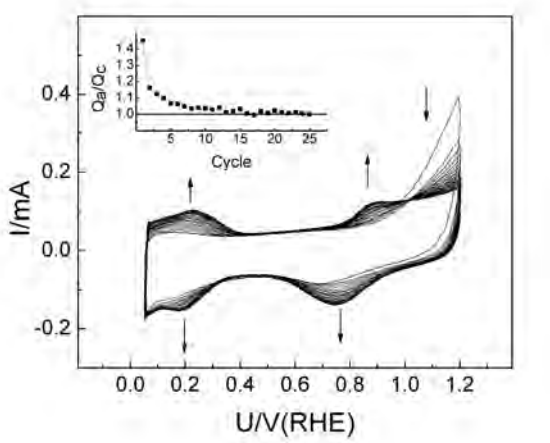

Figure 2. *Cyclic voltammogram of $PtCo_3$/C heat-treated at 800°C. Platin loading 12.7µg/cm², v=100mV/s, Ar-saturated 0.1M $HClO_4$, 20°C. Inset: ratio of total anodic and cathodic charge during cycling.*

Catalytic activity for oxygen reduction

After activation by cyclic voltammetry, the catalytic activity for oxygen reduction was determined with rotating disc electrode (RDE) measurements (Fig. 3b). The catalytic mass activity at 0.9V of the $PtCo_x$/C as-prepared catalyst is comparable to a Pt/C catalyst and about 50% lower than the commercial $PtCo_x$/C catalyst. The mass activity increases with the heat-treatment temperature and reaches a maximum at 800°C. Mass transport corrected activities of 0.56A/mg_{Pt} were reached at 0.9 V (RHE) and room temperature. According to our knowledge, these are the highest activities that have been reported for binary $PtCo_x$/C catalysts. This catalyst

[1] FZK Eggenstein-Leopoldshafen, Germany
[2] ETH Zürich

reaches the activity goal for 2010 of the US Department of Energy (DOE). Higher temperatures of 900 and 1000°C lead to performance loss.

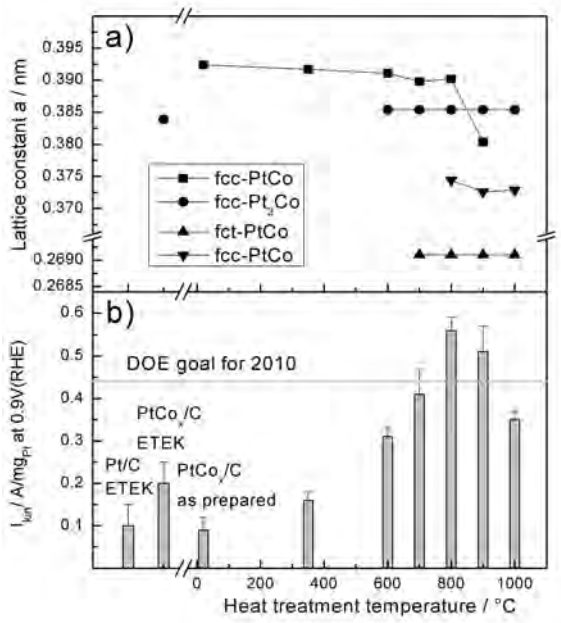

Figure 3. *Structure-activity correlation for $PtCo_x$/C catalysts; a) Presence and lattice constants of crystalline phases in $PtCo_x$/C catalysts determined by deconvolution of powder diffractograms; .b) mass activity for oxygen reduction at 0.9V (RHE) of $PtCo_x$/C catalysts calculated from RDE measurements; O_2-saturated 0.1M $HClO_4$, v=5mV/s, 1600rpm, anodic going sweeps from 0 to 1.2V, 20°C, currents were mass transport corrected using the Levich-Koutecky-Equation.*

X-ray diffractometry

Diffractograms of the as-prepared and heat-treated $PtCo_3$/C can be deconvoluted with 5 phases, namely fcc-Pt (03-065-2868), Pt_3Co (00-029-0499), fct-PtCo (01-071-7406), fcc-PtCo (03-065-8970) and Co (00-015-0806). The XRD results show that the investigated $PtCo_3$/C catalysts consist of several phases or components, which all probably have different catalytic activities. For the improvement of the catalytic activity, it is therefore desirable to understand, which of these phases is most active so that appropriate modifications in the catalyst preparation protocol may lead to a higher concentration or dispersion of the most active phase. This assignment of catalytic activity to structural features is not straightforward for multi-component catalysts, due to limitations of existing analytical methods; however, structure-activity relations of a series of catalysts may indicate which phases are responsible for the high activity. A structure-activity correlation for the XRD results is shown in Figure 3. Catalysts with moderate activity (commercial $PtCo_x$/C, as prepared $PtCo_3$/C and $PtCo_3$/C-350°C) consist of platinum rich fcc-$PtCo_x$ and Pt_3Co. The latter phase is also present at heat-treatment temperatures in the range from 600 to 1000°C. Therefore, a positive structure-activity correlation does not exist for fcc-$PtCo_x$ and Pt_3Co. A connection between the high activity and the presence of fcc-$PtCo_x$ and Pt_3Co seems unlikely. In contrast, fct-PtCo and fcc-PtCo phases only appear in catalysts with high activity ($PtCo_3$-700°C to $PtCo_3$/C-1000°C). These phases are still present after exposure to electrolyte, as was shown with leaching experiments of $PtCo_3$/C-800°C. The reflexes of the fcc-PtCo and fct-PtCo-phase dominate the diffractograms of $PtCo_3$/C-800°C to $PtCo_3$/C-1000°C. A positive structure activity correlation exists for fcc-PtCo and fct-PtCo. If either phases or just one is responsible for the activity jump is unclear, since both arise in a similar temperature range. The activity decreases above 800°C, despite the presence of fcc-PtCo and fct-PtCo, may be explained with a decreasing surface area of these phases, due to higher sintering at these temperatures. Koh [4] observed the formation of two fcc- and one fct-PtCo phases after heat-treatment and dealloying of $Pt_{50}Co_{50}$ precursors. The specific activities for the orr exceeded 600µA/cm^2_{Pt} at 0.9V (RHE), which was 3 times higher than for Pt/C. Other preparation procedures of $PtCo_x$/C catalysts, without heat-treatment or low-temperature treatment, lead to the formation of Pt-rich fcc-$PtCo_x$, whereas high-temperature treatment of $PtCo_x$ frequently leads to predominant formation of fcc-Pt_3Co [5]. The results of these previous XRD studies seem to support the hypothesis that either the ordered fcc-PtCo or fct-PtCo phase in $PtCo_3$/C-800°C has a higher intrinsic activity than fcc-Pt_3Co, since this catalyst shows a considerably higher specific activity than the catalysts in the above mentioned studies. Also, x-ray amorphous phases may play an important role in the catalytic activity of the investigated catalysts; other analytical methods like XAS may help to get a better understanding of the structure-activity relations.

Conclusions

- Heat-treatment of $PtCo_3$/C at 800°C leads to highest mass activity for oxygen reduction.
- RDE measurements demonstrate an activity of 0.56A/mg_{Pt} at 0.9V (RHE) for $PtCo_3$/C-800°C.
- A structure-activity correlation between high activity and the presence of fcc-PtCo and fct-PtCo was detected.

References

[1] .K. Nørskov, J. Rossmeisl, A. Logadottir, L. Lindquist, J.R. Kitchin, T. Bligaard, H. Johnson; J. Phys. Chem. B **108**, 17886-17892 (2004).

[2] P. Yu, M. Pemberton, P. Plasse; J. Power Sources **144**, 11-20 (2005).

[3] H.A. Gasteiger, S.S. Kocha, B. Sompalli, F.T. Wagner, Appl.Cat. B: Environmental **56**, 9-35 (2005).

[4] S. Koh, P. Strasser; J. Am. Chem. Soc. **129**, 12624-12625 (2007).

[5] E. Antolini, Mat. Chem. and Phys. **78,** 2003, 563-573 and references therein.

Real surface area measurements of Pt/C and $PtCo_x$/C catalysts

H. Schulenburg, J. Durst, E. Müller[1], A. Wokaun, G.G. Scherer

phone: +41 56 310 2125, e-mail: hendrik.schulenburg@psi.ch

In PEFC-electrocatalysis a variety of factors influence the activity of Pt-based catalysts, e.g., composition, presence of poisons, and geometric and electronic properties of the nanoparticles. The knowledge of the real surface area is an important value for the discussion of the catalytic activity for oxygen reduction.

The real surface area of Pt- and Pt-alloy catalysts is frequently investigated by *in-situ* electrochemical methods, where a (sub)monolayer of species, like hydrogen, carbon monoxide or copper is adsorbed and desorbed from the nanoparticle surface. The surface area is then calculated from the charge that originates from the adsorption or desorption of these test species. In this work we analyze the real surface areas of two Pt/C and two $PtCo_x$/C (x≈0.33) catalysts supplied by E-TEK and TKK. As *in-situ* measurements we use desorption of underpotential deposited hydrogen (H-upd) and CO-stripping voltammetry, ex-situ methods are high resolution transmission electron microscopy (HRTEM) and X-ray diffractometry (XRD). Our aim is to compare the reliability of these methods.

Experimental

Pt/C and two $PtCo_x$/C catalysts were applied onto glassy carbon electrodes as thin films [1]. Catalysts were activated by recording 20 cyclic voltammograms with a scan rate of 50mV/s in 0.1M $HClO_4$ at 20°C in the potential range from 50 to 1200mV (RHE). After activation, the H-upd desorption and CO-stripping charges were measured. To obtain better statistics for the error analysis, each catalyst was measured 4 times with 4 different catalyst loadings. TEM and XRD measurements were carried out after the H-upd and CO stripping experiments, because Co-leaching or Pt sintering might have occurred during catalyst activation. Table 1 lists the assumptions and considered error sources of the 4 used methods.

Table 1. *Assumptions and error sources for the real surface area detection of carbon supported Pt and $PtCo_x$ nanoparticles*

Method	Assumptions	Considered error sources
XRD	-spherical particle shape -uniform particle radius -no x-ray amorphous phases -no stress and strain effect -no multigrain crystallites -only one crystalline phase	-peak width -peak maximum -particle density -Scherrer constant
TEM	-no particles < 1nm -spherical particle shape	-particle density -particle radius
H-upd and CO-stripping	-210 µC/cm^2_{Pt} for H_{upd} -420µC/cm^2_{Pt} for CO-stripping -Appropriate correction of background currents -correct integration limits -complete catalyst wetting -no electrolyte impurities	-Pt-loading on electrode

Results and Discussion

Figure 1 shows the calculated real surface areas obtained from TEM, XRD, H-upd and CO-stripping voltammetry. In case of both Pt/C catalysts the XRD surface area is slightly lower than the TEM area. The existence of very small x-ray amorphous particles may explain this difference. Even if the particle size of the Pt/C catalysts is close to the limit for detection by XRD, they match fairly well with the TEM results. The correlation of the TEM and CO-stripping areas is excellent for both Pt/C catalysts. The H-upd areas are about 20% lower than the TEM and CO-stripping areas. This difference may be explained by the conventional method to assume constant double layer charging currents [2] or due to superimposed hydrogen evolution currents [3].

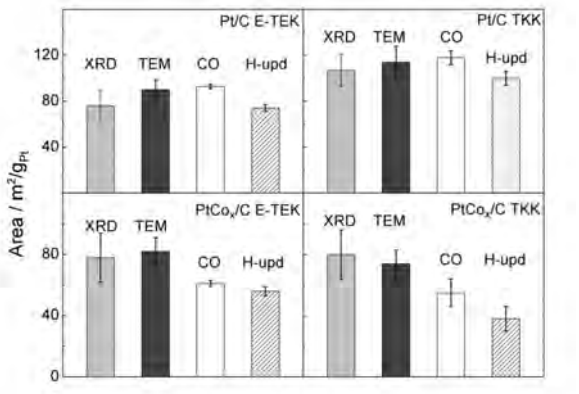

Figure 1. *Comparison of XRD, TEM, H-upd-desorption and CO-stripping voltammetry as methods for the determination of real surface areas of Pt/C and $PtCo_x$/C catalysts*

In case of the $PtCo_x$/C catalysts, the XRD areas agree fairly well with the TEM areas, whereas the electrochemical methods yield much lower surface areas. The discrepancy may be explained by the presence of Co at the particle surface, which contributes to the HRTEM surface area but not to the H-upd surface area. Therefore, the electrochemical methods are misleading for $PtCo_x$/C catalysts; they yield too low surface areas. Considering the required assumptions and error sources of the 4 investigated methods, HRTEM appears to be most reliable for real surface area measurements of Pt and $PtCo_x$ nanoparticles.

References

[1] H.A. Gasteiger, S.S. Kocha, B. Sompalli, F.T. Wagner, Appl. Cat. B: Environmental **56**, 9-35 (2005).

[2] K.J.J. Mayrhofer, D. Strmcnik, B.B. Blizanac, V. Stamenkovic, M. Arenz, N.M. Markovic, Electrochim. Acta **53**, 3181-3188 (2008).

[3] I.A. Schneider, D. Kramer, A. Wokaun, G.G. Scherer, Electrochem. Comm. **9**, 1607-1612 (2007).

[1] ETH Zürich, Zürich

Ultra low Pt anodes for polymer electrolyte fuel cells

B. Schwanitz, H. Schulenburg, M. Horisberger, A. Wokaun, G.G. Scherer

phone: +41 56 310 5629, e-mail: bernhard.schwanitz@psi.ch

The reduction of the Pt catalyst loading in polymer electrolyte fuel cells (PEFC) is a premise for a broad introduction into the market. In state of the art PEFCs, the Pt loading for the anode varies between 50 and 100 µg/cm^2 [1]. These electrodes are usually prepared by application of alcohol/ionomer-based Pt/C inks onto a gas diffusion layer or a polymer electrolyte membrane [1]. The thickness of these layers ranges within a few micrometers. Due to the fast kinetics of the hydrogen oxidation reaction, it is discussed if only a fraction of these catalyst particles participates in the hydrogen oxidation reaction [2, 3]. Provided that solely the catalysts particles in contact with the membrane are active, this fact may be used to reduce the Pt loading at the anode side. Therefore, we prepared and investigated thin Pt layers by sputtering onto gas diffusion media. Our goal is to find a limit for the anode Pt loading, without significant performance and longevity loss for automotive applications.

Experimental

A DC magnetron sputtering set-up ('TIPSI' at the PSI Laboratory of Neutron Scattering) was employed to deposit Pt onto Carbon cloth covered with a micro porous layer of Vulcan XC72. The Pt loading was controlled by the sputtering time and the amount determined by Rutherford Back Scattering Spectroscopy. Sputtered electrodes were tested in 30 cm^2 PEFCs (80°C, 1 bar, H_2/O_2 = 1.5/1.5, fully humidified, E-TEK cathodes (0.5 mg$_{Pt}$/cm^2) without prior ionomer impregnation or activation by cyclic voltammetry. For comparison, an MEA with a commercial electrode as anode (E-TEK LT140EW; 0.5 mg$_{Pt}$/cm^2) was tested under the same conditions.

Results

Transmission Electron Microscopy (TEM)

The sputtered Pt forms particles in the nanometer range, as TEM pictures reveal (Fig. 1). Bright regions show the carbon support and dark ones the Pt nanoparticles. The particles are highly dispersed on the bulb like carbon support, as can be seen in Figure 1.

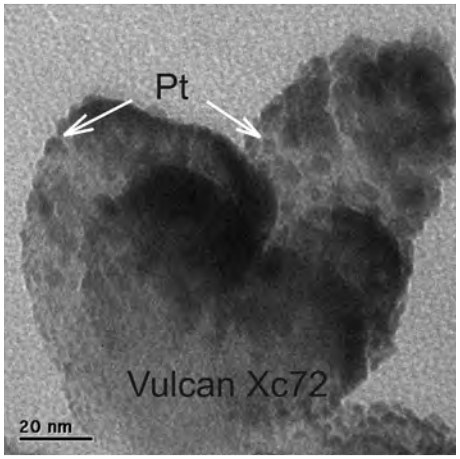

Figure 1. *TEM image of Pt sputtered onto Carbon Black (Vulcan XC72).*

Fuel Cell Performance

MEAs with different Pt loadings were operated at 0.5 A/cm^2 under the above described fuel cell conditions for up to 500 h. After 22 h of run time, MEA1 (3 µg$_{Pt}$/cm^2) reached a power density of 0.544 W/cm^2 at 0.6 V, MEA2 (26.8 µg$_{Pt}$/cm^2) a value of 0.744 W/cm^2, and the E-TEK MEA a value of 0.740 W/cm^2. Thus, MEA2 shows similar performance at 0.6V, but with only a 5% Pt loading on the anode side, compared to the E-TEK MEA. MEA1 shows a 26.5% less performance than the E-TEK MEA at the same voltage, having only 0.6% of its Pt loading. Yet, for higher current densities, a significant voltage loss is observed. This is probably due to mass transport limitations on the anode side, resulting from the low Pt loading. After 310 h and 500 h run time, MEA1 and MEA2 lose 48% and 18% of performance at 0.6V, respectively.

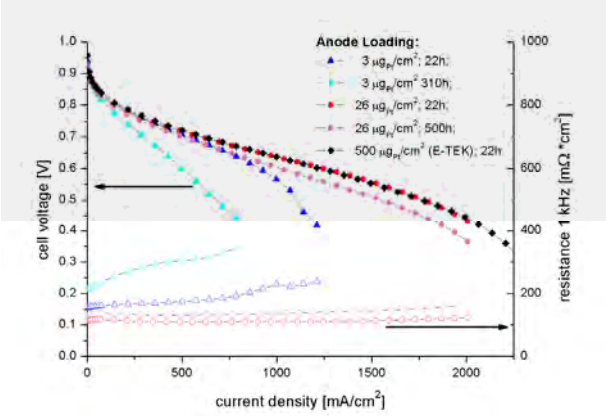

Figure 2. *Current-Voltage-Curve; MEA1 and MEA2: Anode: 3 µg$_{Pt}$/cm^2 and 26.8 µg$_{Pt}$/cm^2 sputter deposited on ELAT gas diffusion layer, E-TEK: Anode: 500 µg$_{Pt}$/cm^2; Cathode: 500 µg$_{Pt}$/cm^2 (ETEK), 80°C, H_2/O_2, 1 bar, stoichiometry 1.5/1.5, fully humidified; operated at 0.5A/ cm^2.*

Part of the performance loss of MEA1 and MEA2 could be due to degradation processes at the membrane electrode interface, leading to higher membrane resistance. The i-E-curves corrected for this resistance shows 2.1% loss in performance for MEA2 at 0.5 A/cm^2, and 5.5% loss for MEA1. Thus, it can be seen that MEA2 exhibits similar performance as the E-TEK MEA, even after 500 h run time, while MEA1 lacks durability and performance not only due to membrane degradation. For future studies, MEAs with 15µg$_{Pt}$/cm^2 will be prepared and tested for fuel cell performance. Post mortem analysis with high-resolution SEM, as well as stability tests under various humidification conditions will be performed.

References

[1] H.A. Gasteiger, S.S. Kocha, B. Sompalli, F.T. Wagner, Appl. Catal. B-Environmental **56**, 9-35 (2005).

[2] S.Y. Cha, W.M. Lee, J. Electrochem. Soc., **146**, 4055 (1999).

[3] A.T. Haug, R.E. White, J.W. Weidner, W. Huang, S. Shi, T. Stoner, N. Rana, J. Electrochem. Soc., **149**, A280-A287 (2002).

THE ELECTROCHEMISTRY LABORATORY

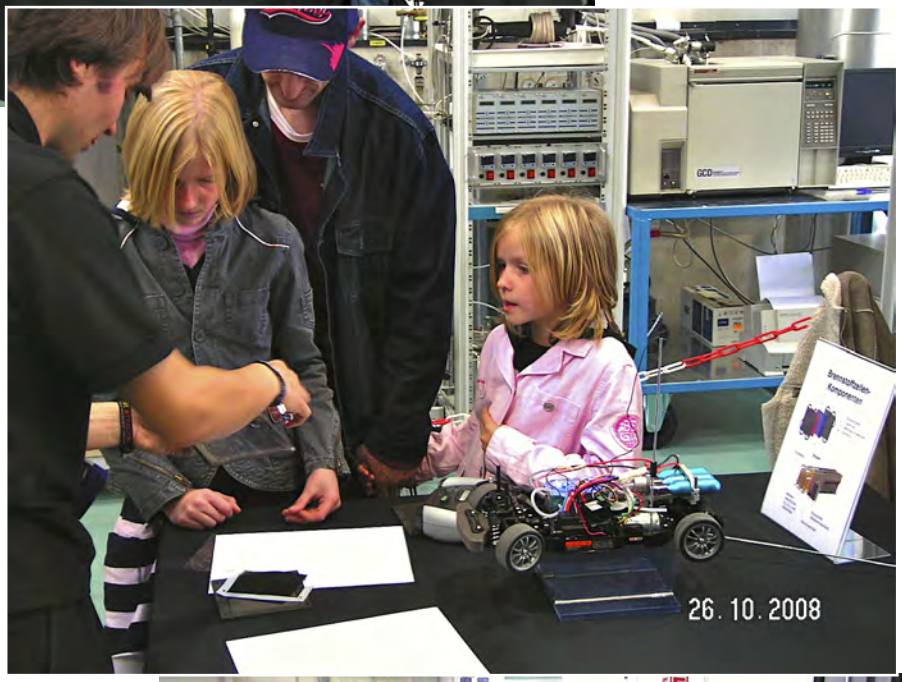

Impressions of the "PSI – open day" on October 25 and 26.

Visitors of all ages inspected the exhibits of the Electrochemistry Laboratory.

Pictures: Fuel Cell system of the Hy-Light (top), a fuel cell model car (middle) and the supercapacitor stack of the Hy-Light (bottom).

STRUCTURE

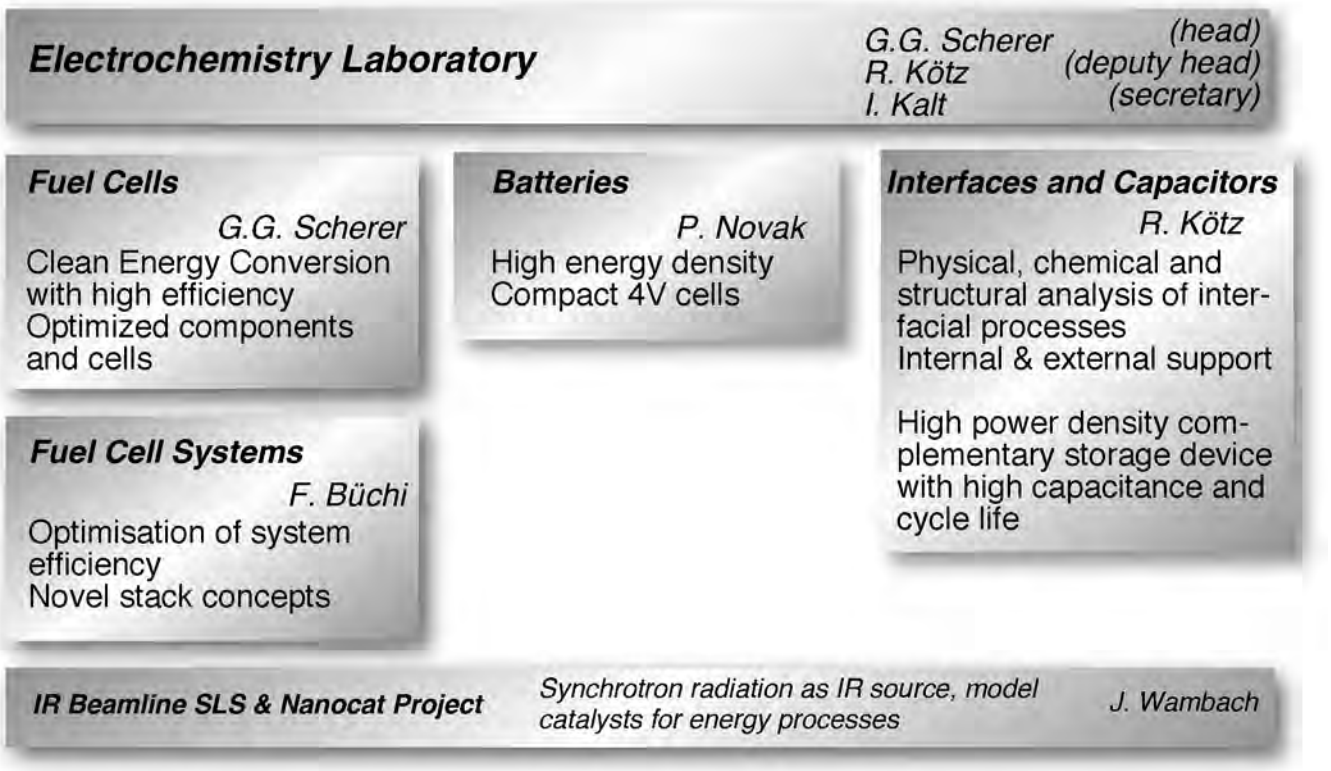
Electrochemistry Laboratory
G.G. Scherer (head)
R. Kötz (deputy head)
I. Kalt (secretary)
Fuel Cells
G.G. Scherer
Clean Energy Conversion with high efficiency
Optimized components and cells
Batteries
P. Novak
High energy density
Compact 4V cells
Interfaces and Capacitors
R. Kötz
Physical, chemical and structural analysis of inter-facial processes
Internal & external support
High power density com-plementary storage device with high capacitance and cycle life
Fuel Cell Systems
F. Büchi
Optimisation of system efficiency
Novel stack concepts
IR Beamline SLS & Nanocat Project
Synchrotron radiation as IR source, model catalysts for energy processes
J. Wambach

ECL-PERSONNEL

Staff

Bernard Jérôme, Dr. (since April) ♦ Büchi Felix, Dr.

Colin François, Dr. (since January) ♦ Colinart Thibaut (since November) ♦ Czekaj Izabela, Dr.

Foelske Annette, Dr.

Geiger Friederike (until May) ♦ Gloor Thomas ♦ Gubler Lorenz, Dr.

Henkensmeier Dirk, Dr. (since February) ♦ Hofer Marcel (since January)

Kaiser Hermann ♦ Kalt Isabella ♦ Kötz Rüdiger, Dr.

Lüscher Sandro (since June)

Maire Pascal ♦ Märkle Wolfgang, Dr. ♦ Marmy Christian

Ng Desmond, Dr. (until November) ♦ Novak Petr, Dr.

Perego Raffaella, Dr. (since November)

Scheifele Werner ♦ Scherer Günther G., Dr. ♦ Schneider Ingo, Dr. ♦ Schulenburg Hendrik, Dr.

Tsukada Akinori (until May) ♦ Thut Jürg (since September)

von Roth Fritz (until May)

Wambach Jörg, Dr.

PhD Students

Bayer Michael ♦ Ben Youcef Hicham ♦ Bernardo Philippe (since April) ♦ Boillat Pierre

Cericola Dario (since February) ♦ Chew Sophie (until November)

Dockheer Sindy

Farquet Patrick (until April)

Godbole Vikram (since October)

Hintennach Andreas

La Mantia Fabio (until June) ♦ Linse Nicolas (since April) ♦ Loviat François (until October)

Menamparambath Mini Mol (since June)

Oberholzer Pierre (since August)

Patey Timothy

Reum Mathias (until August) ♦ Rosciano Fabio (until June) ♦ Ruch Patrick

Savouchkina Anastasia (since June) ♦ Schuler Gabriel ♦ Schwanitz Bernhard (since June) ♦ Seyfang Bernhard ♦ Simmen Franziska

Verma Pallavi (since October) ♦ Von Dahlen Steffen (since August)

Wallasch Frank

Zaglio Maurizio ♦ Zellweger Hans

AWARDS

Patrick Ruch	The Oronzio and Niccolò De Nora Foundation Young Author Prize 2008 of the International Society of Electrochemistry. *In situ X-ray diffraction of the intercalaction of $(C_2H_5)_4N^+$ and BF_4^- into graphite from acetonitrile and propylene carbonate based supercapacitor electrolytes* Electrochim. Acta 53, 1074-1082, 2007.
Holger Kuhn	ABB Forschungspreis 2008 PhD-Thesis *In Situ Charakterisierung von Polymer-Elektrolyt Brennstoffzellen mittels Elektrochemischer Impedanzspektroskopie.*
B.C. Seyfang, P. Boillat, G.G. Scherer, T. Lippert, A. Wokaun	Best Poster Award *Micro-structuring of glassy carbon for micro polymer electrolyte fuel cells: Ns-shadowgraphy during laser ablation* E-MRS Spring Meeting 2008, Strasbourg, France, May 26-30, 2008.
Dario Cericola	Premio di Laurea "PhotoAnalytical srl " of the Divisione di Elettrochimica della Societa' Chimica Italiana. Master Thesis *Materiali carboniosi e liquidi ionici per supercapacitori a doppio strato.*
I. Czekaj, F. Loviat, J. Wambach, A. Wokaun	SCS 2008 Poster Prize Award *Nickel deposition on γ-Al_2O_3: Modelling of metal particles behaviour at the support* Swiss Chemical Society - Fall Meeting 2008, University Zürich, Zürich, September 11, 2008.

THESE PHD STUDENTS FROM ECL GRADUATED IN 2008

Dr. Fabio La Mantia

Characterization of electrodes for lithium-ion-batteries through electrochemical impedance spectroscopy and mass spectrometry

Ph.D. Thesis, No. 17848, ETH Zürich, June 2008

Advisors Prof. Dr. R. Nesper, ETH Zürich
Prof. Dr. A. Wokaun, PSI/ETH Zürich
PD Dr. P Novák, PSI Villigen

Dr. Fabio Rosciano

In-situ synchrotron and neutron diffraction based methods for the characterization of cathodic materials for lithium-ion-batteries

Ph.D. Thesis, No. 17847, ETH Zürich, June 2008

Advisors Prof. Dr. A. Wokaun, PSI/ETH Zürich
Prof. Dr. R. Nesper, ETH Zürich
PD Dr. P. Novák, PSI Villigen

Dr. Patrick Farquet

Synchrotron radiation grafting: A lithographic method to create polymer micro- and nanostructures

Ph.D. Thesis, No. 17711, ETH Zürich, April 2008

Advisors Prof. Dr. A. Wokaun, PSI/ETH Zürich
Prof. Dr. N.D. Spencer, ETH Zürich
Dr. C. Padeste, PSI Villigen
Dr. rer. nat. G.G. Scherer, PSI Villigen

Dr. Mathias Reum

Sub-millimeter resolved measurement of current density and membrane resitstance in polymer electrolyte fuel cells (PEFC)

Ph.D. Thesis, No. 17979, ETH Zürich, September 2008

Advisors Prof. Dr. A. Wokaun, PSI/ETH Zürich
Prof. Dr. B. Schönfeld, ETH Zürich
Dr. ret. nat. G.G. Scherer, PSI Villigen
Dr. F. Büchi, PSI Villigen

Dr. François Loviat

Photo-assisted activation of methane over supported catalysts with a xenon excimer lamp

Ph.D. Thesis, No. 18145, ETH Zürich, December 2008.

Advisors: Prof. Dr. A. Wokaun, PSI/ETH Zürich
Dr. J. Wambach, PSI Villigen

EXCHANGE STUDENTS, DIPLOMA THESES, SUMMER STUDENTS

Denis Tehlar	*Investigation of the cross-convection in PEFC serpentine flow-fields* ETH Zürich, September 2007 – March 2008.
Dominik Rätz	*Sub-mm Membranwiderstand in PEFC – Methodenentwicklung und Bestimmung des Einflusses der Gaszusammensetzung an der Kathode* ETH Zürich, October 2007 – February 2008.
Anna Evans	*In situ colorimetric analsysis of lithium intercalation into graphite electrodes of lithium-ion-batteries* ETH Zürich, October 2007 – February 2008.
Verena Klass	*AMS/MAN copolymerization onto ETFE base film using DIPB as crosslinking agent* ETH Zürich, February – April 2008.
Sofia Rudin	Mechanical and electrochemical properties of ETFE based membranes for PEFC ETH Zürich, March – August 2008.
Michael Uldry	*Elektrochemische Charakterisierung von gesputterten Pt/C-Katalysatoren* Fachhochschule beider Basel (Nordwestschweiz), April – July 2008.
Julien Durst	*Real surface area measurements of Pt/C and Pt3Co/C catalysts* ENSEEG (Ecole Nationale Supérieure d'Electrochimie et d'Electrométallurgie de Grenoble) FR, April – July 2008.
Marcelo Do Carmo	*Electrochemical characterization of platinum electrocatalysts supported on polystyrene sulphonic grafted carbon black for PEMFC applications* Technical Research Institute of Sao Paulo, BR, August – September 2008.
Juan Luis Gomez Camer	*Silicon-carbon composite electrodes for lithium-ion batteries.* University of Cordoba, ES, September – December 2008.
David Bailie	*SNIFTIRS investigation of the oxidative decomposition mechanism of organic-carbonate-based electrolytes in lithium-ion batteries using glassy carbon and nickel working electrodes* Queen's University Belfast, IE, June – August 2008.
Matthias Burgener	*Hydrogen under potential deposition experiments on micro-patterned glassy carbon electrodes* Universität Bern, July – August 2008.
Mark Zurbrügg	*Synthese und elektrochemische Charakterisierung von PtCox/C Katalysatoren für die elektrochemische Sauerstoffreduktion* Universität Bern, July – August 2008.

SEMINAR, INVITED SPEAKERS

Prof. Patrice Simon Université Toulouse, FR	*Nanostructured interfaces in electrodes for energy storage devices* January 14, 2008.
Prof. Dr. Angelika Heinzel Universität Duisburg-Essen, DE	*F&E-Portfolio des Zentrums für Brennstoffzellentechnik in Duisburg* February 15, 2008.
Dr. Alexander Bittner MPI, Stuttgart, DE	*Hochporöser Kohlenstoff in Superkondensatoren* February 18, 2008.
Dr. Timo Jacob Fritz Haber Institut, Berlin, DE	*Theoretical modeling of electrochemical systems* February 26, 2008.
Dr. Rolf Hempelmann Universität Saarland, DE	*Nano-Elektrochemie* March 03, 2008.
Prof. Mark Orazem University of Florida, USA	*Application of impedance spectroscopy to PEM fuel cells: Interpretation of low-frequency inductive loops* April 14, 2008.
Lukas Durrer ETH Zürich	*Electrochemical formation of:* *-Fe catalyst nanoparticle for SWNT growth* *-Bi_2+xTe_3-x for an increase in TEG performance* *May 19, 2008.*
Dr. Masashi Arita IP Center of Dainippon Screen, Kyoto, JP	*Presentation of the Company Profile and R&D Activities* June 02, 2008.
Dr. Ting He Honda Research Institute USA	*Platinum alloy electrocatalysts: Discovery, synthesis and durability* June 20, 2008.
Prof. Steven Holdcroft, Simon Fraser University, Vancouver, CA	*Model polymers for the systematic study of morphology of fuel membranes. Batteries not included* June 23, 2008.
Dr. Michael Eikerling. Assist. Prof. Simon Fraser University, Burnaby, CA	*Materials and processes in PEFCs: The balancing act of complex morphologies and water* June 27, 2008.
Prof. Josef Hormes Universität Bonn, DE	*Die Charakterisierung von metallischen Nanoteilchen mittels Röntgenabsorptionsspektroskopie* July 24, 2008.
Prof. Yuping Wu Fudan University, Shanghai, CN	*Novel anode materials for lithium ion batteries* September 15, 2008.

Dr. Kai-C. Möller Fraunhofer Institut für Silicatforschung, Würzburg, DE	*Elektroden und Elektrolyte für Batterien und Supercaps auf Basis nanostruktureller Materialien* September 29, 2008.
Dr. B. Panella ETH Zürich	*Hydrogen storage technologies* October 06, 2008.
Prof. Joannis Kallitsis, University of Patras, GR	*Influence of the molecular structure on the properties of high temperature polymer electrolyte membranes* October 27, 2008.
Prof. Doron Aurbach Bar-Ilan Universität, IL	*Studies of activated carbon electrodes for EDLC devices and separation processes* October 27, 2008.
Dr. Tetsuya Yamaki Japan Atomic Energy Agency, JP	*Our strategies for preparation of polymer electrolyte membranes: construction of multiply-crosslinked structures and application of ion-track technology* November 03, 2008.
Dr. Günter Gutmann Esslingen, DE	*Elektrische Stromquellen für Mobilität, Stand der Technik und zukünftige Potentiale* November 03, 2008.
Dr. Wolfgang H. Meyer Max Planck Institut, Mainz, DE	*Proton conductive polymers for improved fuel cell applications* November 10, 2008.
Prof. Takuto Araki Yokohama National University (YNU), Japan	Introduction of fuel cell research activity at YNU December 08, 2008.
Prof. Tom Zawodzinski Case Western Reserve University, Cleveland, USA	Composite electrode issues December 15, 2008.
Dr. Nancy Garland US DOE, USA	US DOE fuel cell activities December 15, 2008.

Electrocatalysis

24th One-Day-Symposium
May 7, 2008
Organizers: G.G. Scherer and R. Kötz

Contributions from:

Francesco Di Quarto Universität Palermo, IT
Manuel M. Lohrengel, Universität Düsseldorf, DE
Rolf Schuster, Universität Karlsruhe, DE
Wolfgang Kautek, Universität Wien, AT
Jean-Claude Puippe, Innosurf, Châtel-St-Denis, CH
Achim Walter Hassel, MPI Düsseldorf, DE

Lecturers and organization staff in action shortly before the start of the symposium

REVIEW ACTIVITIES OF THE LABORATORY

Journals

Advanced Materials ♦ Advanced Functional Materials ♦ Angewandte Chemie

Carbon ♦ Chemical Reviews

Electrochimica Acta ♦ Electrochemistry Communications ♦ Electrochemical and Solid-State Letters

Journal of the Electrochemical Society ♦ Journal of Experimental Heat Transfer ♦ Journal of New Materials for Electrochemical Systems ♦ Journal of Physical Chemistry ♦ Journal of Physics D: Applied Physics ♦ Journal of Power Sources ♦ Journal of Solid State Electrochemistry ♦ Journal of Electroanalytical Chemistry

Materials Chemistry and Physics

Simulation Modelling Practice and Theory

Co-Referee's Report for Dissertations

P. **F**arquet, PSI/ETH Zürich
F. **L**a Mantia, PSI/ETH Zürich, F. Loviat, PSI/ETH Zürich
M. **R**eum, PSI/ETH Zürich, F. Rosciano, PSI/ETH

INDUSTRIAL PARTNERS

The Laboratory had the pleasure to collaborate with the following industrial partners during the year 2008:

Belenos, Biel ♦ Bucher Schörling, Niederweningen

CEKA Elektrowerkzeuge AG, Wattwil ♦ Ciba, Basel

MES DEA, Stabio

Nissan Motors Co., Ltd. Yokosuka, Japan

Proton Motors, Puchheim, Deutschland

TIMCAL AG, Bodio

PROJECT COLLABORATIONS WITH EXTERNAL PARTNERS

CCEM

F.N. Büchi Projektleiter PSI	hy.muve: Development of **hy**drogen powered **mu**nicipal **ve**hicle with EMPA Dübendorf and Industrial Partners

BFE

F.N. Büchi Projektleiter	*Cal.PEF-CH: Modelbased investigation of PE fuel cell performance with focus on porous layer properties* with ZHAW, Winterthur
L. Gubler Projektleiter	*Lebensdauer Limitierungen von Brennstoffzellen- Membranen: Mechanismen, Methoden und Innovationen*
L. Gubler, I.A. Schneider Projektleiter	*go.PEF-CH: Enhancing PEFC durability and reliability under application-relevant conditions* Partner: Berner Fachhochschule Technik und Informatik (BFH-TI, Biel BE), CEKA Elektrowerkzeuge AG & Co. KG (Wattwil SG), MES-DEA SA. (Stabio TI)
G.G. Scherer, L. Gubler Projektleiter	*Protonen-Leitende Polymermembranen für Brennstoff- und Elektrolysezellen*

EU

G.G. Scherer Projektleiter	*EU-Project CARISMA*
I.A. Schneider Projektleiter	*EU-Project Nanoglowa (Diagnostics workpackage)*

Industry

P. Boillat, G.G. Scherer Projektleiter	*Diagnostics of polymer electrolyte fuel cells* Automotive industry
P. Boillat, G.G. Scherer Projektleiter	*Diagnostics of polymer electrolyte fuel cells* Nissan Motor Co. Ltd., Yokohama, Japan
F. N. Büchi Projektleiter	*Diagnostics of polymer electrolyte fuel cells* Automotive Industry
P. Maire Projektleiter	*Electrochemical characterization of polymeric organic active materials* Ciba, Basel
W. Märkle Projektleiter	*Graphite für Lithiumionen-Batterien* TIMCAL SA, Bodio

TEACHING ACTIVITIES

University Level Teaching

PD Dr. P. Novák, Prof. Dr. A. Wokaun	*Technische Elektrochemie* ETH Zürich, HS 2008
Prof. Dr. A. Wokaun, Dr. G.G. Scherer, Prof. Dr. K. Boulouchos	*Renewable Energy Technologies II* ETH Zürich, SS 2008

PUBLICATIONS

Books and Reviewed Book Chapters

S. Alkan-Gürsel, L. Gubler, B. Gupta, G.G. Scherer	*Radiation grafted membranes* Adv. Polym. Sci. **215**, 157–217 (2008). In: Fuel Cells I Edited by G.G. Scherer, Springer Verlag Berlin-Heidelberg, ISBN 978-3-540-69755-8. doi: 10.1007/12_2008_153
K.A. Friedrich, F.N. Büchi	*Fuel cells using hydrogen* In: Hydrogen as a Future Energy Carrier, **8.1**, 335-363 (2008). Edited by A. Züttel, A. Borgschulte, L. Schlapbach, Wiley VCH, Weinheim, ISBN: 978-3-527-30817-0.
L. Gubler, G.G. Scherer	*A proton-conducting polymer membrane as solid electrolyte – Function and required properties* Adv. Polym. Sci. **215,** 1-14 (2008). In: Fuel Cells I Edited by G.G. Scherer, Springer Verlag Berlin-Heidelberg, ISBN 978-3-540-69755-8. doi: 10.1007/12_2008_156
G.G. Scherer, Ed	*Fuel Cells I,* Adv. Polym. Sci. **215**, Springer-Verlag, Berlin-Heidelberg (2008) ISBN 978-3-540-69755-8. doi: 10.1007/978-3-540-69757-2
G.G. Scherer, Ed	*Fuel Cells II,* Adv. Polym. Sci. **216**, Springer-Verlag, Berlin-Heidelberg (2008) ISBN 978-3-540-69763-3. doi: 10.1007/978-3-540-69765-7

Peer Reviewed Papers

S. Alkan Gürsel, J. Schneider[1], H. Ben youcef, A. Wokaun, G.G. Scherer	*Thermal properties of proton-conducting radiation grafted membranes* J. Appl. Polym. Sci. **108**, 3577-3585 (2008). doi: 10.1002/app.27947 [1] ETH Zürich
A.R. Armstrong[1], D.W. Tee[1], F. La Mantia, P. Novák, P.G. Bruce[1]	*Synthesis of tetrahedral $LiFeO_2$ and its behavior as cathode in rechargeable lithium batteries* J. Am. Chem. Soc. **130**, 3554-3559 (2008). doi: 10.1021/ja077651g [1] University of St. Andrews, St. Andrews, UK

F. Atchison, A. Bergmaier[1], M. Daum, M. Döbeli, G. Dollinger[1], P. Fierlinger, A. Foelske, R. Henneck, S. Heule, M. Kasprzak[2], K. Kirch, A. Knecht, M. Kuzniak[3], A. Pichlmaier, R. Schelldorfer, G. Zsigmond

Surface characterization of diamond-like carbon for ultracold neutron storage
Nucl. Instrum. Methods Phys. Res., Sect. A **587**, 82-88 (2008).
doi: 10.1016/j.nima.2007.12.037
[1] Universität der Bundeswehr München, Germany
[2] Stefan Meyer Institute, Vienna, Austria
[3] Jagiellonian University, Cracow, Poland

H. Ben youcef, S. Alkan Gürsel, A. Wokaun, G.G. Scherer

The influence of crosslinker on the properties of radiation-grafted films and membranes based on ETFE
J. Membr. Sci. **311**, 208-215 (2008).
doi: 10.1016/j.memsci.2007.12.015

P. Boillat, D. Kramer, B.C. Seyfang, G. Frei, E. Lehmann, G.G. Scherer, A. Wokaun, Y. Ichikawa[1], Y. Tasaki[1], K. Shinohara[1]

In situ observation of the water distribution across a PEFC using high resolution neutron radiography
Electrochem. Commun. **10**, 546-550 (2008).
doi: 10.1016/j.elecom.2008.01.018
[1] Nissan Motor Co., Ltd., Yokosuka-shi, Japan

P. Boillat, G.G. Scherer, A. Wokaun, G. Frei, E.H. Lehmann

Transient observation of ^{2}H labeled species in an operating PEFC using neutron radiography
Electrochem. Commun. **10**, 1311-1314 (2008).
doi: 10.1016/j.elecom.2008.06.016

F.N. Büchi, M. Reum

Measuring the local membrane resistance in PEFC on the sub-mm scale
Meas. Sci. Technol. **19**, 85702-707 (2008).
doi: 10.1088/0957-0233/19/8/085702

F.P. Campana, H. Buqa, P. Novák, R. Kötz, H. Siegenthaler[1]

In situ atomic force microscopy study of exfoliation phenomena on graphite basal planes
Electrochem. Commun. **10**, 1590-1593 (2008.)
doi: 10.1016/j.elecom.2008.08.026
[1] University of Bern, Bern

P. Farquet, C. Padeste, H.H. Solak, S.A. Gürsel, G.G. Scherer, A. Wokaun

Extreme UV-radiation grafting of glycidyl methacrylate nanostructures onto fluoropolymer foils by RAFT-mediated polymerization
Macromolecules **41**, 6309-6316 (2008).
doi: 10.1021/ma800202b

P. Farquet, C. Padeste, M. Börner[1], H. Ben youcef, S. Alkan-Gürsel, G.G. Scherer, H.H. Solak, V. Saile[1], A. Wokaun

Microstructured proton conducting membranes by synchrotron radiation induced grafting
J. Membr. Sci. **325**, 658-664 (2008).
doi: 10.1016/j.memsci.2008.08.040
[1] Forschungszentrum Karlsruhe, Institute for Microstructure Technology, Karlsruhe, Germany

R. Flückiger, S.A. Freunberger, D. Kramer, A. Wokaun, G.G. Scherer, F.N. Büchi

Anisotropic, effective diffusivity of porous gas diffusion layer materials for PEFC
Electrochim. Acta **54**, 551-559 (2008).
doi: 10.1016/j.electacta.2008.07.034

S.A. Freunberger, I.A. Schneider, P.-C. Sui[1], A. Wokaun, N. Djilali[1], F.N. Büchi

Cell interaction phenomena in polymer electrolyte fuel cell stacks
J. Electrochem. Soc. **155**, B704-B714 (2008).
doi: 10.1149/1.2913095
[1] University of Victoria, Victoria BC, Canada

R. Gadiou[1], A. Didion[1], R.I. Gearba[1], D.A. Ivanov[1], I. Czekaj, R. Kötz, C. Vix-Guterl[1]

Synthesis and properties of new nitrogen-doped nanostructured carbon materials obtained by templating of mesoporous silicas with aminosurgars
J. Phys. Chem. Solids **69**, 1808-1814 (2008).
doi: 10.1016/j.jpcs.2008.01.006
[1] CNRS UPR 9069, Mulhouse, France

L. Gubler, H. Ben Youcef, S. Alkan Gürsel, A. Wokaun, G.G. Scherer

Crosslinker effect in ETFE based radiation grafted proton conducting membranes
I. Properties and fuel cell performance characteristics
*J. Electrochem. Soc. **155**, B921-B928 (2008).*
doi: 10.1149/1.2951919

M. Hahn, H. Buqa, P.W. Ruch, D. Goers[1], M.E. Spahr[1], J. Ufheil, P. Novák, R. Kötz

A dilatometric study of lithium intercalation into powder-type graphite electrodes
Electrochem. Solid-State Lett. **11**, A151-A154 (2008).
doi: 10.1149/1.2940573
[1] TIMCAL SA, Bodio

L.J. Hardwick, P.W. Ruch, M. Hahn, W. Scheifele, R. Kötz, P. Novák

In situ Raman spectroscopy of insertion electrodes for lithium-ion batteries and supercapacitors: First cycle effects
J. Phys. Chem. Solids **69**, 1232-1237 (2008).
doi: 10.1016/j.jpcs.2007.10.017

R. Kötz, M. Hahn, P.W. Ruch, R. Gallay[1]

Comparison of pressure evolution in supercapacitor devices using different aprotic solvents
Electrochem. Commun. **10**, 359-362 (2008).
doi: 10.1016/j.elecom.2007.12.016
[1] Maxwell Technologies SA, Rossens

D. Kramer, S.A. Freunberger, R. Flückiger, I.A. Schneider, A. Wokaun, F.N. Büchi, G.G. Scherer

Electrochemical diffusimetry of fuel cell gas diffusion layers
J. Electroanal. Chem. **612**, 63-77 (2008).
doi: 10.1016/j.jelechem.2007.09.014

F. La Mantia, P. Novák

Online detection of reductive CO_2 development at graphite electrodes in the 1 M $LiPF_6$, EC: DMC battery electrolyte Electrochem. Solid-State Lett. **11**, A84-A87 (2008).
doi: 10.1149/1.2890756

F. La Mantia, J. Vetter, P. Novák

Impedance spectroscopy on porous materials: A general model and application to graphite electrodes of lithium-ion batteries
Electrochim. Acta **53**, 4109-4121 (2008).
doi: 10.1016/j.electacta.2007.12.060

F. La Mantia, R. Rosciano, N. Tran, P. Novák

Direct evidence of oxygen evolution from $Li_{1+x}(Ni_{1/3}Mn_{1/3}Co_{1/3})_{1-x}O_2$ at high potentials
J. Appl. Electrochem. **38**, 893-896 (2008).
doi: 10.1007/s10800-008-9491-9

P. Maire, A. Evans, H. Kaiser, W. Scheifele, P. Novák

Colorimetric determination of lithium content in electrodes of lithium-ion batteries
J. Electrochem. Soc. **155**, A862-A865 (2008)
doi: 10.1149/12979696

A. Mantion[1], A.G. Guex[1], A. Foelske, L. Mirolo[2], K.M. Fromm[2], M. Painsi[3], A. Taubert[1,4,5]

Silver nanoparticle engineering via oligovaline organogels
Soft Matter **4**, 606-617 (2008).
doi: 10.1039/b712826f
[1] University of Basel, Basel
[2] University of Fribourg, Fribourg
[3] University of Bern, Bern
[4] University of Potsdam, Germany
[5] Max-Planck-Institute, Golm, Germany

K. Mortensen[1], U. Gasser, S. Alkan Gürsel, G.G. Scherer

Structural characterization of radiation grafted block copolymer films, using SANS technique
J. Polymer Sci: Part B: Polymer Physics, **46**, 1660-1668 (2008).
doi: 10.1002/polb.21502
[1] University of Copenhagen, Denmark

S.H. Ng, N. Tran, K. G. Bramnik[1], H. Hibst[1], P. Novák

A feasibility study on the use of $Li_4V_3O_8$ as a high capacity cathode material for lithium-ion batteries.
Chem. Eur. J., **14**, 11141-11148 (2008).
doi: 10.1002/chem.200800286
[1] BASF SE, Ludwigshafen*, Germany*

T.J. Patey, S.H. Ng, R. Büchel[1], N. Tran, F. Krumeich[1], J. Wang[2], H.K. Liu[2], P. Novák

Electrochemistry of LiV_3O_8 nanoparticles made flame spray pyrolysis
Electrochem. Solid-State Lett. **11**, A46-A50 (2008).
doi: 10.1149/1.2836741
[1] ETH Zürich
[2] University of Wollongong, Australia

R. Rosciano, M. Holzapfel, W. Scheifele, P. Novák

A novel electrochemical cell for in situ neutron diffraction studies of electrode materials for lithium-ion batteries
*J. Appl. Cryst. **41**, 690-694 (2008).*
doi: 10.1107/S0021889808018025

I.A. Schneider, H.M. Bayer, A. Wokaun, G.G. Scherer

Impedance response of the proton exchange membrane in polymer electrolyte fuel cells
J Electrochem. Soc. **155**, B783-B792 (2008).
doi: 10.1149/1.2929823

F. Simmen, T. Lippert, P. Novák, B. Neuenschwander[1], M. Döbeli[2], M. Mallepell[2], A. Wokaun

The influence of lithium exess in the target on the properties and compositions of $Li_{1+x}Mn_2O_{4-\delta}$ thin films prepared by PLD
Appl. Phys. A **93**, 711-716 (2008).
doi: 10.1007/s00339-008-4701-1
[1] Berner Fachhochschule, Burgdorf
[2] PSI / ETH Zürich

N. Tran, K.G. Branmik[1], H. Hibst[1], J. Prölss[1], N. Mronga[1], M. Holzapfel, W. Scheifele, P. Novák

Spray-drying synthesis and electrochemical performance of lithium vanadates as positive electrode materials for lithium batteries
J. Electrochem. Soc. **155,** A384-A389 (2008).
doi: 10.1149/1.2884859
[1] BASF SE, Ludwigshafen, Germany

X. Wei, A. Reiner, E. Müller[1], A. Wokaun, G.G. Scherer, L. Zhang[1], K.-Y. Shou[1], B.J. Nelson[1]

Electrochemical surface reshaping of polycrystalline platinum: morphology and crystallography
Electrochem. Acta **53**, 4051-4058 (2008).
doi: 10.1016/j.electacta.2007.08.071
[1] ETH Zürich

K. Yoshizawa[1],K. Ikezoe[1], Y. Tasaki[1], D. Kramer, E.H. Lehmann, G.G. Scherer	*Analysis of gas diffusion layer and flow-field design in a PEMFC using neutron radiography* J. Electrochem. Soc. **155**, B223-B227 (2008). doi: 10.1149/1.2823003 [1] Nissan Research Center, Yokosuka-shi, Japan

Conference Proceedings / Other Papers

F.N. Büchi, R. Flückiger, D. Tehlar, F. Marone, M. Stampanoni	*Determination of liquid water distribution in porous transport layers* ECS Transactions **16**, 587-592 (2008). doi: 10.1149/1.2981893
L. Gubler, S. Alkan Gürsel, H. Ben youcef, F. Wallasch, A. Wokaun, G.G. Scherer	*Recent advances in radiation grafted fuel cell membranes* Proc. Fundamentals and Developments of Fuel Cell Conference 2008, ISBN 978-2-7466-0413-1, Nancy, France, Dec 10-12 (2008).
P. Novák	*Beyond the conventional approach: An in situ look at battery materials* 49th Battery Symposium in Japan, Book of Abstracts, 429-430, Sakai, Japan, November 5-7 (2008).
P.W. Ruch, D. Cericola, S.H. Ng, A. Foelske, R. Kötz	*Single wall carbon nanotubes for supercapacitors studied by in situ Raman spectroscopy and in situ dilatometry* Proc. 18th International Seminar on Double Layer Capacitors and Hybrid Energy Storage Devices, 80-90, Deerfield Beach, USA, December 8-10 (2008).
M. Zaglio, G.A. Schuler, A. Wokaun, J. Mantzaras, F.N. Büchi	*Parameter extraction from experimental data using multiparameter optimization algorithms* Proc. Fundamentals and Developments of Fuel Cells Conference 2008, ISBN 978-2-7466-0413-1,Nancy, France, December 10-12 (2008).

TALKS

Invited Talks

F.N. Büchi	*Hydrogen based mobility: Developments in Europe* COME 2008, International Conference on Mobility and Energy, Vienna, Austria, February 28, 2008.
F.N. Büchi	*Sizing of fuel cell powertrains for mobile applications* HYCELTEC 2008, International Symposium on Hydrogen and Fuel Cells, Bilbao, Spain, July 3, 2008.
L. Gubler	*Trends for fuel cell membrane development* 12th Aachener Membran Kolloquium, Aachen, Germany, October 29, 2008.
M.P. Hofer	*Freezing of PEFC* IEA HEV Annex XIII Workshop, Cold start behavior of FC vehicles, Geneva, March 12, 2008.
R. Kötz	*SuperCaps basics* *Applications of SuperCaps* International Max Planck Research School (IMPRS) Energy, Patras, Greece, June 1-8, 2008.

P. Novák	*Beyond the conventional approach: An in situ look at battery materials* 49th Battery Symposium in Japan, Sakai, Japan, November 6, 2008.
P. Novák	*Oxygen loss from NMC materials* BASF SE, Ludwigshafen, Germany, July 18, 2008.
P. Novák	*In situ investigations of battery materials* Seminar at the State Key Laboratory of Physical Chemistry of Solid Surfaces, Xiamen University, Xiamen, China, July 9, 2008.
P. Novák	*Materials for lithium-ion batteries* Seminar at the Department of Chemistry, Zhejiang University, Hangzhou, China, July 3, 2008.
P. Novák	*In situ characterization methods - the scientific key to battery materials* 14th Int. Meeting on Lithium Batteries, Tianjin, China, June 22-28, 2008.
P. Novák	*Beyond the conventional approach: An in situ look at battery materials* Seminar at Toyota Central R&D Labs., Inc., Nagoya, Japan, June 20, 2008.
P. Novák	*Energy storage in advanced batteries* Seminar "A Physics Perspective on Climate Change and Energy Supply" of the German Physical Society, Bad Honnef, Germany, May 29, 2008.
P. Novák	*Beyond the conventional approach: An in situ look at battery materials* Seminar in the Laboratory for Inorganic Chemistry, ETH Zürich, Switzerland, February 19, 2008.
T.J. Patey	*Nanoparticles in lithium-ion batteries – opportunities and challenges* Particle Formation Symposium, Vitznau, Switzerland, July 5, 2008.
G.G. Scherer	*Radiation grafted membranes as solid electrolyte in fuel cell applications* Advances in Polymer Science and Technology, plenary lecture, New Delhi, India, January 28-31, 2008.
G.G. Scherer	*Fuel cells for transportation - an overview on European activities* Nissan Motor Company, Research Center, Kanagawa, Japan, February 6, 2008.
G.G. Scherer	*The lithium-ion battery - activities at PSI's Electrochemistry Laboratory* Dainippon Screen, Kyoto, Japan, February 7, 2008.
G.G. Scherer	*Fuel Cells I* *Fuel Cells II* International Max Planck Research School (IMPRS) "Energy", Greece, June 2–6, 2008.
G.G. Scherer	*Die Funktionsweise der Polymer Elektrolyt Brennstoffzelle* SKZ - ConSem GmbH, Kunststoffe in der Brennstoffzelle, Würzburg, Germany, June 11, 2008.

G.G. Scherer	*Radiation grafted polymer membranes for fuel cell applications achievements and challenges* IRAP2008, 8th International Symposium on Ionizing Irradiation and Polymers, keynote lecture, Angra Dos Reis, Brasil, October 12-17, 2008.
G.G. Scherer	*Radiation grafted fuel cell membranes* IPEN, Centro de Química e Meio Ambiente, Sao Paulo, Brazil, October 23, 2008.
G.G. Scherer	*Polymer electrolyte fuel cells: in situ diagnostic methods & materials development* IPEN, Centro de Células a Combustível**,** Sao Paulo, Brazil, October 24, 2008.
G.G. Scherer	*Electrochemical energy conversion and storage - R & D at Paul Scherrer Institut* IPEN, Centro de Química e Meio Ambiente, Sao Paulo, Brazil, October 25, 2008.
I.A. Schneider	*Impedance response of the proton exchange membrane in polymer electrolyte fuel cells* 5th Symposium on FC Modelling and Validation, Winterthur, March 12, 2008.
I.A. Schneider	*Recent insights obtained from local in situ diagnostics in polymer electrolyte fuel cells* 214th Meeting of The Electrochemical Society, Honolulu HI, USA, Oct 16, 2008.
B.C. Seyfang	*Micro polymer electrolyte fuel cells – simple, small, but still sophisticated enough* Catalysis Group Seminar, University of Cape Town, South Africa, February 14, 2008.

Other Talks

H. Ben youcef, P. Farquet, G.G. Scherer, C. Padeste, M. Börner[1], H.H. Solak, S. Alkan-Gürsel, V. Saile[1], A. Wokaun	*Micro-structured proton conducting membranes by synchrotron radiation induced grafting for fuel cell applications* Europolymer Conference, Gargnano, Italy, June 1-5, 2008. [1] Forschungszentrum Karlsruhe, Karlsruhe, Germany
F.N. Büchi	*Determination of liquid water distribution in porous transport layers* 214th Meeting of The Electrochemical Society, Honolulu HI, USA, October 14, 2008.
R. Flückiger	*Effective diffusivity of porous gas diffusion materials for PEFC* 5th Symposium on Fuel Cell Modelling and Experimental Validation, Winterthur, March 12, 2008.
R. Flückiger	*Anisotropic diffusivity of gas diffusion materials and current density distribution over channel and rib of PEFC* 6th International Fuel Cell Science, Engineering & Technology Conference, Denver, USA, June 16, 2008.
R. Kötz, P.W. Ruch, D. Cericola, S.H. Ng, A. Foelske	*Single wall carbon nanotubes for supercapacitors studied by in situ Raman spectroscopy and in situ dilatometry* 18th International Seminar on Double Layer Capacitors and Hybrid Energy Storage Devices, Deerfield Beach, USA, December 8-10, 2008.

F. La Mantia, F. Rosciano, N. Tran, P. Novák	*Oxygen evolution from $Li_{1+x}(Ni_{1/3}Mn_{1/3}Co_{1/3})_{1-x}O_2$ at high potentials* 213th Electrochemical Society Meeting, Phoenix, Arizona, USA, May 21, 2008.
P. Maire, A. Evans, W. Scheifele, H. Kaiser, P. Novák	*In situ colorimetric determination of lithium content in graphite anodes of lithium-ion batteries* 59th Annual Meeting of the International Society of Electrochemistry, Seville, Spain, September 11, 2008.
W. Märkle, N. Tran, P. Novák, D. Goers[1], M.E. Spahr[1], E. Grivei[1]	*Influence of the electrolyte composition and graphite particle size on the electrochemical intercalation of hexafluorophosphate anions* CARBON 2008, Nagano, Japan, July 15, 2008. [1] TIMCAL SA, Bodio
S.H. Ng, T.J. Patey, R. Büchel[1], F. Krumeich[1], J.Z. Wang[2], H.K. Liu[2], S.E. Pratsinis[1], P. Novák	*Electrochemical properties of flame spray-pyrolyzed vanadium oxide cathode nanomaterial in lithium battery* 7th International Symposium on New Nano Materials for Electrochemical Systems, Montréal, Canada, June 26, 2008. [1] ETH Zürich [2] University of Wollongong, Australia
P. Novák, M. Hahn, P. W. Ruch, D. Goers[1], M.E. Spahr[1], J. Ufheil, R. Kötz	*In situ electrochemical dilatometry: Lithium intercalation into carbon electrodes* 59th Annual Meeting of the International Society of Electrochemistry, Seville, Spain, September 11, 2008. [1] TIMCAL SA, Bodio
T.J. Patey, M. Nakayama[1], P. Novák	*Advanced characterization of $LiMn_2O_4$ nanoparticles* Seminar at Tokyo Institute of Technology, Tokyo, Japan, December 3, 2008. [1] Tokyo Institute of Technology, Tokyo, Japan
M. Reum	*High resolution measurement of current distribution and, ionic resistance in PEFCs: Insights into the channel-rib, partition of current generation* 5th Symposium on Fuel Cell Modelling and Experimental Validation, Winterthur, March 11, 2008
F. Rosciano, M. Holzapfel, N. Tran, F. La Mantia, P. Novák	*A new approach to in situ neutron diffraction applied to lithium-ion batteries* 5th Baltic Conference on Electrochemistry, Tartu, Estonia, April 30, 2008.
P. Ruch, D. Cericola, A. Foelske, R. Kötz	*In situ studies of single-walled carbon nanotubes and activated carbon in non-aqueous supercapacitor electrolytes* 59th Annual Meeting of the International Society of Electrochemistry, Seville, Spain, September 7-12, 2008.
P. Ruch, D. Cericola, A. Foelske, R. Kötz	*Electrochemical in situ studies of supercapacitor electrodes - comparing activated carbon, single-walled carbon nanotubes and graphite* Electrochemistry: Crossing Boundaries, Giessen, Germany, October 6-8, 2008.
I.A. Schneider, M.H. Bayer, A. Wokaun, G.G. Scherer	*Millisecond resolved transient response of the high frequency resistance in polymer electrolyte fuel cells* 213th Meeting of the Electrochemical Society, Phoenix, USA, May 16, 2008.

I.A. Schneider, M.H. Bayer, A. Wokaun, G.G. Scherer	*Impedance response of the proton exchange membrane in polymer electrolyte fuel cells* 41th Heyrovsky Discussion, 8th Symposium on Electrochemical Impedance Spectroscopy, Trest, Czech Republic, June 16, 2008.
G.A. Schuler	*Experimental investigation of the local membrane degradation in PEFC* Fuel Cells Science & Technology, Copenhagen, Denmark, October 10, 2008.
B.C. Seyfang, P. Boillat, G.G. Scherer, T. Lippert, A. Wokaun	*Liquid water in micro polymer electrolyte fuel cells without gas diffusion layer*59th Annual Meeting of the International Society of Electrochemistry, Seville, Spain, September 7-12, 2008.
B.C. Seyfang, P. Boillat, G.G. Scherer, T. Lippert, A. Wokaun	*Micro polymer electrolyte fuel cells: A novel design without gas diffusion layer* 5th Symposium on Fuel Cell Modelling and Experimental Validation, Winterthur, Switzerland, March 11-12, 2008.
F. Simmen, T. Lippert, P. Novák, B. Neuenschwander[1], M. Döbeli, M. Mallepell, A. Wokaun	*Influence of the substrate material on the properties of pulsed laser deposited thin $Li_xMn_2O_{4-\delta}$ films* European Materials Research Society Spring Meeting, Strasbourg, France, May 26, 2008. [1] Berner Fachhochschule, Burgdorf
F. Wallasch, L. Gubler, G.G. Scherer, A. Wokaun	*Advanced radiation grafted fuel cell membranes* 6th Swiss Snow Symposium, Fiesch, February 15-17, 2008.
F. Wallasch, L. Gubler, M. Slaski, G.G. Scherer, A. Wokaun	*Novel polymer electrolyte fuel cell membranes: preparation, characterization, and fuel cell tests* Europolymer Conference, Gargnano, Italy, June 1-5, 2008.
M. Zaglio	*Parameter extraction from experimental data using multiparameter optimization algorithms* Fundamentals and Developments of Fuel Cell Conference 2008, Nancy, France, December 11, 2008.

POSTERS

M.H. Bayer, A. Wokaun, G.G. Scherer, I.A. Schneider	*2D impedance model for low humidity PEFCs* 59th Annual Meeting of the International Society of Electrochemistry, Seville, Spain, September 7-12, 2008.
M.H. Bayer, A. Wokaun, G.G. Scherer, I.A. Schneider	*A 2-dimensional ac impedance model for polymer electrolyte fuel cells* 214th Meeting of The Electrochemical Society, Honolulu, Hawaii, USA, October 12-17, 2008.
H. Ben youcef, S. Alkan-Gürsel, L. Gubler, A. Wokaun, G.G. Scherer	*Effect of crosslinker concentration on performance and properties of radiation grafted ETFE based membranes* Advances in Polymer Science and Technology, New Delhi, India, January 28-31, 2008.
H. Ben youcef, S. Alkan-Gürsel, L. Gubler, A. Wokaun, G.G. Scherer	*Radiation grafted ETFE based membranes: Properties, fuel cell performance, and degradation analysis* Europolymer Conference, Gargnano, Italy, June 1-5, 2008.
J. Bernard, F.N. Büchi	*Fuel cell hybrid drivetrain design tool for fuel economy optimization* F-Cell Conference, Stuttgart, Germany, September 28-29, 2008.

D. Cericola, P. Ruch, R. Kötz, P. Novák, A. Wokaun	*Towards lithium ion battery and electrochemical double layer capacitor hybridization* PhD Student's Symposium 2008, Empa, St. Gallen, November 13, 2008.
S.Y. Chew, T.J. Patey, R. Büchel[1], J. Wang[2], S.E. Pratsinis[1], H.K. Liu[2], P. Novák	*$LiMn_2O_4$ thin films synthesized via an in situ annealing-assisted flame spray deposition method* 14th Int. Meeting on Lithium Batteries, Tianjin, China, June 22-28, 2008. [1] ETH Zürich [2] University of Wollongong, Australia
I. Czekaj, F. Loviat, J. Wambach, A. Wokaun	*Nickel particles behaviour at the alumina support: DFT modelling and XPS studies of model catalyst* CAMD Summer School, Electronic Structure Theory and Materials Design, Lyngby, Denmark, August 18-29, 2008.
I. Czekaj, F. Loviat, J. Wambach, A. Wokaun	*Nickel deposition on γ-Al_2O_3: Modelling of metal particles behaviour at the support* SCS Fall Meeting 2008, University Zürich, Zürich, September 11, 2008.
S.M. Dockheer, A.S. Domazou[1], L. Gubler, G.G. Scherer, W.H. Koppenol[1], A. Wokaun	*Reaction of the OH with model molecules representing a polymer membrane used in PEMFCs* Swiss Chemical Society Fall Meeting, Zürich, September 11, 2008. [1] ETH Zürich
A. Foelske-Schmitz, P. Ruch, R. Kötz	*Intercalation and film formation on HOPG in supercapacitor electrolyte – an x-ray photoelectron spectroscopy and atomic force microscopy study* 25th European Conference on Surface Science, Liverpool, England, July 27-August 1, 2008.
D. Goers[1], M.E. Spahr[1], A. Leone[1], W. Märkle, S.H. Ng, P. Novák	*Graphite negative electrode materials for power oriented lithium-ion batteries* 14th Int. Meeting on Lithium Batteries, Tianjin, China, June 22-28, 2008. [1] TIMCAL SA, Bodio
L. Gubler, G.G. Scherer	*Aging phenomena in radiation grafted fuel cell membranes* Gordon Research Conference – Fuel Cells, Bryant University, Smithfield RI, USA, July 20-25, 2008.
L. Gubler, M.M. Menamparambath, G.G. Scherer	*Comprehensive durability characterization of radiation grafted fuel cell membranes* International Workshop on Accelerated Testing in Fuel Cells, Ulm, Germany, October 6-7, 2008.
F. Loviat, I. Czekaj, J. Wambach, A. Wokaun	*Experimental and theoretical investigations of Ni-based model catalysts: Nickel deposition on γ-Al_2O_3* Catalysis for Society, XL Annual Polish Conference on Catalysis, ICSC PAS, Cracow, Poland, May 11-15, 2008.
W. Märkle, J.-F. Colin, D. Goers[1], M.E. Spahr[1], P. Novák	*Investigation of graphites at high potentials with synchrotron based in situ XRD* MRS Fall Meeting 2008, Boston, USA, December 1-5, 2008. [1] TIMCAL SA, Bodio

S.H. Ng, Ph. Bernardo, N. Tran, M.E. Spahr[1], D. Goers, C. Vix-Guterl[2], P. Novák	*Correlations between surface properties of graphite and the first cycle irreversible capacity in lithium-ion batteries* CARBON 2008, Nagano, Japan, July 13-18, 2008. [1] TIMCAL SA, Bodio [2] CNRS UPR, Mulhouse, France
S.H. Ng, F. La Mantia, W. Märkle, M. E. Spahr[1], C. Vix-Guterl[2], P. Novák	*The influence of electrode density on the electrochemical performance of highly crystalline graphites in Li-ion batteries* CARBON 2008, Nagano, Japan, July 13-18, 2008. [1] TIMCA SA, Bodio [2] CNRS UPR, Mulhouse, France
T.J. Patey, A. Hintennach, P. Novák	*How to make electrodes with nanoparticles better* 14th Int. Meeting on Lithium Batteries, Tianjin, China, June 22-28, 2008.
T.J. Patey, R. Büchel[1], S.E. Pratsinis[1], P. Novák	*Flame co-synthesis of nano-$LiMn_2O_4$ and carbon black* 14th Int. Meeting on Lithium Batteries, Tianjin, China, June 22-28, 2008. [1] ETH Zürich
A. Savouchkina, A. Foelske-Schmitz, R. Kötz, G.G. Scherer, A. Wokaun	*Degradation mechanisms of electro-catalysts used in polymer electrolyte fuel cells* PhD Student's Symposium 2008, Empa, St. Gallen, November 13, 2008.
H. Schulenburg, E. Müller[1], G. Kheslashvili[2], T. Roser, H. Bönnemann[2], A. Wokaun, G.G. Scherer	*Heat-treated $PtCo_3$ nanoparticles as catalyst for oxygen reduction* Faraday Discussion 140: Electrocatalysis – Theory and Experiment at the Interface University of Southampton, UK, July 7-9 2008. [1] FZK, Eggenstein-Leopoldshafen, Germany [2] ETH Zürich
B. Schwanitz, H. Schulenburg, A. Wokaun, G.G. Scherer	*Characterization of Pt and Pt/C (co)-sputtered electrodes for polymer electrolyte fuel cells* PhD Student's Symposium 2008, Empa, St. Gallen, November 13, 2008.
B.C. Seyfang, P. Boillat, G.G. Scherer, T. Lippert, A. Wokaun	*Micro-structuring of glassy carbon for micro polymer electrolyte fuel cells: Ns-shadowgraphy during laser ablation* E-MRS Spring Meeting 2008, Strasbourg, France, May 26-30, 2008.
F. Wallasch, L. Gubler, M. Slaski, G.G. Scherer, A. Wokaun	*Advanced fuel cell membranes: Graft copolymerization of AMS and MAN* Advances in Polymer Science and Technology, New Delhi, India, January 28-31, 2008.
F. Wallasch, L. Gubler, M. Slaski, G.G. Scherer, A. Wokaun	*Advanced fuel cell membranes: Graft copolymerization of AMS and MAN* Europolymer Conference, Gargnano, Italy, June 1-5, 2008.
F. Wallasch, L. Gubler, G.G. Scherer, A. Wokaun	*Fuel cell test results of membranes prepared via a pre-irradiation / graft polymerization / sulfonation sequence* Europolymer Conference, Gargnano, Italy, June 1-5, 2008.
F. Wallasch, L. Gubler, M. Slaski, G.G. Scherer, A. Wokaun	*Membranes for polymer electrolyte fuel cells: The pre-irradiation / graft polymerization / sulfonation sequence* 7th PSI Summer School on Condensed Matter Research, Zuoz, August 16-22, 2008.

F. Wallasch, L. Gubler, M. Slaski, G.G. Scherer, A. Wokaun	*Advanced fuel cell membranes: Graft copolymerization of AMS and MAN* 59th Annual Meeting of the International Society of Electrochemistry, Seville, Spain, September 7-12, 2008.
F. Wallasch, H. Ben youcef, M. Slaski, L. Gubler, D. Henkensmeier, A. Wokaun, G.G. Scherer	*Improved radiation grafted membranes for PEFC* Carisma Meeting, Progress MEA 2008, La Grande Motte, France, September 21-24, 2008.
F. Wallasch, L. Gubler, M. Slaski, A. Wokaun, G.G. Scherer	*Advanced polymer electrolyte fuel cell membranes prepared by graft copolymerization of AMS and MAN* IRAP2008, 8th International Symposium on Ionizing Irradiation and Polymers, Angra Dos Reis, Brasil, October 12-17, 2008.
F. Wallasch, L. Gubler, M. Slaski, A. Wokaun, G.G. Scherer	*Advanced polymer electrolyte fuel cell membranes: Fuel cell tests and post mortem analysis* IRAP2008, 8th International Symposium on Ionizing Irradiation and Polymers, Angra Dos Reis, Brasil, October 12-17, 2008.
H.C. Zellweger, A. Wokaun, G.G. Scherer, I.A. Schneider	*AC impedance based characterization of CO2 separation membranes* Europolymer Conference, Gargnano, Italy, June 1-5, 2008.

CONFERENCES, WORKSHOPS & EXHIBITIONS

P. Novák	*59th Annual Meeting of the International Society of Electrochemistry* Seville, Spain, September 14-19, 2008. Organizing Committee
P. Novák	*IMLB-14, 14th Int. Meeting on Lithium Batteries* Tianjin, China, June 22-28, 2008. Int. Scientific Committee
G.G. Scherer, R. Kötz	*Electrochemical Materials Processing* 24th One-Day-Symposium, PSI Villigen, May 7, 2008. Organizers
R. Kötz	*59th Annual Meeting of the International Society of Electrochemistry* Seville, Spain, September 7-12, 2008. Co-Organizer and Chair of Symposium 8b, Electrochemical Energy Conversion and Storage
R. Kötz	*ESSCAP 2008, 3rd European Symposium on Supercapacitors and Applications* Roma, Italy, November 6-7, 2008. Scientific Committee
G.G. Scherer	*59th Annual Meeting of the International Society of Electrochemistry* Seville, Spain, September 7–12, 2008. Co-Organizer and Chair of Symposium 8b, Electrochemical Energy Conversion and Storage
G.G. Scherer	*Advances in Polymer Science and Technology - Asian Polymer Association* New Delhi, India, January 28-31, 2008. Int. Advisory Board

G.G. Scherer	*France-Deutschland Fuel Cell Conference* Nancy, France, December 10-12, 2008 Advisory Board

MEMBERSHIPS IN EXTERNAL COMMITTEES

L. Gubler	*Prüfungskommission Physiklaboranten, Kanton Zürich* Experte
R. Kötz	*Electrochimica Acta* Advisory Board
R. Kötz	*International Society of Electrochemistry* Publications Committee
P. Novák	*International Society of Electrochemistry* Vice President
P. Novák	*The Electrochemical Society, Inc.* Member of the Technology Award Committee of the Battery Division
G.G. Scherer	*Fuel Cell Handbook* Advisory Board
G.G. Scherer	*European Fuel Cell Forum* Advisory Board
G.G. Scherer	*Kantonsschule Wohlen* Maturitätsprüfungsexperte Biologie/Chemie

Paul Scherrer Institut, 5232 Villigen PSI, Switzerland
Tel. +41 (0)56 310 21 11, Fax +41 (0)56 310 21 99
www.psi.ch